Onderzoek van turbulentie eigenschappen met de gasinjectie beeldvorming diagnostiek in de rand van de TEXTOR tokamak

Investigation of edge turbulence properties by gas puff imaging diagnostic at the TEXTOR tokamak

---

Ilya Shesterikov

Mentor KMS: Dr. Y. Xu
Promotor UGent: Prof. dr. ir. G. Van Oost
Promotor KMS: Prof. dr. ir. M. Van Schoor
Proefschrift ingediend tot het behalen van de graad van Doctor in de Ingenieurswetenschappen: Toegepaste Natuurkunde(UGent) en Doctor in de Ingenieurswetenschappen(KMS)

Vakgroep Toegepaste Fysica
Voorzitter: Prof. dr. ir. C. Leys
Faculteit Ingenieurswetenschappen en Architectuur

UNIVERSITEIT GENT

Departement Fysica
Departementshoofd: Prof. dr. ir. M. Van Schoor
Faculteit Polytechniek

Academiejaar 2013 - 2014

Members of the Examination Committee

Dr. Yuhong Xu Royal Military Academy, Belgium	Supervisor
Prof. Guido Van Oost Ghent University, Belgium	Promoter
Prof. Michael Van Schoor Royal Military Academy, Belgium	Promoter
Prof. Rik Van de Walle Ghent University, Belgium	Chairman
Prof. Christophe Leys Ghent University, Belgium	Secretary
Prof. Carlos Hidalgo EURATOM-CIEMAT, Spain	
Dr. Maarten Vergote Royal Military Academy, Belgium	
Prof. Jean-Marie Noterdaeme Ghent University, Belgium	
Dr. Jan Stöckel Institute of Plasma Physics, Czech Republic	

Acknowledgements

I owe a great intellectual debt to my supervisor, Dr. Y. Xu, a man whose expertise, understanding, and patience, added considerably to my graduate experience. I appreciate his vast knowledge and skill. I would like to thank him for his guidance, help and discussions during the work. Special thanks to him also for valuable correction of this work. I doubt that I will ever be able to convey my appreciation fully, but I owe him my eternal gratitude.

I would like to thank the head of the laboratory for plasma physics of ERM/KMS Prof. M. Van Schoor and the director of "Institut für Energie- und Klimaforschung - Plasmaphysik" of FZJ Prof. U Samm, who provided us the opportunity, direction, technical support and prepared all condition for this work.

I would like to express my gratitude to Prof. G. Van Oost for various supports and encouragements he gave to me. It was under his tutelage that I developed a focus and became involved in fusion research.

I would like to thank M. Vergote and P. Dumortier for the assistance in the development of the gas puff imaging system at TEXTOR.

A very special thanks goes out to M. Berte, R. Philips, R. Osselaer, P. Despontin, M. Vervier and V. Lancelotti who provided a timely and comprehensive technical support throughout the period of this project.

I must also thank B. Schweer, T. Lambertz, S. Brezinsek, B. Unterberg, A. Hueber from FZJ for their valuable advices on the issues of optics and mechanical engineering.

Thanks also goes out to those who provided me with valuable advices at times of critical need, comments and suggestions; H. Stoschus, O. Schmitz, S. Bozhenkov, J. Coenen, D. Borodin.

I thank Stefan Jachmich for his substantial effort in the course of biasing H-mode experiment at TEXTOR.

I want honestly thank the technical staff of FZJ: G. Esser, J. Schruff, G. Zientz, R. Dohmen, , I. Lassiwe, H. Reimer, H-G. Esser, K. Bovert von, K.Kloren. You have been of great help, assistance, recommendations and support to me with the development of the GPI system. I would very much like to express my gratitude for the time you invested in this project.

I am indebted to S. J. Zweben and R. Maqueda, who gave valuable advices for the development and implementation of the GPI system. Your pioneering works have certainly been a key to success of this project.

I would also like to thank my wife Alena without whose love and encouragement I would not have finished this project.

Juelich, August 2013
Ilya Shesterikov

Table of Contents

List of Acronyms

A

AT	Ambient Turbulence

B

BDT	Biglari-Diamond-Terry
BES	Beam Emission Spectroscopy
BN	Boron Nitride

C

CCD	Charge-Coupled Device
CR	Collisional-Radiative

D

DW	Drift Waves

F

FFT	Fast Fourier Transform
FWHM	Full Width at Half Maximum

G

GAM	Geodesic Acoustic Mode
GPI	Gas Puff Imaging

L

LCFS	Last Closed Flux Surface
LFZF	Low-Frequency Zonal Flow

N

NA	Numerical Aperture

Q

QC	Quasi-Coherent

R

RMS	Root Mean Square
RS	Reynolds Stress

S

SOL	Scrape-Off Layer

T

TDE	Time-Delay Estimation

Z

ZF	Zonal Flow

Nederlandse samenvatting –Summary in Dutch–

Hoge temperatuur plasmas worden intensief bestudeerd met het doel om een beheerst kernfusieproces tot stand te brengen voor energieproductie in de toekomst. Het meest voorkomende plasma-opsluitingsconcept is gebaseerd op toroïdale magnetische veldgeometrieën, waarin een magneto-hydrodynamisch evenwicht kan worden bereikt. Een groot onopgelost probleem van kernfusie-onderzoek zijn de deeltjes-en energietransportprocessen in het opsluitende magnetisch veld. Verschillende mechanismen zijn verantwoordelijk voor een radiaal verlies van deeltjes en energie uit het plasmavolume. In fusieplasmas wordt een belangrijke fractie van de deeltjes- en energieverliezen toegeschreven aan turbulente fluctuaties in dichtheid n_e, temperatuur T_e en potentiaal ϕ_p. Deze turbulente fluctuaties in het plasma worden aangedreven door verschillende micro-instabiliteiten en een gedetailleerd inzicht in deze instabiliteiten is vereist om het turbulente transport in toekomstige experimenten onder controle te houden.

Uit eerdere onderzoeken, uitgevoerd op tokamaks [1–5] en stellaratoren [6, 7], blijkt dat turbulente structuren sterk uitgerekt zijn langs de magnetische veldlijnen. Snelle bewegingen van zeer mobiele elektronen langs de magnetische veldlijnen egaliseren fluctuaties langs het veld wat significante wijzigingen in het radiale vlak ten opzichte van het poloïdale vlak beperkt. Hierdoor blijkt de turbulentiedynamiek loodrecht op de magnetische veldlijnen informatiever. Bijgevolg zijn voor de karakterisering en de studie van de onderliggende fysische mechanismen twee-dimensionale (2D) (radiaal *vs* poloïdaal) turbulentiemetingen vereist. Twee methoden worden algemeen gebruikt in onderzoek naar de loodrechte turbulentie structuur: Langmuir sondes [8–10] en bundel-emissiespectroscopie (BES) [11,12]. Echter heeft BES doorgaans niet voldoende ruimtelijke resolutie en kunnen Langmuir sondes niet erg diep in het hete plasma doordringen. Voor 2D-metingen, biedt de gasinjectie beeldvorming (GPI) een interessant alternatief. Met deze diagnostiek, kunnen poloïdale turbulente structuren met een hoge ruimtelijke en temporele resolutie worden gemeten. In het kader van dit doctoraatsproject is het GPI-systeem ontworpen en gemplementeerd in de TEXTOR tokamak.

Een van de belangrijkste en meest uitdagende data analysemethoden relevant voor de verwerking van GPI data is de reconstructie van het snelheidsvectorveld uit de sequentie van gemeten GPI frames. Deze reconstructie kan ons inzicht in plasmaturbulentie en haar link naar de turbulente deeltjesflux aanzienlijk verbeteren. Met informatie over het tijdsafhankelijk snelheidsvectorveld kan de wisselwerking tussen vorticiteit en dichtheidsfluctuaties onthult worden en, op deze manier, ons inzicht verdiepen in de rol van het Hasegawa-Wakatani model in de beschrijving van de tijdsevolutie van plasmaturbulentie. Recentelijk is er steeds meer belangstelling voor het afleiden snelheidsvectorvelden uit ruimte- en tijdsafhankelijke dichtheidsfluctuatiedata verkregen hetzij met BES of GPI [13–15]. Als voorbeeld wijzen we op het recente werk waar de twee-dimensionale ruimtelijke tijdscorrelaties zijn toegepast op gasinjectievisualisatiedata gemeten in de rand van EAST tokamakplasmas [15]. Van bijzonder belang is de hybride-techniek die optische stromen [16] en de lokale patroonmatchingtechnieken combineert, en die geïmplementeerd en getest is op de GPI gegevens van de Nationale Sferische Torus Experiment (NSTX) machine [14]. In dit werk is de multi-resolutie optische stromingsmethode geïmplementeerd en gebruikt voor de verwerking van GPI-gegevens.

De turbulentie-stromingsinteractie is een belangrijk aspect van de randfysica door de rol van $E_r \times B$ afschuifstromen in de onderdrukking van turbulentie en de vermindering van radiaal transport. De onderdrukking van turbulent transport in het randgebied is vermoedelijk het resultaat van de vorming van een radiaal gelokaliseerd gebied van afschuivende poloïdale rotatie, de zogenaamde "afschuivingslaag". De lokale vermindering van fluctuaties in de afschuivingslaag wordt zowel waargenomen bij de L-H overgang [17, 18] als in standaard ohmische regimes [19, 20]. Een diep inzicht in de turbulentie-stromingsinteractie vereist een gedetailleerde karakterisering van de poloïdale stromen in de plasmarand. Een van de traditionele methoden om de gemiddelde poloïdale plasmarotatie in de rand te karakteriseren is gebaseerd op de schatting van de fasesnelheid van plasmaturbulentie. De metingen van de fasesnelheid worden gedaan met behulp van de tijdsvertragings-schatting tussen turbulentiesignalen van twee polodaal gescheiden punten. Als alternatief kan de poloïdale snelheid op elke radiale positie ook worden afgeleid met de optische stromingstechniek uit de sequentie van GPI frames. De metingen van de poloïdale snelheid met de Langmuir sonde en GPI diagnostiek zijn in dit werk vergeleken met de poloïdale $E_r \times B$ stroming in de rand.

De vermindering van de turbulente transport in aanwezigheid van afschuivende stromen is toegewezen aan radiale decorrelatie mechanismen. In tegenstelling tot andere mechanismen, heeft radiale decorrelatie de universaliteit die nodig is om de onderdrukking van turbulentie door afschuivende stromen te verklaren die waargenomen is op verschillende machines en in verschillende regimes met verschillende turbulente modi. Dit model werd door Biglari, Diamond en Terry [21] (BDT model) voorgesteld en hun hypothese werd sinds dan ondersteund door vele werken [10, 20]. De meeste van deze werken zijn gebaseerd op Langmuir sondemetingen. De systematische studie van de eddy-decorrelatie door afschuivende stromen waargenomen met de tweedimensionale (2D) gasinjectievisualisatiediagnostiek (GPI) in de rand van de TEXTOR tokamak wordt gepresenteerd. Bovendien, presenteren we voor de eerste keer direct experimenteel bewijs van eddy-verbreking door afschuivende stromen in fusieplasmas. Deze afschuivende stromen zijn spontane poloïdale stromen natuurlijk gevormd in de plasmarand.

Naast spontane stromen kunnen poloïdale stromen in het plasma ook gegenereerd worden door extern veroorzaakte elektrische velden. In het concept van plasmabias is de plasmapotentiaal lokaal geïnduceerd door middel van een voorspanningselektrode uit grafiet ingebracht in het hete plasma. In dit werk wordt plasmabias toegepast om de tussenliggende mechanismen betrokken bij de turbulentie-stromingsinteractie te bestuderen.

Met uitzondering van de gemiddelde $E_r \times B$ stromen, kan het onderdrukken van turbulentie ontstaan door zonale stromen (ZFs). Dit type poloïdale stromen wordt spontaan geëxiteerd, is poloïdaal en toroïdaal symmetrisch, lang levende $E_r \times B$ structuren. In tegenstelling tot de gemiddelde "nul-frequentie"-stromen hebben deze stromen een eindige, hoewel kleine, oscillatiefrequentie. ZFs worden verondersteld te worden veroorzaakt door turbulente Reynolds spanning [22, 23], die niet-lineaire kleinschalige driftgolven in de grootschalige ZF koppelt. In toroidale plasmas verwacht men twee soorten zonale stromingen: de laagfrequente ZF en de hoogfrequente geodetische akoestische modus (GAM). Deze stromen zijn de reden van de oscillerende L-H overgangsfase (de zogenaamde dithering of I-fase), bijvoorbeeld waargenomen op de ASDEX Upgrade tokamak [24]. Sommige theorieën [25] stellen dat deze stromen de L-H overgangsvermogendrempel aanzienlijk verlagen, in vergelijking met de situatie wanneer zonale stromen ontbreken. Om deze redenen zijn deze stromen in de afgelopen vijftien jaar het onderwerp van intensief onderzoek op vele machines over de hele wereld [26–31]. De bicoherentie analyse is de experimentele onderzoeksmethode voor coherente drie golvenkoppeling, een maat voor de ZF-aandrijving. De fysica van ZF aandrijving, het effect van de ZF op turbulentie en transport, en bispectrale analysetechnieken zijn ook onderzocht in dit werk.

English summary

High-temperature plasmas are intensively studied with the aim to achieve a controlled nuclear fusion process for the future energy production. The most widespread confinement concept is based on toroidal magnetic field geometries. A major unresolved problem of nuclear fusion research is particle and energy transport processes across the magnetic field. Various mechanisms are responsible for a radial loss of particles and heat out of the plasma volume. In fusion plasmas, a major fraction of the particle and energy losses is attributed to the turbulent fluctuations in density n_e, temperature T_e and potential ϕ_p. Turbulent fluctuations in the plasma are driven by different micro-instabilities and a detailed understanding of these instabilities is required in order to control turbulent transport in future experiments.

Previous investigations, carried out on tokamaks [1–5, 32] and stellarators [6, 7], show that turbulent structures are highly elongated along magnetic field lines. Rapid streaming of the highly mobile electrons along magnetic field lines smoothes fluctuations along the field and thus restricts significant variations to the radial *vs* poloidal plane. Therefore, the dynamics of turbulence across magnetic field lines is more informative. Consequently, characterization and understanding the underlying physical mechanisms require essentially two-dimensional (2D) (radial *vs* poloidal) turbulence measurements. Two methods are commonly used for the investigation of the perpendicular structures of the turbulence: Langmuir probe arrays [8–10] and beam emission spectroscopy (BES) [11, 12]. However, BES typically does not have enough spatial resolution and Langmuir probes can not penetrate very deep into the hot plasma. For 2D measurements, the gas puff imaging diagnostic (GPI) presents an interesting alternative. With this diagnostic, the poloidally resolved turbulent structures can be measured with high spatial and temporal resolutions. This PhD project has primarily three purposes: (I) development of the GPI system at the TEXTOR tokamak, (II) development of data processing methods relevant to the GPI measurements and (III) investigation of the two-dimensional turbulence dynamics using the GPI. The latter study focuses primarily on the interaction of turbulence and flows in toroidal plasmas.

Within the frame of this PhD project, ~~the~~ a GPI system has been designed and implemented at the TEXTOR tokamak. With this diagnostic, the two-dimensional structure and dynamics of turbulence in the edge of TEXTOR have been observed for the first time. The main technical novelty of this system is the novel design of the in-vessel GPI optical telescope, which is implemented to protect in-vessel optical components from coating and severe thermal loads. The presented design

~~might~~ could be used as a basis for ~~the~~ GPI systems on next generation machines. The assessment of diagnostic issues and limitations suggests that the local gas puff with the flux $(6-8) \times 10^{19}$ molecules/s, typical for the GPI experiment on TEXTOR, does not influence substantially on local and global plasma performance neither on plasma turbulence properties. Meanwhile, we have shown that the equilibrium/fluctuating emission intensity is more sensitive to the equilibrium/fluctuating electron density than the equilibrium/fluctuating electron temperature, supporting the idea that ~~the~~ a GPI is the diagnostic that measures primarily density events. We identified that the dynamics of turbulence in the scrape-off layer (SOL) of limiter tokamaks is substantially different from that dynamics in divertor machines. The decay of structures in the SOL of limiter tokamaks is much faster probably due to shorter connection length of the magnetic field line to the toroidal (or even poloidal) limiter.

One of the most important and challenging data analysis methods relevant to the processing of GPI data is the reconstruction of the velocity vector field from the sequence of measured GPI frames. This reconstruction can substantially improve our understanding of plasma turbulence and its link to the turbulent particle flux. Having information about the time-resolved velocity vector field can disclose an interplay between vorticity and density fluctuations and, in this way, deepen our insight into the turbulent processes in plasma. In recent times, there has been rising interest in deriving velocity vector fields from spatially and temporally resolved density fluctuation data obtained either with BES or GPI diagnostics [13–15]. One just has to emphasize the recent work where the two-dimensional spatial time-correlations have been applied to the gas puff imaging data collected at the edge of EAST tokamak plasmas [15]. Of particular relevance is the hybrid technique, combining optical flow [16] and local pattern matching techniques, which has been implemented and tested on GPI data from the National Spherical Torus Experiment (NSTX) machine [14].

In this work, the multiresolution optical flow scheme has been implemented and used for the reconstruction of the velocity vector field from GPI data. There is a problem of local minima of the energy functional of optical flow caused by the fact that turbulent structures do not simply move but also change ~~the~~ shape, i.e., they are simultaneously ~~bended~~ bent, stretched and flattened. The smoothing of images removes these small details, remaining only a translational motion. In the multi-resolution technique the output from the coarse image is used as an initialization at a finer scale. The full pyramid of images is used, starting with the coarsest grid. It has been shown in Ref. [13] that this technique gives some improvements in the reconstruction of the velocity vector field as compared to the traditional Horn and Schunck approach.

The turbulence-flow interaction is an important aspect of the edge physics due to the role of $E_r \times B$ flow shear in the suppression of turbulence and reduction of radial transport. The suppression of turbulent transport in the edge region is believed to result from the formation of a radially localized region of a sheared poloidal rotation, so called "*shear layer*". The local reduction of fluctuations in the shear layer is observed at the L-H transition [17, 18] as well as in standard ohmic regimes [19, 20]. The following mechanisms contribute to the reduction of turbulent transport in the shear layer:

- Decorrelation of turbulent structures in the mean shear flow [21].
- The Reynolds stress driven zonal flow structures extract energy from ambient turbulence, leading to a reduction of the turbulence level [25, 29].
- These zonal flows in turn also decorrelate turbulent eddies, leading to an additional suppression of turbulence and transport [29, 33].

The deep understanding of the turbulence-flow interaction requires a detailed characterisation of the poloidal flows in the plasma edge. One of the traditional approaches applied to characterisation of the mean poloidal plasma rotation in the edge is based on the estimation of the phase velocity of plasma turbulence. Alternatively, the poloidal velocity at each radial position can also be derived from the sequence of GPI frames using the optical flow technique.

In this work, the measurements of the phase velocity have been done using the time-delay estimation between turbulence signals from two poloidally separated points. The measurements of the poloidal velocity using the GPI diagnostics are compared to the edge $E_r \times B$ poloidal flow. We have shown that in the poloidal direction turbulent structures move downward in the SOL (along the ion diamagnetic drift direction) and upward in the plasma edge (along the electron diamagnetic drift direction), following up mainly with the $E_r \times B$ drift. Both, probe and GPI measurements give the edge turbulence phase velocities of $-(1-3)\ km/s$. The corresponding phase velocity in the SOL is $1-2\ km/s$. The magnitude of the poloidal plasma rotation in both the edge and the SOL gradually reduces with increasing line-averaged density. The thickness of the shear layer, where the poloidal flow sharply changes the sign, is estimated to be $\sim 1\ cm$.

We have mentioned that the reduction of the turbulent transport in the presence of sheared flows is attributed to a number of processes, and one of them is the radial decorrelation mechanisms. In contrast to other mechanisms, the radial decorrelation have that universality which is needed to explain the suppression of turbulence by sheared flows observed on different machines in different regimes with various turbulent modes. This model was proposed by Biglari, Diamond and Terry [21] (BDT model) and since that time their hypothesis has been supported by many works; see [10, 20] and references therein. However, most of these works are based on Langmuir probe measurements. Our work presents the systematic study of the eddy decorrelation with the use of the two-dimensional (2D) gas-puff imaging (GPI) diagnostic. In particular, for the first time we present the direct experimental evidence of eddy breaking by sheared flows in fusion plasmas. These sheared flows are spontaneous poloidal flows naturally formed in the plasma edge. The shearing effect on eddies depends on ~~the coherence length of the eddy structure, namely,~~ the poloidal $l_{c\theta}$ and radial l_{cr} correlation lengths $\omega_s \propto l_{cr} l_{c\theta}^{-1}$. The magnitude of the flow shearing rate plays a key role for the eddy breaking and needs to be larger than some lower limit.

Except of mean $E_r \times B$ flows, the suppression of turbulence can occur by zonal flows (ZFs). These poloidal flows are spontaneously excited, poloidally and toroidally symmetric and long lived $E_r \times B$ structures. In contrast to the mean "zero-frequency" flows, these flows have finite, though small, oscillation frequency. ZFs are supposed to be driven by the turbulent Reynolds stress [22,23], which non-linearly couples small-scale drift-waves with large-scale zonal flows. In toroidal plasmas, two types of zonal flows are expected: the low-frequency ZF and the high-frequency geodesic acoustic mode (GAM). These flows are the reasons for the oscillatory L-H transition phase (so called "dithering" or "I-phase"), observed, for instance, on ASDEX Upgrade [24], EAST [34] and W7-AS [35] machines. Some theories [25] state that these flows substantially lower the L-H transition power threshold as compared to the situation when zonal flows are absent. For these reasons, in the past fifteen years, these flows have been the subject of intensive studies on many machines around the globe [26–31].

Besides spontaneous flows and zonal flows, poloidal flows in the plasma can also be generated by externally induced electric fields. In the concept of plasma biasing, the plasma potential is locally induced by means of an graphite biasing electrode inserted into the hot plasmas.

In this work, biasing is applied in order to study the intermediate mechanism involved in the turbulence-flow interaction. These results present the first evidence of the eddy stretching and splitting process in a confinement device and the intimate interaction between sheared flows, eddy structures, Reynolds stress, zonal flows and ambient fluctuations during the transition to an improved confinement. The flow shear gives the dynamical influence on turbulence structures, which results in the generation of the Reynolds stress and zonal flows and eventually suppresses background fluctuations due to the nonlinear energy transfer.

In the last chapter, a comprehensive analysis of GAM zonal flows is presented. We identified that the apparent ≈10 kHz mode in the frequency spectrum of floating potential is related to GAM zonal flows. For instance, a systematic study shows that the measured frequencies of this mode very well correspond to the theoretical dispersion relation of GAM zonal flow. Experiments show high toroidal and poloidal homogeneity of this mode, in agreement with the theoretical model. These results are consistent with the finding that there is no direct contribution of GAM zonal flows, in themselves, to the turbulent transport. The bicoherence analysis is the experimental investigation method of coherent three-wave coupling, a measure of the ZF drive. The nonlinear interaction between GAM and ambient turbulence has been identified using the auto-bicoherence of $\tilde{\phi}_{fl}$ and cross-bicoherence of $\tilde{v}_r$ and $\tilde{v}_\theta$. ~~Meanwhile, the cross-bicoherence analysis which directly involves Reynolds stress components of~~ $\cancel{\tilde{v}_r}$ ~~and~~ $\cancel{\tilde{v}_\theta}$ ~~shows better coupling than the traditional auto-bicoherence of~~ $\cancel{\tilde{\phi}_{fl}}$~~, which again supports the theory of a Reynolds stress driven zonal flows.~~

In conclusion, dedicated experiments have been conducted at TEXTOR in standard ohmic and biasing-induced plasmas to study the underlying physics of turbulence-flow interaction. These results present the first evidence of eddy stretching and splitting processes in a high temperature fusion plasmas. In improved con-

finement regimes induced by limiter biasing, the results show the systematic tilting and uniform alignment of turbulent eddies when small flow shear is imposed. Such stretching of turbulent eddies results in the Reynolds stress generation. In its turn, the Reynolds stress production imposes the development of low frequency zonal flows structures, what suggests that the model of zonal flows driven by the Reynolds stress is correct. Finally, the physics of the GAM zonal flow, the effect of GAM on turbulence and transport and the bispectral analysis techniques are also investigated in this work.

1
Introduction

The rising energy consumption around the globe could eventually lead to an energy crisis if no alternatives to the conventional energy sources will be provided. The continuously running down hydrocarbon reserves (such as oil, coal and gas), which nowadays are the primary energy sources, will be completely depleted already by the middle of the 21th century. However, taking into account the global warming (greenhouse effect), caused by carbon dioxide emissions as a result of fossil fuel combustion, the ecological consequences could arise even earlier.

Controlled nuclear fusion provides a promising alternative as it proposes an almost inexhaustible, relatively safe and clean energy source. It is known from the nuclear physics that the nuclear fusion is a nuclear reaction in which two or more atomic nuclei collide at a very high speed and join to form a new type of *bound* atomic nucleus. The mass difference between the initial components and the reaction products is associated with the binding energy, according to Einstein's relation. The fusion process of two light nuclei has been found to release this binding energy, providing a potential energy source. The reaction between two light nuclei which has the highest cross-section is the reaction between deuterium (D) and tritium (T). One kilogramm of a deuterium-tritium mixture will be sufficient to provide 100 MW of fusion energy for 24 hours.

The D-T fusion reaction components are abundant on the Earth. Deuterium presents in seewater in virtually boundless quantities. Tritium can be produced when fusion neutrons interact with litium that is also present in the water of mineral springs and brine pools. Therefore, fusion energy could cover the world energy demand for thousands of years.

The resulting high neutron flux can cause induced radioactivity so that components in fusion reactor may become highly radioactive increasing the amount of nuclear waste. However, this issue is much less harmful than the associated problem of fission reactors.

Another important argument in favour of fusion energy is an inherent safety of fusion reactor concept. The burning process in fusion reactor is not of an avalanche nature. Instead, the plasma confinement always balances on the brink of disruption and any technical failure terminates this very fragile process. Moreover, the amount of fuel stored in fusion reactor is very limited because reaction components are continuously supplied to the combustion zone. Therefore, the threat of meltdown or other large-scale catastrophe is naturally absent.

Despite of more than 60 years of the active international research on controlled nuclear fusion, commercial power production is still believed to be unlikely before 2050. Conditions that are necessary to ignite of a self-sustaining burning plasma have not been achieved in plasma confinement devices. To date, the most promising approach towards this goal is a magnetic confinement in a so-called "tokamak". In spite of a world record fusion power production of 16 MW, achieved in 1997 on JET tokamak, the self-sustaining regime is still an open issues. In that context one should mention the following problems:

- the unpredictable high level of particle and energy transport, that limits the ability to attain fusion ignition in the laboratory
- degradation of first wall materials due to extremely high energy/particle and radiation fluxes on a material surface (for instance melting, sputtering and nuclear transmutation) limits the lifetime of reactor components
- the suppression/control of a magnetohydrodynamic (MHD) instabilities that lead to a high transient heat load on reactor components and plasma disruptions (termination of a magnetically confined plasma)

1.1 Turbulence and turbulent transport in tokamaks

Experimental measurements of the cross-field transport in tokamaks show that the heat conductivity for ions is one order of magnitude larger than the neoclassical one, while that quantity for electrons is two orders of magnitude larger than values predicted by neoclassical theory. The particle transport is also larger than the neoclassical. The deviation from the neoclassical transport is called "anomalous transport". There are several possible explanations of the anomalous transport and the most widely followed explanation is the role of the plasma turbulence. Instabilities in the plasma give rise to local fluctuations in plasma potential and plasma density, which eventually causes particle and energy transport across the magnetic field.

The understanding of turbulent behavior in plasma and neutral fluids is one of the most intriguing, frustrating and important problems in the classical physics. Despite of an active study of the problem of turbulence for years, yet we do not understand in complete detail how or why turbulence occurs, nor can we reliably control or suppress turbulent behavior (from an engineering perspective). Thus, study of turbulence is motivated both by its inherent intellectual challenge and by the practical application of these knowledges.

Turbulence in the edge region of tokamaks and other magnetized plasmas has been measured for many years. This topic is important to the progress of magnetic confinement fusion since edge plasma conditions will play a significant role in both the plasma-wall interaction and the global plasma performance. The transport at the edge and the SOL depends on the level and characteristics of this turbulence and, consequently, on the edge temperature and density. The edge conditions then may affect the core confinement through their effects on edge gradients and gradient driven instabilities such as drift waves (DW). The edge turbulence may also play a crucial role in high confinement physics (i.e., H-mode physics) where steep edge pedestals in the temperature and density form within the closed field line region nearby the separatrix.

In the SOL, turbulent transport exhibits intermittent convective behavior (blobby behavior) [36, 37]. These blobs are coherent structures extending in a filamentary way along magnetic field lines and leaving the plasma radially at a rather high speed. Such blobs can result in a high level erosion of the first wall. As such, the characterization of the blobby transport and understanding the physical mechanisms of the blob generation and evolution processes are extremely demanded in fusion research.

The turbulence in magnetized plasmas is essentially two-dimensional. Rapid streaming of the highly mobile electrons along magnetic field lines smoothes fluctuations along the field and thus restricts significant spatial variations to the radial vs poloidal plane. It essentially modifies the turbulent cascade. In conventional three-dimensional turbulence only the direct energy cascade is expected because the energy is the only conserved quantity in the turbulent system. When the dynamics of the turbulence is limited by two dimensions only, both energy and enstrophy are conserved. As a consequence of this constraint, the dual cascade is formed with inverse energy and direct enstrophy transfer. Simply put, a magnetic field substantially modifies the dynamics of turbulence. However, on the other hand, it implies that the turbulence diagnostic methods could be simplified from three-dimensional measurements to two-dimensional ones, assuming that the dynamics perpendicular to the magnetic field lines is more informative.

1.1.1 Zonal flows

One of the intriguing phenomena in the physics of plasma turbulence is the formation of large scale flows (zonal flows) from small scale drift wave turbulence. In the context of tokamak plasmas, this type of poloidal flows is spontaneously excited, poloidally and toroidally symmetric $E_r \times B$ structures. In contrast to the mean "zero-frequency" flows, these flows have finite, though small, oscillation frequency.

Two important features of a drift wave - zonal flow system drive the strong interest in the study of zonal flows:

- First, the zonal flow shearing acts to regulate and reduce turbulence and transport. The associated zonal $E_r \times B$ poloidal flow changes its sign with radius. Correspondingly, the shearing in the zonal $E \times B$ flow tilts turbulent eddies, narrowing their radial extent. It implies that the radial wavenumber of turbulence increases. As a consequence of this, an increase in the radial wavenumber reduces the effective step size for turbulent transport.

- Second, since zonal flows are generated by nonlinear energy transfer from drift waves to zonal flows, their generation naturally acts to reduce the level of ambient turbulence.

These beneficial features drive the continuous increase of interest in zonal flow studies for last fifteen years. Some technique, applied to stimulate an energy transfer from broadband turbulence to zonal flows, would be an attractive way to reduce and control the turbulent transport in fusion plasmas. Therefore, the search for effective methods of generation of zonal flows is currently an active research area [38].

The process of nonlinear energy transfer from turbulence to zonal flows is the nonlinear coupling between two structures of disparate scales since drift waves have high frequency and wavenumber ($\omega_{DW} \sim 30 - 150\ kHz$, $k_\perp^{DW}\rho_i \sim 1$) in comparison to zonal flows ($k_\perp^{ZF}\rho_i \ll 1$, $\omega_{ZF} \sim 0$). In that sense, the zonal flow formation phenomena is related to an aforementioned inverse cascade of energy in a two-dimensional turbulence, which leads to a formation of large-scale structures. However, the conventional inverse energy cascade proceeds via a local coupling in wavenumber space while zonal flow generation occurs via non-local (because zonal flows are large-scale structures) transfer of energy between small and large scales. In that context, the process of zonal flow generation is similar to the dual cascade phenomenon familiar from the two-dimensional hydrodynamics. Here, the growth of zonal flow corresponds to the inverse energy cascade, whereas the increase in the radial wavenumber is similar to the forward enstrophy cascade.

In toroidal plasmas, two types of zonal flows are expected: the low-frequency ZF (LFZF) and the high-frequency geodesic acoustic mode (GAM). The inhomogeneity of the toroidal magnetic field causes a difference in mean poloidal $E_r \times B$ rotations between the inner and outer sides of the torus. This induces poloidal pressure asymmetry, for instance a compression at the top ($\delta p > 0$) and a decompression at the bottom ($\delta p < 0$), as shown in Fig. 1.1(a). In the case of the low-frequency ZF, this asymmetry is compensated by a return flow along field lines because the magnetic field lines following the helical path connect top with the bottomm of the torus.

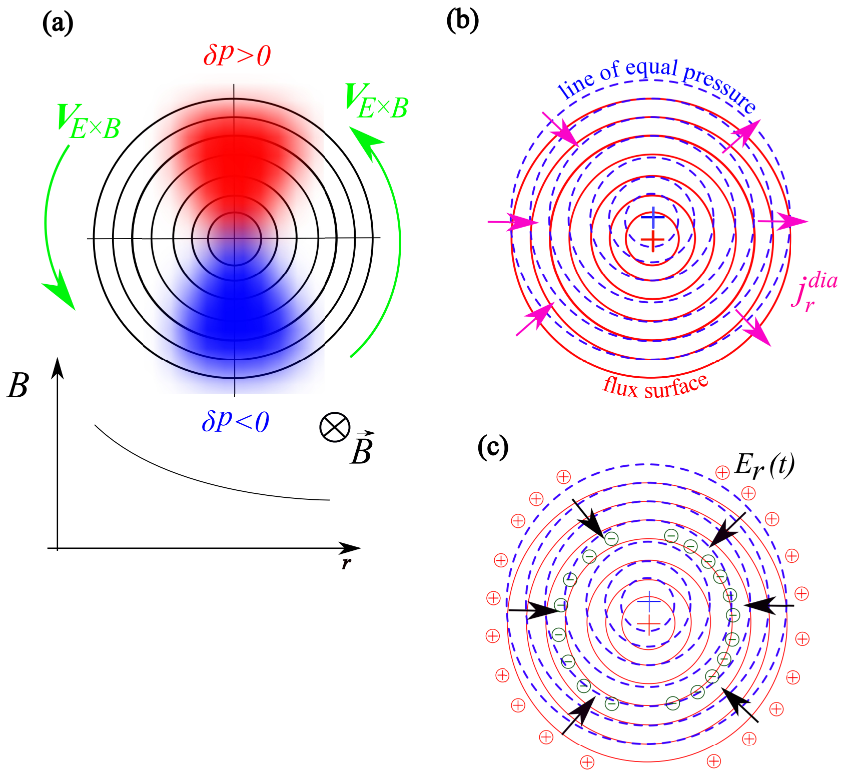

Figure 1.1: (a): A difference in mean poloidal $E_r \times B$ rotations causes a compression of the plasma at the top and a decompression at the bottom. (a)-(b): The formation of GAM zonal flows in toroidal plasmas. (b): The pressure up-down asymmetry leads to the displacement of the pressure contours (blue dashed lines) with respect to the magnetic surfaces (red solid lines), which in turn causes the radial component of the diamagnetic current j_r^{dia} (magenta arrows). (c): This diamagnetic current results in the charge separation, radial electric field $E_r(t)$ (black arrows) and an associated polarisation current.

Alternatively, this assymetry can induce the oscillatory behavior of the flows [29, 33, 39], thereby forming GAM zonal flow oscillations. The formation of GAM zonal flows in toroidal plasmas is explained in Fig. 1.1. The pressure up-down asymmetry leads to a vertical displacement of the pressure contours (contour connecting points of equal plasma pressure) with respect to the flux surfaces. For instance, the up-down asymmetry shown in Fig. 1.1(a) leads to an upward vertical displacement as in Fig. 1.1(b). The main restoring force appears from the radial component of the diamagnetic current j_r^{dia} (magenta arrows in Fig. 1.1(b)) and the corresponding time varying radial electric field $E_r(t)$ (black arrows in Fig. 1.1(c)), which arise from this displacement. The polarisation current associated with this radial electric field leads to the time varying poloidal plasma flows oscillating at the GAM frequency.

1.2 Outline of this work

Before going ahead, in the next chapter the TEXTOR tokamak and its typical discharge parameters for experiments of this work are described for reference.

Traditionally, the information about the 2D structure of plasma edge turbulence in tokamaks and stellarators has been obtaining for years using the statistical two-point cross-correlation technique. The GPI diagnostic provides the 2D imaging of edge turbulence in which both the radial and poloidal structures are measured at one instant of time rather than inferred from statistical correlations. The GPI systems installed at different machines around the globe provide the information about 2D nature of plasma turbulence with the highest spatial resolution. In the GPI diagnostic the instantaneous two-dimensional radial vs poloidal structure of the turbulence is observed along the local magnetic field line direction using fast frame cameras. By using a controlled neutral gas puff, the brightness and contrast of the turbulent emission fluctuations are increased and the structure can be measured independently of a natural gas recycling. The implementation of the GPI diagnostic in the TEXTOR tokamak is presented in chapter 3 together with typical results from this experiment.

The experimental reconstruction of the velocity vector field is one of the common data processing tools applied to GPI data. This approach can substantially improve our understanding of plasma turbulence and its link to the turbulent particle flux. Chapter 4 provides a detailed explanation of this technique. Meanwhile, it considers the reconstruction of the velocity vector field using data from GPI diagnostic at TEXTOR.

The turbulence-flow interaction is an important aspect of the edge physics. The dynamics of and an interplay between mean shear flows, zonal flows and turbulence modes are key mechanisms behind the turbulence-flow interaction. The study on this issue requires the detailed characterisation of the poloidal flows in the plasma edge. In chapter 5, poloidal flows in the plasma edge are investigated.

At present, there exists robust experimental evidence on the importance of the mean radial electric field (E_r) and associated $E_r \times B$ shear flows in reducing turbulent transport [17, 19, 20, 40]. This phenomenon is ascribed to the radial decorrelation mechanisms. However, this process has never been directly visualized in high-temperature plasma. In chapter 6, we present the systematic study of the eddy decorrelation by sheared flows observed by a two-dimensional (2D) gas-puff imaging (GPI) diagnostic in the TEXTOR tokamak.

Except of mean $E_r \times B$ flows, the suppression of turbulence can occur by zonal flows. Zonal flows are self-generated from turbulent velocity fluctuations. In chapter 7, we present the detailed experimental observation on the mechanisms behind the generation of zonal flows and then the role which zonal flows play in the transition to an improved confinement. The dynamics of and an interplay between mean shear flows, zonal flows and turbulence modes are key mechanisms which are addressed.

In the past ten years, GAM zonal flows have been the subject of intensive studies on many machines around the globe [26–31]. At TEXTOR, GAM zonal flows have been initially identified by correlation reflectometry [41] as a density fluctuations at the top of the vacuum vessel. Further characterisation of GAM zonal flows at TEXTOR and their radial propagation has been reported in Refs. 42, 43. A comprehensive experimental analysis of GAM zonal flows and the role they play in the turbulent transport is given in chapter 8.

1.3 Publications

The following papers and conference contributions have been published or presented within the frame of this PhD project.

Refereed journal publications

1. **I. Shesterikov**, Y. Xu, C. Hidalgo, M. Berte, P. Dumortier, M. Van Schoor, M. Vergote, G. Van Oost and the TEXTOR Team. Direct evidence of eddy breaking and tilting by edge sheared flows observed in the TEXTOR tokamak. *Nucl. Fusion*, 52:042004, 2012.

2. **I. Shesterikov**, Y. Xu, M. Berte, P. Dumortier, M. Van Schoor, M. Vergote, B. Schweer and G. Van Oost. Development of the gas-puff imaging diagnostic in the TEXTOR tokamak. *Review of Scientific Instruments*, 84:053501, 2013.

3. **I. Shesterikov**, Y. Xu, G. R. Tynan, P. H. Diamond, S. Jachmich, P. Dumortier, M. Vergote, M. Van Schoor, G. Van Oost and the TEXTOR team. Experimental evidence for the intimate interaction among sheared flows,

eddy structures, Reynolds stress and zonal flows across a transition to improved confinement. *Physical Review Letters*, 111:055006, 2013.

4. Y. Xu, **I. Shesterikov**, M. Van Schoor, M. Vergote, R. R. Weynants, A. Krmer-Flecken, S. Zoletnik, S. Soldatov, D. Reiser, K. Hallatschek, C. Hidalgo and the TEXTOR Team. Observation of geodesic acoustic modes (GAMs) and their radial propagation at the edge of TEXTOR tokamak. *Plasma Physics and Controlled Fusion*, 53:095015, 2011.

5. Y. Xu, C. Hidalgo, **I. Shesterikov**, M. Berte, P. Dumortier, M. Van Schoor, M. Vergote, A. Krämer-Flecken, R. Koslowski and the TEXTOR Team. Role of symmetry-breaking induced by $E_r \times B$ shear flows on developing residual stresses and intrinsic rotations in the TEXTOR tokamak. *Nuclear Fusion*, 53:072001, 2013.

6. Y. Xu, C. Hidalgo, **I. Shesterikov**, A. Krämer-Flecken, S. Zoletnik, M. Van Schoor, M. Vergote and the TEXTOR Team. Isotope effect and multi-scale physics in fusion plasmas. *Physical Review Letters*, 110:265005, 2013.

7. Y. Xu, D. Carralero, C. Hidalgo, S. Jachmich, P. Manz, E. Martines, B van Milligen,M. Pedrosa, M. Ramisch, **I. Shesterikov**, C. Silva, M. Spolaore, U. Stroth, N. Vianello. Long-Range Correlations and Edge Transport Bifurcation in Fusion Plasmas. *Nuclear Fusion*, 51:063020, 2011.

8. S. Zoletnik, L. Bardoczi, A. Kramer-Flecken, Y. Xu, **I. Shesterikov**, S. Soldatov, G. Anda, D. Dunai, G. Petravich and the TEXTOR Team. Methods for the detection of Zonal Flows using one-point and two-point turbulence measurements. *Plasma Physics and Controlled Fusion*, 54:065007, 2012.

Conference and workshop contributions

1. **I. Shesterikov**, Y. Xu, M. Vergote, M. Van Schoor, G. Van Oost and the TEXTOR team. Investigation of GAM zonal flows in the TEXTOR tokamak. *37th European Physical Society Conference on Plasma Physics (EPS 2010), June 21–25, 2010. Dublin, Ireland*, Poster Contribution, P1.1090

2. **I. Shesterikov**, Y. Xu, M. Vergote, M. Van Schoor, G. Van Oost and the TEXTOR team. Investigation of GAM zonal flows in the TEXTOR tokamak. *Workshop on Electric Fields, Turbulence and Self-Organisation in Magnetized Plasmas (EFTSOMP 2010), June 28–29, 2010. Dublin, Ireland*, Oral Contribution.

3. **I. Shesterikov**, Y. Xu, C. Hidalgo, S. Jachmich, P. Dumortier, M. Berte, M. Vergote, M. Van Schoor, G. Van Oost and the TEXTOR team. The experimental investigation on the role of $E_r \times B$ flow shear in tilting and breaking of turbulent eddies. *39th European Physical Society Conference on Plasma Physics and 16th International Congress on Plasma Physics, July 2–6, 2012. Stockholm, Sweden*, Poster Contribution, P5.064

4. **I. Shesterikov**, Y. Xu, C. Hidalgo, S. Jachmich, P. Dumortier, M. Berte, M. Vergote, M. Van Schoor, G. Van Oost and the TEXTOR team. The experimental investigation on the role of $E_r \times B$ flow shear in tilting and breaking of turbulent eddies. *Workshop on Electric Fields, Turbulence and Self-Organisation in Magnetized Plasmas (EFTSOMP 2012), July 9–10, 2012. Stockholm, Sweden*, Oral Contribution, **Invited talk**.

5. **I. Shesterikov**, Y. Xu, C. Hidalgo, S. Jachmich, P. Dumortier, M. Berte, M. Vergote, M. Van Schoor, G. Van Oost and the TEXTOR team. The experimental investigation on the role of $E_r \times B$ flow shear in tilting and breaking of turbulent eddies. *15th European Fusion Theory Conference, September 23-26, 2013. Merton College, Oxford, UK*, Oral Contribution, **Invited talk**.

6. Y. Xu, **I. Shesterikov**, M. Van Schoor, M. Vergote, D. Reiser, A. Krmer-Flecken and the TEXTOR team. Influence of Resonant Magnetic Perturbation (RMP) and plasma density on the long-range correlation and GAM zonal flows at TEXTOR. *3rd EFDA Transport Topical Group Meeting; 15th EU-US Transport Task Force Workshop*, September 7–10, 2010. Cordoba, Spain, Oral Contribution, O4.07

7. Y. Xu, **I. Shesterikov**, M. Van Schoor, M. Vergote, R. R. Weynants, A. Krämer-Flecken, D. Reiser, S. Zoletnik and the TEXTOR team. Overview of recent results on long-range correlations and zonal flows in the edge of TEXTOR tokamak. *38th European Physical Society Conference on Plasma Physics (EPS 2011), June 27– July 01, 2011. Strasbourg, France*, Oral Contribution, O4.125

8. Y. Xu, **I. Shesterikov**, M. Van Schoor, M. Vergote, R. R. Weynants, A. Krämer-Flecken, D. Reiser, S. Zoletnik and the TEXTOR team. Overview of recent results on long-range correlations and zonal flows in the edge of TEXTOR tokamak. *6th Festival de Thèorie, July 4–22, 2011. Aix-en-Provence, France*, Oral Contribution.

9. Y. Xu, **I. Shesterikov**, M. Van Schoor, M. Vergote, R. R. Weynants, A. Krämer-Flecken, D. Reiser, S. Zoletnik and the TEXTOR team. Overview of recent results on long-range correlations and zonal flows in the edge

of TEXTOR tokamak. *Workshop on Electric Fields, Turbulence and Self-Organisation in Magnetized Plasmas (EFTSOMP 2011), July 4–5, 2011. Strasbourg, France*, Oral Contribution.

10. Y. Xu, **I. Shesterikov**, M. Berte, P. Dumortier, M. Van Schoor, M. Vergote, A. Krämer-Flecken, R. Koslowski and the TEXTOR team. Experimental measurements of residual stress and related parametric dependence for intrinsic toroidal rotation generation at the edge of TEXTOR tokamak. *4th EFDA Transport Topical Group Meeting; 17th Joint EU-US Transport Task Force Workshop*, September 3–6, 2012. Padova, Italy, Oral Contribution, O2.7

11. Y. Xu, S. Jachmich, **I. Shesterikov**, N. Vianello, M. Spolaore, E. Martines, P. Manz, M. Ramisch, U. Stroth, C. Silva, M. A. Pedrosa, C. Hidalgo, D. Carralero, B. van Milligen. Interplay between mean sheared flows and zonal flows. *18th European Fusion Physics Workshop, December 6–8, 2010. Mayrhofen, Austria*, Oral Contribution.

12. Y. Xu, C. Hidalgo, **I. Shesterikov**, M. A. Pedrosa, A. Krämer-Flecken, B. Liu, S. Zoletnik, M. Van Schoor, M. Vergote and the TEXTOR team. Isotope effect and multi-scale physics in fusion plasmas. *40th European Physical Society Conference on Plasma Physics, July 1–5, 2013. Espoo, Finland*, Oral Contribution, O2.113

13. S. Zoletnik, L. Bardoczi, G. Anda, D. Dunai, G. Petravich, D. Refy, A. Kramer-Flecken, **I. Shesterikov**, S. Soldatov, Y. Xu and the TEXTOR Team. The spatiotemporal structure of Geodesic Acoustic Modes in the edge plasma of TEXTOR. *Kinetic-Scale Turbulence in Laboratory and Space Plasmas: Empirical Constraints, Fundamental Concepts and Unsolved Problems, July 19–23, 2010. Cambridge, UK*, Oral Contribution.

14. S. Zoletnik, L. Bardoczi, G. Anda, D. Dunai, G. Petravich, D. Refy, A. Kramer-Flecken, **I. Shesterikov**, S. Soldatov, Y. Xu and the TEXTOR Team. The spatiotemporal structure of Geodesic Acoustic Modes in the edge plasma of TEXTOR. *3rd EFDA Transport Topical Group Meeting; 15th EU-US Transport Task Force Workshop*, September 7–10, 2010. Cordoba, Spain, Oral Contribution, O2.05

15. Y. Xu, N. Vianello, M. Spolaore, E. Martines, P. Manz, U. Stroth, C. Silva, M. A. Pedrosa, C. Hidalgo, D. Carralero, S. Jachmich, B. van Milligen, M. Ramisch, **I. Shesterikov**. Long-Range Correlations and Edge Transport Bifurcation in Fusion Plasmas. *23rd IAEA Fusion Energy Conference, October 11–16, 2010. Daejeon, Rep. of Korea*, Oral Contribution, EX-C/9-3

16. L. Bardoczi, S. Zoletnik, Y. Xu, **I. Shesterikov**, A. Kramer-Flecken, S. Soldatov, G. Petravich, D. Refy. Spatiotemporal structure of Geodesic Acoustic Modes in the edge plasma of TEXTOR. *38th European Physical Society Conference on Plasma Physics (EPS 2011), June 27– July 01, 2011. Strasbourg, France*, Poster Contribution, P1.065

1.4 Awards

Some results of this PhD project about the investigation of the two-dimensional dynamics of plasma turbulence have been awarded the **Itoh Project Prize in Plasma Turbulence 2012** at the 39th European Physical Society Conference on Plasma Physics in Stockholm (see appendix A).

2

Tokamak

The fusion plasmas cannot be confined directly in material vessels since no solid material could withstand the extremely high temperature of the fusion plasma. The problem is obviated by using magnetic fields, which confine and thermally insulate the plasma, keeping it away from the vessel walls. When a charged particle, ion or electron, moves in a static magnetic field, it traces a helical path, the axis of which is parallel to the magnetic field. The particles are thus tied to the field lines and move freely along magnetic field lines. Therefore, it is possible to confine a plasma and keep it away from material walls. The tokamak has emerged as the most promising magnetic confinement approach for a burning plasma experiment. The tokamak concept is outlined in Fig. 2.1. The plasma is confined in two superimposed magnetic fields: the toroidal field B_φ generated by external poloidal coils and poloidal B_θ generated by a toroidal current in the plasma. Therefore, magnetic field lines run helicoidally, as it is shown in Fig. 2.1, and the magnetic configuration of tokamak presents an infinite set of nested magnetic flux surfaces.

Apart from the toroidal and poloidal fields, the need for a vertical component of the magnetic field arises in order to maintain the horizontal stability of a plasma torus. The Lorentz force of the toroidal plasma current in the vertical field provides the inward force that holds the plasma in equilibrium.

The toroidal current is induced by slowly increasing the current through an electromagnetic winding linked with the plasma torus: the plasma can be considered as the secondary winding of a transformer. Therefore, this is inherently a pulsed process because there is a limit to the current through the primary. Tokamaks must therefore rely on other means of heating and current drive.

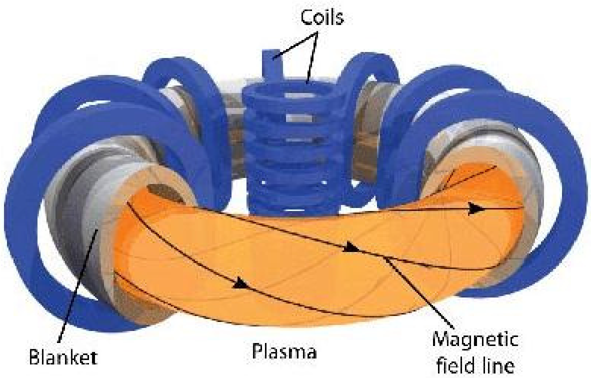

Figure 2.1: Tokamak concept. The innermost cylindrical 'coils' are the transformer coils for inducing a plasma current. The 'plasma' column is indicated by yellow colour torus. The coils along the torus are used to generate the toroidal magnetic field. The helical 'magnetic field line' results from overlapping of the toroidal (B_ϕ) and poloidal (B_θ) fields.

The properties of the field lines are characterized by the safety factor q defined by

$$q = \frac{number\ of\ toroidal\ windings}{number\ of\ poloidal\ windings} \tag{2.1}$$

of a field line on the torus.

In the limit of the screw-pinch , the relation:

$$q \approx \frac{r\,B_\varphi}{R\,B_\theta} \tag{2.2}$$

holds, r is the minor plasma radius and R is the major plasma radius. At places with low rational safety factor instabilities can easily arise.

To keep the plasma temperature sufficiently high the plasma is heated using several methods: ohmic heating due to the plasma current, microwave heating and neutral beam injection.

2.1 The TEXTOR tokamak

TEXTOR (Tokamak Experiment for Technology Oriented Research) is a medium sized limiter tokamak. It is dedicated primarily to the study of plasma wall interaction. ~~The major radius $R_0 = 175\ cm$ and minor radius $a = 47.5\ cm$.~~ The plasmas in TEXTOR have a circular cross section and last for up to 10 s. ~~Magnetic fields of up to 3 T and plasma currents up to 800 kA are possible, although the typical~~

~~values are 2.25 T and 300 kA, respectively.~~ Table 2.1 lists the main machine parameters of TEXTOR as well as typical parameters of ohmic discharges that have been analysed in the course of this work. The inside view of TEXTOR is presented in Fig. 2.2.

TEXTOR parameters	Value
a [cm]	47.5
R [cm]	175
B_T [T]	$1.6 - 2.6$
I_p [kA]	$200 - 350$
$\bar{n}_e(0)$ $[m^{-3}]$	$(1 - 3.5) \times 10^{19}$
$\bar{T}_e(0)$ $[keV]$	~ 1
q_a	$2.9 - 6.3$

Table 2.1: The typical TEXTOR plasma parameters for experiments of this work.

The TEXTOR tokamak has a double walled chamber. The liner (inner wall) is mounted at the average distance of 70 mm from the vacuum vessel (outer wall). Two wall conditioning techniques are applied in TEXTOR for impurities and hydrogen removal from the liner. They include (i) a ~~thermal~~ baking of the vacuum vessel, (ii) glow discharge cleaning. For thermal baking, direct current is fed into the liner from two opposite toroidal positions. Baking is performed at 300 °C routinely while the maximum temperature is 500 °C. Another technique to reduce the impurity influx from the wall is the deposition of the protective film on the vessel (boronization).

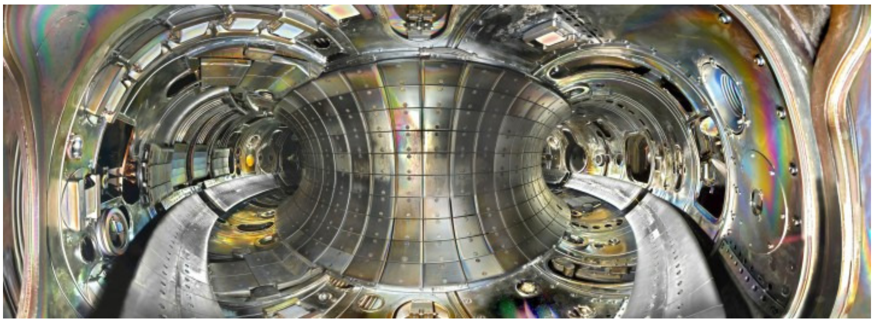

Figure 2.2: View inside the vacuum vessel of TEXTOR. In the central part of the photo, the fully toroidal bumper limiter covers most of the high field side surface of the wall. At 45° below the equatorial midplane, several blades of the ALT-II pump limiter are visible.

TEXTOR is equipped with several limiters to protect the liner from the plasma energy. First of all, the Advanced Limiter Test-II (ALT-II) of TEXTOR is a full toroidal belt limiter mounted 45° below the equatorial plane on the low field side. The minor radius of TEXTOR plasmas is defined primarily by this ALT-II limiter. Meanwhile, on the high field side of the vessel the fully toroidal bumper limiter covers about one third of the wall surface and protects it from the deposition of the plasma energy in case of a disruption.

3 The gas puff imaging diagnostic and Langmuir probes

The aim of this chapter is to report on implementation details of the Gas Puff Imaging (GPI) system on the TEXTOR tokamak. It has been mentioned in section 1.1 that the turbulence in magnetized plasmas is essentially two-dimensional, This imposes essentially two-dimensional turbulence measurements. Two methods are commonly used for 2D turbulence measurements: Langmuir probe arrays [8–10] and beam emission spectroscopy (BES) [11, 12]. However, the spatial resolution of a BES diagnostic is not high enough and Langmuir probes can not penetrate very deep into the hot plasma. Gas puff imaging presents an interesting alternative as it is not subject to some of the drawbacks of other systems. In the present work, we refer to a GPI system as a system with an observation direction along the magnetic field line, as introduced in pioneering works in Refs. 44, 45. Over the past 10 years some essential progress in GPI systems has been made, but so far the diagnostic has only been implemented in diverted tokamaks and linear machines [44–46]. Within the frame of this PhD project, the GPI system has been designed and implemented at TEXTOR. We have to emphasize that the TEXTOR GPI diagnostic is the first implementation of the GPI system on a limiter tokamak.

Meanwhile, at the end of this chapter we present a brief description of the fast reciprocating Langmuir probe system at TEXTOR. This probe can provide radial profiles of density, electron temperature, floating potential and the electric field in the plasma edge with high spatial resolution. Therefore, this probe diagnostic, along with the recently developed GPI system, is an important tool for our studies of turbulence in the plasma edge.

Section 3.1 describes details of the engineering design as well as basic physical principles that underlie GPI measurements. Some fundamental limitations and diagnostic issues will be discussed in section 3.2. In section 3.3 first measurements of the 2D turbulence dynamics in the edge of TEXTOR are reported. Section 3.4 presents a short description of the Langmuir probe system at TEXTOR.

3.1 The engineering design of the GPI system

The gas puff imaging diagnostic has been used previously in Alcator C-Mod, NSTX and EAST; see [32, 44, 45, 47] and references therein. A neutral deuterium (D) cloud is puffed into the edge plasma region. The visible light emission from the gas cloud is then imaged with a fast framing camera with exposure times (typically of the order of few μs) shorter than the life-time time of the turbulence in order to track the motion of turbulent structures.

A schematic illustration of the GPI geometry (top view) is shown in Fig. 3.1. A neutral gas cloud is puffed continuously in the vacuum chamber for half a second through the gas inlet nozzle installed on the liner. The light emitted by the gas cloud is observed via a telescope, installed on the equatorial plane nearby the nozzle (see also Fig. 3.2) at a toroidal distance of 45.6 cm ($L_{cloud} \approx$ 45.6 cm). With this configuration we obtain a viewing area 12 cm in diameter at the cloud plane. The system is adjusted so that the separatrix passes through the middle of the observation area and divides the view field in two approximately equal parts corresponding to the edge and the SOL plasmas. Therefore, the evolution of turbulent structures, from the birth in the edge to the fast decay in the SOL can be observed.

After passing through the telescope optics, the light is guided to the objective of the fast frame camera, installed 1.3 m away from the TEXTOR vessel. A D_α optical filter (656 nm), installed in front of the charge-coupled device (CCD) chip, is used to discriminate the brightest deuterium line ($n = 3 \rightarrow 2$ transition in the Balmer series).

Figure 3.2 shows the in-vessel components of the GPI system. The observation direction of the telescope system is along the local (at the gas puff cloud) magnetic field line, which has a pitch angle $\alpha \approx 2.5°$ with respect to the horizontal plane. This value is estimated for $r = 47.5\ cm$, $I_p = 250\ kA$ and $B_T = 2.25\ T$.

The gas injection system is composed of a deuterium molecules reservoir and the tubing system that connects the reservoir to the exit nozzle. The nozzle is installed inside the TEXTOR vessel (fixed on the liner) at a radial position (minor radius) $r \approx 53\ cm$ ($5.5\ cm$ outside of the last closed flux surface (LCFS)). The tubing system consists of external and invessel tubes. The interface between both tubes (the gas injection entrance port) is a short “Vespel” tube to ensure electrical

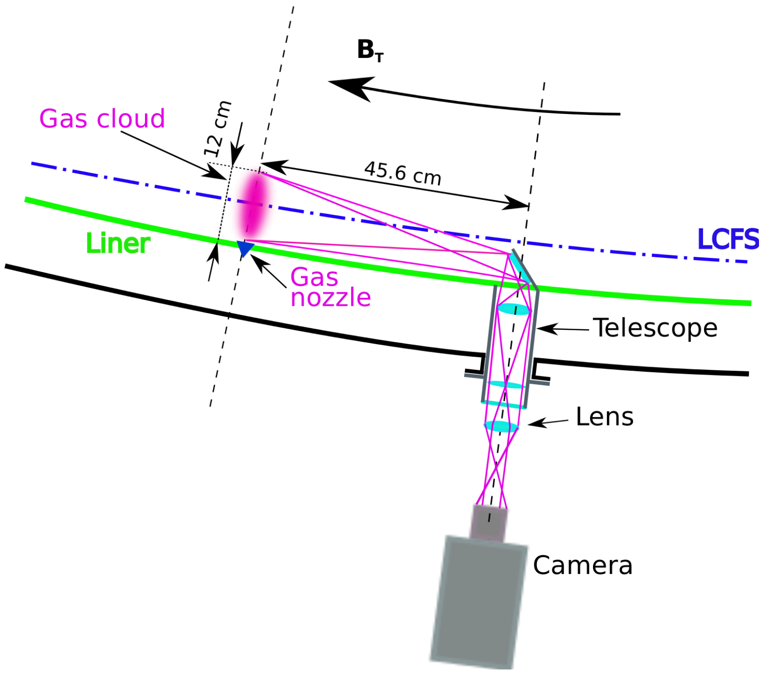

Figure 3.1: Schematic illustration (top view) of the GPI system in TEXTOR. The emission from the gas cloud is viewed along the local (at the puff) magnetic field line by an optical telescope, installed in the vessel. The observation covers a view field 12 cm in diameter in the radial vs poloidal plane from the plasma edge to the wall. The light passes through the telescope's lenses and is guided to the fast frame camera installed about 1.3 m away from the TEXTOR vessel.

insulation between the vacuum vessel and the outside hardware. The external tube is 6 mm inner diameter, 7 m long stainless steel tube. The in-vessel one is 6 mm inner diameter, 0.5 m long stainless steel flexible tube. This flexibility is necessary to remove mechanical tensions in the tube raised by bakeout heating or disruptions.

One of the novel features of our GPI system is the reduced divergence angle of the gas puff flow. It is always reasonable to reduce the divergence of the GPI gas flow. This is primarily due to two reasons. First, the measured intensity is line-integrated along the line of sight and large extension of the cloud leads to an additional difficulties in interpretation of results (due to nonlocal measurements). Second, a large extension of the gas cloud leads to the fraction of gas puff neutrals that are not in the view field of GPI optics, and these neutral atoms produce an additional perturbation in plasma properties. Despite these concerns, the divergence issue has not been considered in the design of the GPI system at NSTX and Alcator C-Mod whereas low divergence gas-puffing systems based on the supersonic-type

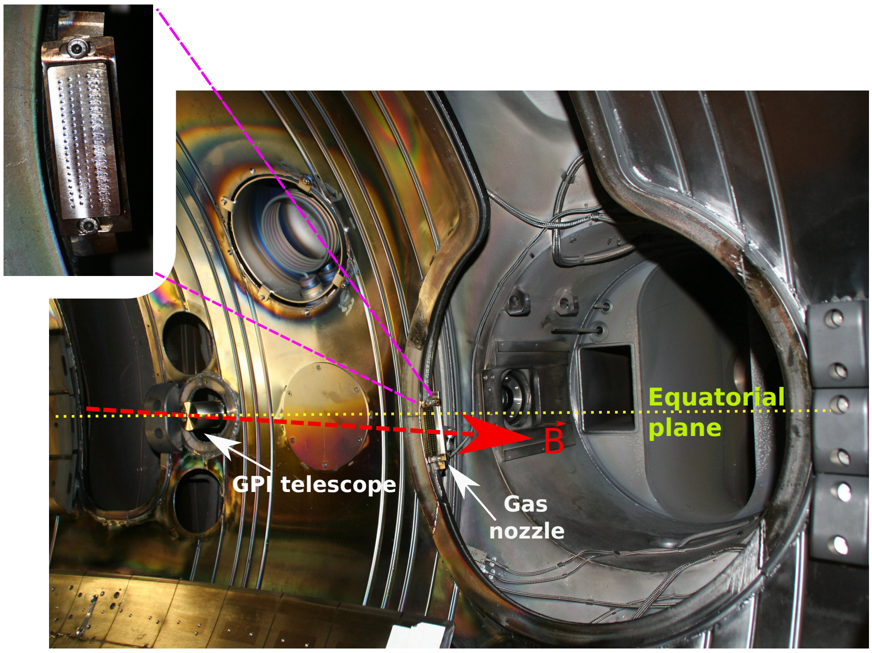

Figure 3.2: In-vessel components of the GPI system at TEXTOR. The neutral gas enters the chamber radially via the gas-puff nozzle. Its emission is viewed along the local (at the gas cloud) magnetic field ($\vec{B}$) by a telescope installed in an equatorial port at a distance of $45.6\ cm$ from the gas inlet nozzle. The inset at the top shows the capillary gas inlet nozzle composed of 100 holes each with a diameter of $0.5\ mm$.

nozzle are widely used in many machines (for instance in LHD and TEXTOR).

In our experiment, in order to reduce the divergence, we used "shower-like" multi-capillary source made up of 100 holes mechanically drilled in a rectangular matrix, that has the size of $2 \times 6\ cm^2$. Each hole has the diameter of $d = 0.5\ mm$ and the length of $L = 15\ mm$ (aspect ratio $A = L/d = 30$). The plasma facing side of the nozzle is zoomed in the inset of the figure 3.2. The holes are drilled in the orthogonal stainless steel bar.

Alternatively, the stack of stainless steel hypodermic needles (or standard capillary tubes available in the industry), laser drilled holes and a supersonic De Laval nozzle can be implemented to make the beam more unidirectional. However, a practical implementation of these approaches is more costly and time-consuming. Our choice is the compromise between improving divergence of the gas flow and minimising fabrication costs of the nozzle.

Another novel feature of the GPI system at TEXTOR is the in-vessel GPI opti-

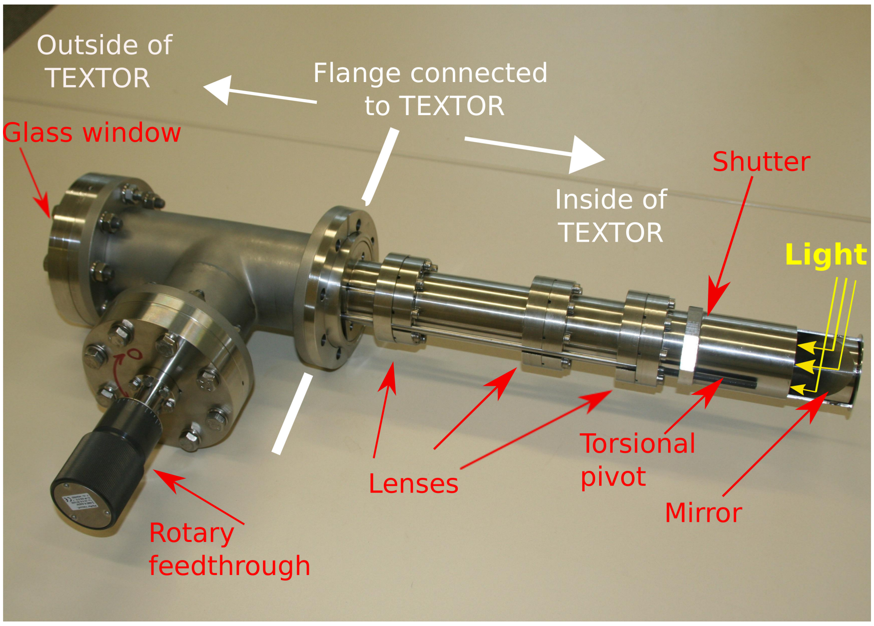

Figure 3.3: (a): The photo of the GPI telescope.

cal telescope, which is implemented to protect in-vessel optical components from coating and severe thermal loads. The feature of this telescope is that it is designed to sustain severe thermal loads and coating. It should be noted that the in-vessel telescope has not been implemented on the GPI systems in Alcator C-Mod and NSTX. In Alcator C-Mod, a simple GPI telescope ~~has been~~ was used together with an in-vessel fiber optic bundle. However, the fiber optic light guides can be gradually ~~contaminated~~ destroyed by heat load in hot plasmas and radiation fluxes (neutron and x-ray fluxes). For instance, the GPI glass fiber optic bundles in Alcator C-Mod has been replaced in 2009 due to radiation darkening, most likely due to the high x-ray fluxes generated in C-Mod plasmas [48]. Our telescope is free of these drawbacks.

Figures 3.3 and 3.4 show the assembly of the optical telescope. From right to left we indicate main components of the telescope: the mirror, the shutter, lenses, the rotary feedthrought and the glass window. All in-vessel lenses are held in telescope by fluoroplastic rings with the radial thickness of 1 mm to avoid cracking of lenses due to the thermal expansion. The diameter of telescope lenses is limited by the inner diameter of the TEXTOR flange (CF63). Therefore, all optical components of the telescope have diameter of 40 mm.

The telescope works according to the next description: the light emitted by the

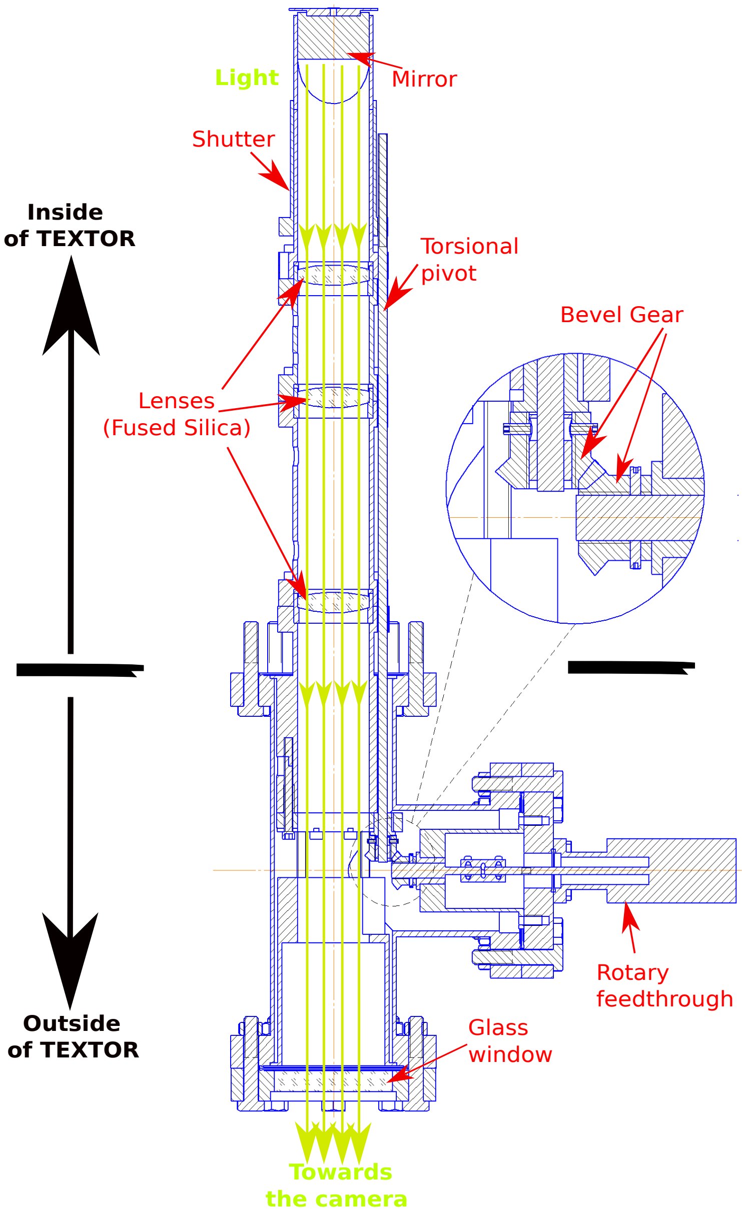

Figure 3.4: The section drawing of the GPI telescope system sketching its internal design and the light propagation.

gas cloud (marked with yellow arrows) is collected by the mirror and focused with several lenses; After light passes through lenses, it goes through the glass window

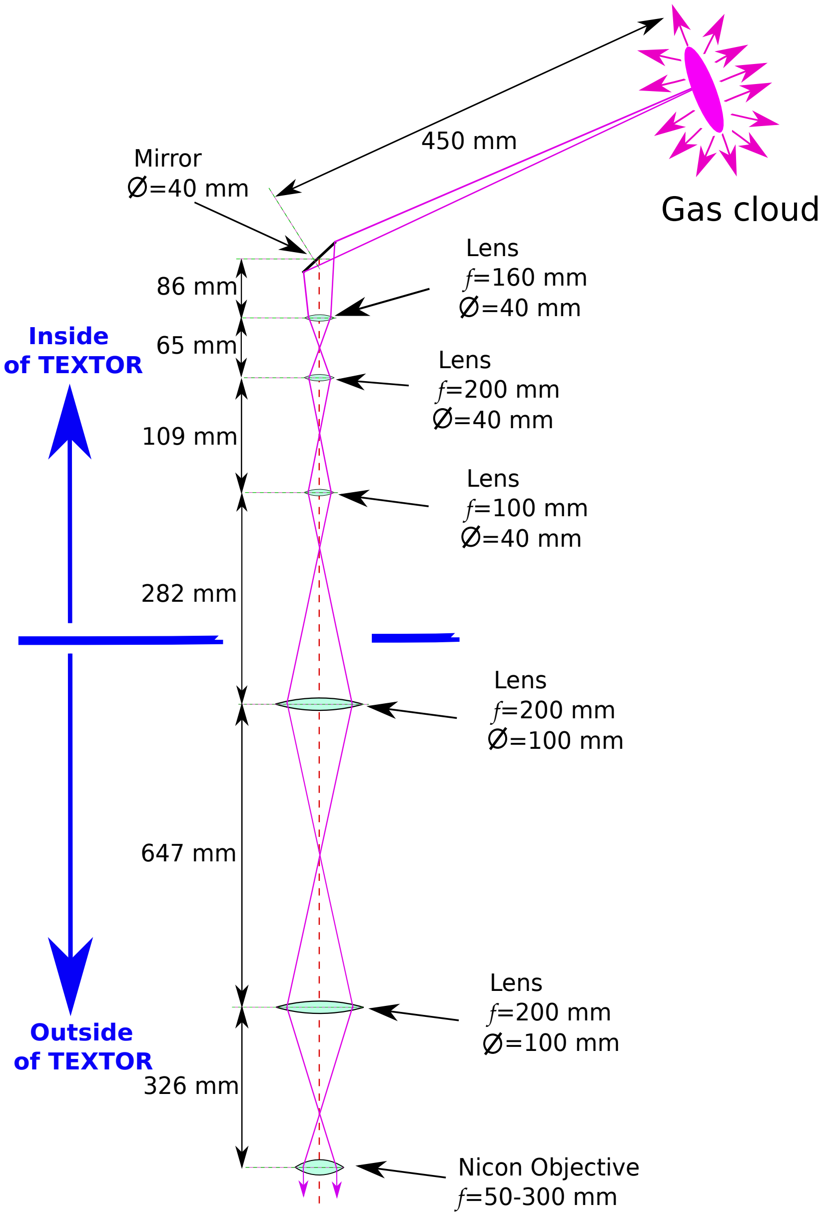

Figure 3.5: The optical design of the GPI system. This design was created using the "ZEMAX" optical design software.

towards the fast frame camera (not shown in the figure) installed about 1.3 m away from the TEXTOR flange. The most internal part, the mirror, undergoes a severe transient thermal load and a particle flux on its surface. Therefore, it is made as polished 0.5 mm thick stainless steel plate. To prevent the coating on the telescope mirror, a protective shutter has been installed on the telescope head as also shown in figures 3.3 and 3.4. The rotary feedthrought, bevel gear, and torsional pivot are installed to handle the position of the shutter. The shutter is connected to the torsional pivot and linearly moves along the telescope axis when the pivot rotates. A torque is transmitted from rotary feedthrought to the pivot via the bevel gear. While rotating the feedthrought, the shutter can be moved in the position either to cover and protect the mirror or open it for measurements. The mirror is shuttered off during the glow discharge cleaning, boronization and other experiments when coatings can be deposited on the mirror surface.

The optical design of the GPI system is shown in Fig. 3.5. It was designed using the "ZEMAX" optical design software, which provides complete information about abberations, spot sizes and quality of the designed optics in general. In contrast to GPI systems in NSTX and Alcator C-Mod, we do not use a fiber bundle to connect the camera to the telescope in order to avoid as much as possible loss of light and aberrations in the final image. A PSI-5 fast-frame camera [45] with a 64×64 pixel CCD detector has been used with exposure times from 2 to 6 μs, chosen in function of the plasma parameters (higher plasma densities lead to higher emission and thus to lower exposure time).

All in-vessel lenses are ready-made commercial lenses made of fused silica to sustain high in-vessel temperatures. The high melting point (1723 °C) and low thermal expansion coefficients of fused silica account for its ability to sustain high temperatures (applied, for instance, for the TEXTOR wall conditioning 250-600 °C) and rapid temperature changes, caused by disruptions or runaway electrons. The latter two events may significantly raise the temperature up to the melting point. The maximum working temperatures of fused silica is 1000 °C. Although there are several glass types with even higher working temperatures (maximum working temperature of sapphire lenses up to 2000 °C), the choice of the fused silica is the compromise between the wide availability of standard lenses made of this material and a heat resistance of this material. In addition, all in-vessel lenses are uncoated to avoid the degradation of coatings in high temperature conditions.

3.1.1 Optical resolution

Several technical aspects contribute to the optical resolution of the system: optical aberrations, the misalignment of the line of sight with respect to the local magnetic field line direction, number of pixels in the camera sensor. Let's discuss these contributions one by one.

- Aberration leads to deformation(distortion) and blurring of the image produced by an image-forming optical system.

Distortion
The maximum relative distortion (obtained from the distortion plot of optical design software) of the optical system is 0.07 $\%$. Projecting this value onto the object plane and taking into account the diameter of the observation view ($L_{obj} \approx 12\ cm$) gives the absolute deformation of the measured object of $R_{dist} \approx 0.08\ mm$.
Blur spot
The maximum ray spot size of the optics is $S_{sp} \approx 0.15\ mm$ in the periphery of the image plane and it is much smaller near the centre. This is also obtained from the spot diagrams and transverse ray aberration plots of the design software. Taking into account the magnification factor M of the system gives the geometric blur size in the object plane. The optical magnification factor M, as the ratio between the imaged size of the object (equals to the camera CCD chip size $L_{img} = 18\ mm$) and its real size in the object plane (L_{obj}), has been obtained $M = L_{img}/L_{obj} = 18/120 = 0.15$. Therefore, the contribution of the ray spot size to the spatial resolution of the optical system is $R_{sp} = S_{sp}/M \approx 1\ mm$.

Thus, it is visible that $R_{sp} \gg R_{disp}$ and therefore the contribution of aberrations to the spatial resolution is defined primarily by blur spot size $R_{abb} \approx R_{sp}$.

- Another issue, relevant to the spatial resolution, is the misalignment of the observation view with respect to the magnetic field line direction due to finite viewing angle of the telescope (in our case $\alpha \approx L_{obj}/L_{cloud} \approx 15.2^o$). When the line of sight is not parallel to the field line direction, this causes the loss of the poloidal resolution when observing the turbulent structures which lie along this field line. The resolution degrades gradually with increase in the neutral gas cloud size in the line of sight direction. In the TEXTOR tokamak, the extension of the gas cloud along the magnetic field line direction is $\sim 5\ cm$. For various combinations of q values in TEXTOR, the pitch angle at the gas cloud varies in the range of 2.3^o - 4.2^o, which corresponds to the poloidal resolution 5 mm - 10 mm within the view field of our optics. On the other hand, as long as the pitch angle remains close to the 2.5^o, from which the gas cloud is observed, the poloidal resolution due to misalignment linearly grows from 0 in the centre of the view field to 5 mm on its edge. In the majority of our GPI experiments the pitch angle varies within the range of 14% of the typical value.

- Another contribution to the spatial resolution is the limited number of pixel in the camera sensor (only 64 in each direction). This corresponds to the spatial resolution of $R_{cam} = L_{obj}/64 \approx 2.0\ mm$, which is even higher than the resolution defined by the optical aberrations $R_{cam} > R_{abb}$. This value cannot be improved unless another CCD camera is used.

Therefore, the total optical resolution is determined mainly by low pixel number in the CCD sensor and it gradually degrades from 2 mm (dictated by low pixel number) in the centre of the view field to 5 mm on its edge (dictated by non parallel line of sight).

Looking further forward, we ~~are meant~~ intend to use more advanced CCD cameras with higher number of pixels. In that case, the low number of pixels will not be the factor limiting the spatial resolution of the system anymore and, instead, the resolution will be determined by optical aberrations (R_{abb}). Therefore, it is reasonable to discuss some aspects which limit R_{abb}.

Optical aberrations could be significantly reduced by increasing the distance between the telescope and the gas cloud L_{cloud}, thus reducing the angular extent of an imaged cloud and hence approaching the paraxial approximation [49]. However, this measure leads to a reduction of the *object space numerical aperture* (NA) of the system and hence its light-gathering ability. The actual price paid for the reduction of the NA (the amount of light) is the enhanced gas puff flux and hence enhanced perturbation of the background plasma, which is not desired in all cases. The NA value of our optical periscope system is equal to 0.031. The NA value would be higher if we used larger diameter lenses. However, as already mentioned above, the diameter of periscope lenses is limited by the inner diameter of the TEXTOR flange.

Taking these arguments into consideration, the distance between the gas cloud and the telescope mirror was chosen as a compromise between low aberrations (better resolution) of the distant imaging and decrease of the GPI signal intensity with increasing distance.

3.1.2 Some aspects of atomic physics relevant to GPI measurements and a typical GPI frame

The kinetics of the population of atomic levels for typical edge plasma parameters is described by collisional-radiative (CR) models [50,51]. The basic assumption of the CR model is that states above the ground state will decay much more rapidly than the ground state will change. Based on this, the emission intensity ϵ from the gas cloud is proportional to the ground-state density n_0 (i.e. the local density of neutrals in the gas cloud) and, in general, a nonlinear function of the electron density n_e and temperature T_e:

$$\epsilon(photons/m^3) = n_0 f(n_e, T_e) A \tag{3.1}$$

where A is the radiative decay rate from the excited electron states (Einstein coefficient) and $f(n_e, T_e)$ is a nonlinear function of T_e and n_e. Therefore the light emission from the plasma is modulated by both the local T_e and n_e fluctuations.

The CR modelling of a molecular deuterium is very complex due to many atomic processes such as dissociation, ionisation, excitation, dissociative excitation and others. Therefore, the modelling of these processes is beyond the scope of this work. In this section, we would like to just mention some typical molecular processes proposed in articles [52–56], in which two types of dissociation reactions are used to explain the production of deuterium atoms:

$$D_2 + e^- \rightarrow D^*(n = 3, 4, 5) + D + e^- \tag{3.2}$$
$$D_2 + e^- \rightarrow D_2^+ + e^- + e^- \tag{3.3}$$

The reaction (3.3) requires the subsequent collisional dissociation to produce one deuterium atom:

$$D_2^+ + e^- \rightarrow D^+ + D^*(n = 3, 4, 5) + e^- \tag{3.4}$$

Meanwhile, the atoms in the ground state can be excited again:

$$D + e^- \rightarrow D^*(n = 2, 3, 4, 5..) + e^- \tag{3.5}$$

The produced deuterium atoms or other excited ones from the ground state after decay will produce Lyman (transition to $n = 1$) and Balmer (transition to $n = 2$) series. Among them, transitions $n = 3 \rightarrow 2$ contribute to the D_α signal.

3.1.2.1 Typical GPI image

All of these aforementioned processes are relevant to the production of the D_α emission, which is measured by the GPI system. A typical single GPI frame is shown in Figure 3.6(a). This image was measured with an exposure time of 6 μs in a deuterium cloud. It corresponds to an ohmic discharge with $\bar{n}_{e0} = 3.5 \times 10^{19}$ m^{-3}, $I_p = 350$ kA and $B_T = 2.6$ T. The artificial colour scale (right) has been used to effectively recolor the original grayscale camera image. The x-axis displays the radial extension of the viewing area in terms of the TEXTOR minor radius. The position of the separatrix is shown in the figure along with the poloidal extension (z) of the view field. The radial position of the LCFS in the GPI frame was determined empirically from the radial calibration of the GPI optics. The cm-scale yellow colour structures in this image correspond to turbulent eddies.

Figure 3.6(b) shows the 300-frames averaged radial profile of the D_α emission intensity (I_{camera}) measured in the same shot as the one of figure 3.6(a). In the following part we will make some attempts to understand qualitatively the emission profile in figure 3.6(b).

The first thing to notice here is that reactions 3.2-3.5 show that the D_α emission in molecular deuterium is very complex and one needs to make some assumptions in order to explain the observed emission profile. In particular, we will simplify our consideration by making the following assumptions:

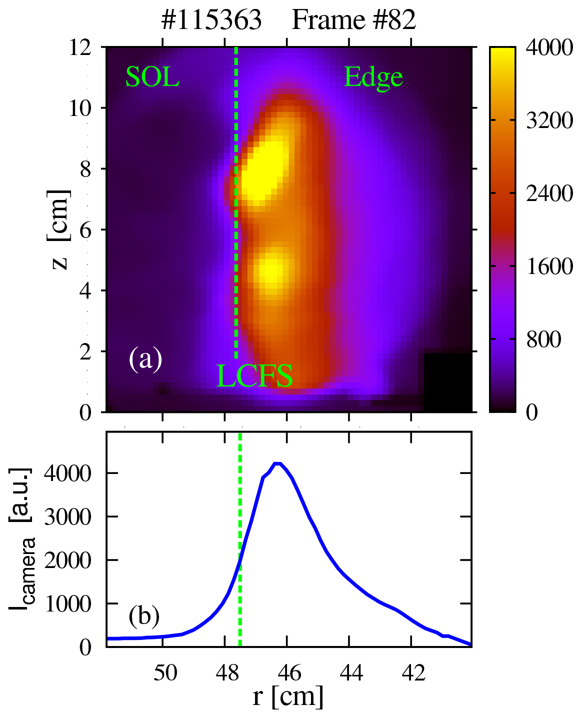

Figure 3.6: (a) A single frame of the GPI showing the D_α light emission from the neutral deuterium cloud viewed by the optical telescope. The viewing area of the telescope covers $\approx$ $12\ cm \times 12\ cm$ in the poloidal (z) vs radial plane (r). The frame is taken at an exposure time of 6 μs. The separatrix position is shown by the dashed green line. (b) The 300-frames averaged radial profile of the D_α emission measured with the GPI.

- the D_α emission is produced by neutral deuterium atoms, preliminary excited by electron impact. In other words, we consider only the reaction 3.5 and ignore all dissociation processes 3.2-3.4. This is a very rough assumption, taking into account that the major contribution to the D_α spectra is produced by the molecular dissociation (coupled with a dissociative excitation) [55, 56] in reactions 3.2-3.4. This assumption also implies that, from the very beginning, we consider deuterium as an atomic (rather than molecular) gas.

- We assume that we are really dealing with an unidirectional beam of atoms (with the density n_0 and velocity v_0). This is a very rough assumption, taking into account that we are in fact concerned with molecular deuterium, and a molecular dissociation yields a corresponding FranckCondon energy (certain kinetic energies for the dissociation products). Therefore, in reality, produced deuterium atoms will fly in all directions and the resulting cloud is far from being unidirectional.

- We assume that the coronal model [50, 57] is applicable to analyse the population of atomic levels of deuterium atoms. The basic idea in the coronal model is that the depopulation of excited levels occurs only by radiative decay, population occurs by electron collisions.

Following these assumptions, in the steady-state, the D_α emission intensity is given by [50, 57]

$$\epsilon(r) \sim n_e(r)n_0(r)\langle\sigma_{1\to3}v_e\rangle \tag{3.6}$$

with $\langle\sigma_{1\to3}v_e\rangle$ denoting the excitation rate from the ground state of a deuterium atom. The line emission $\epsilon(r)$ is monotonically increasing function of the local electron density n_e and temperature T_e. However, the density of neutral atoms n_0 is attenuated towards the centrum by ionization of molecules and atoms on account of electron collisions. This is visible from the equation for the ionisation rate per unit volume

$$\frac{dn_0}{dt} = n_e(r)n_0(r)\langle\sigma_i v_e\rangle. \tag{3.7}$$

Here, $< \sigma_i v_e >$ is the cross-section of ionisation from the ground state by electron collisions. In the steady-state, this equation can be rewritten:

$$v_0\frac{\partial n_0}{\partial r} = n_e(r)n_0(r)\langle\sigma_i v_e\rangle, \tag{3.8}$$

Therefore, two quantities n_e and n_0 included in the expression for $\epsilon(r)$ have opposite radial dependencies, which results in the peaked $\epsilon(r)$ profile as shown in Fig. 3.6(b). It is clear that the GPI can only be applied in the vicinity of the separatrix.

We have to notice that the GPI-measured emission intensity in figure 3.6(b) qualitatively agrees with the measured D_α light emission profile in C-mod [44] as well as with the results from DEGAS 2 simulations for that machine. In particular, their widths (FWHM) are 2.5 cm at TEXTOR and 2 cm at C-Mod and they are both localised in the near vicinity of the separatrix: 1.5 cm deeper than LCFS at TEXTOR and 0.5 cm farther at C-Mod. This result is not so obvious because mean time-averaged $I_{camera}(r)$ profile is defined mainly by the edge $T_e(r)$ and $n_e(r)$ profiles and despite of similar $T_e(r)$ radial profile on both machines (typical values are 20-30 eV on TEXTOR and 20-30 eV on C-Mod), the corresponding $n_e(r)$ profiles differ from each other by approximately one order (2.5×10^{12} cm^{-3} on TEXTOR and 3×10^{13} cm^{-3} on C-Mod).

These results might be explained in the context of a simple coronal model mentioned above. Let's assume that the whole $n_e(r)$ profile increased several times. The collisional excitations are more intense the higher the $n_e(r)$ values ~~are~~, according to equation (3.6). On the other hand, the ionization frequency also grows with $n_e(r)$ making neutral particles out of the game, according to equation (3.8). Therefore, increased $n_e(r)$ profile results in the $I_{camera}(r)$ profile shifted radially outward whereas the width and typical values of the emission intensity profile might be approximately the same. In other words, all collisional processes enter into the game earlier along the track of particles.

Note, however, that turbulent structures do not affect the whole $n_0(r)$ profile. At TEXTOR, the typical radial and poloidal sizes of turbulent structures in the plasma edge is $\sim 2\,cm$, as one can see for instance in Fig. 3.6(a). The typical level of edge plasma density fluctuations, relative to the mean time-averaged value, is $\sim (20-30)\%$. The local 20% increase in n_e does not change significantly n_0 because n_0 and n_e are related through the differential equation (3.8). However, it will rise the emission intensity by 20%, according to linear relation in Eq. (3.6). Therefore, turbulent structures do not affect significantly $n_0(r)$ profile and the emission intensity is modulated only locally.

3.2 Limitations of the diagnostic

One key requirement for a GPI system is that the gas puff ~~does not~~ affects neither the local and global plasma parameters nor the turbulence properties. Meanwhile, it should provide sufficient emission. To investigate the impact of the gas puff on the local plasma parameters we used a fast reciprocating Langmuir probe mounted at the midplane on the low field side of TEXTOR [58], toroidally $22.5°$ ($86\,cm$) away from the GPI gas nozzle. Due to this small toroidal distance, the local perturbation of the gas puffing on equilibrium plasma parameters can be seen by the probe as well.

In Figure 3.7, we present results for an omhic discharge where we plunge the fast probe twice within one shot: without (blue line) and with the gas puff (red line). The left column shows the results for a gas flux of 1.2×10^{20} molec/s, while the right column corresponds to 2.3×10^{20} molec/s. Figures 3.7 (a) and (b) depict the equilibrium electron density for a radial range of 49.8 cm $> \rho >$ 45.5 cm, including the SOL and the plasma edge. There is no visible difference between the results obtained with and without gas puffing. This is true even for the high flux in Fig. 3.7(b). The same is valid for the equilibrium electron temperature as can be seen in figures 3.7 (c) and (d), where no visible local cooling of the plasma is observed due to energy losses on dissociation, ionization and excitation processes.

To check whether the edge turbulence is affected, we compared the frequency spectra of $\tilde{\phi}_{fl}$ and $\tilde{I}_s$. The FFT spectra of $\tilde{\phi}_{fl}$ for two puffing flux values are compared in figures 3.7(e) and (f) and show little difference. However, whereas the spectra $S_{\tilde{I}_s}$ in Fig. 3.7(g) show little difference in low puffing case, for high puff flux the spectrum of $\tilde{I}_s$ in Fig. 3.7(h) is clearly affected. From this we conclude

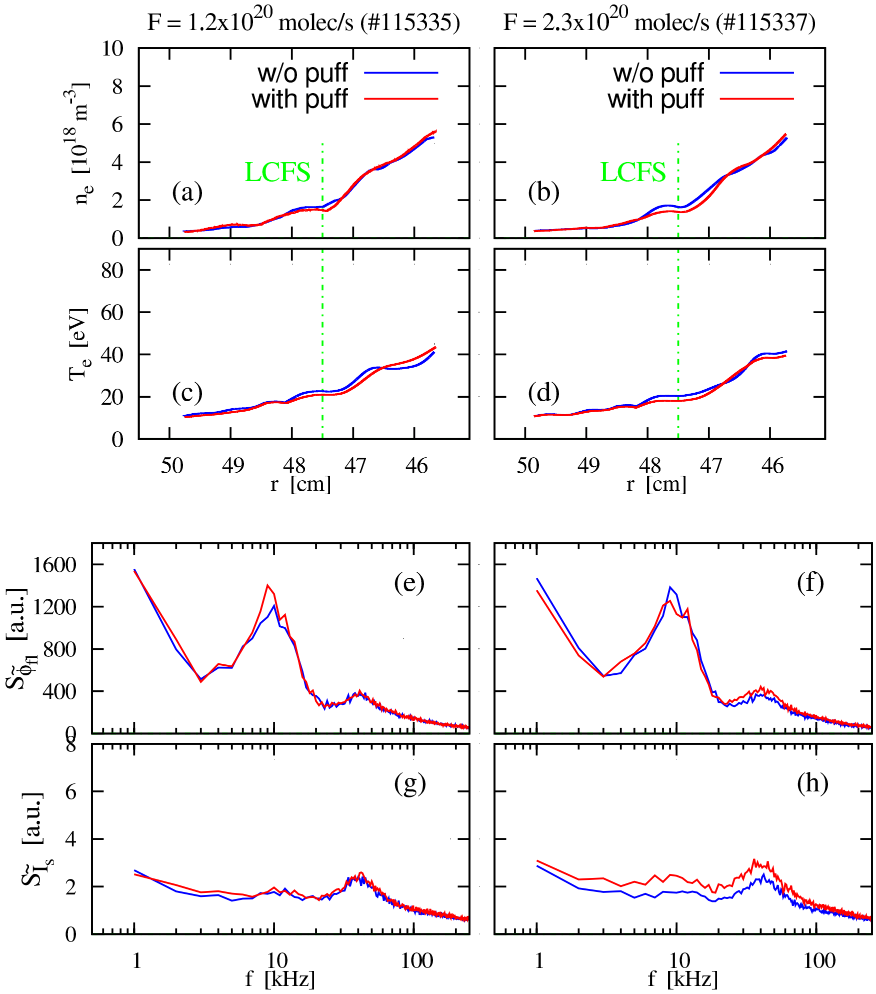

Figure 3.7: (a)-(d) Radial profiles of electron density and temperature measured by a Langmuir probe with (blue) and without (red) local gas puffing. (e)-(h) Power spectra of the floating potential fluctuations ($S_{\tilde{\phi}_{fl}}$) and ion saturation current fluctuations ($S_{\tilde{I}_s}$). The left column shows results for a gas flux of 1.2×10^{20} molec/s while the right column for 2.3×10^{20} molec/s.

that the GPI system on TEXTOR is suited to the operation in low gas puff flux level in order to minimize the perturbing effect of the puff cloud on plasma turbulence.

In order to study the influence of the gas puff on the global plasma parameters, we compared the line-averaged densities $\bar{n}_e$ without (black lines) and with gas puffing (red lines). The results are shown in Fig. 3.8. In all cases the puffing flux

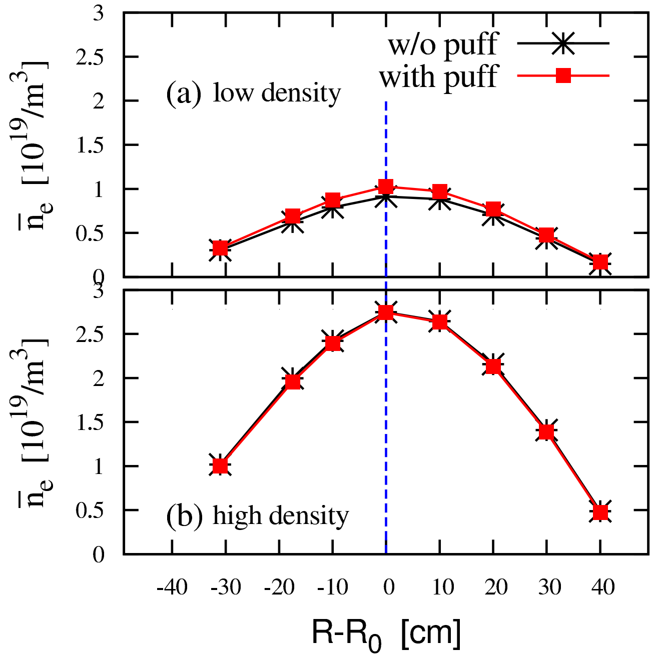

Figure 3.8: Comparison of the line-averaged density $\bar{n}_e$ obtained with and without the gas injection (the puffing flux is 1.0×10^{20} molec/s). The results of this figure show that the low density shot can be easily perturbed by the gas puffing than the high density shots. Consequently, the working gas puff flux level for all range of plasma densities should be as low as 1.0×10^{20} molec/s.

is 1.0×10^{20} molec/s. In low density shots (see Fig.3.8(a)), results show clear difference between two profiles, while in the high density discharges (see Fig.3.8(b)) the difference in $\bar{n}_e$ is almost invisible. Thus, low density shots are more sensitive to perturbations from the GPI gas injection. This might be explained as follows: at TEXTOR the central line-averaged density $\bar{n}_{e0}$ is feedback controlled by the internal TEXTOR gas inlet system. In low density shots ($\bar{n}_{e0} = 1.0 \times 10^{19}\ m^{-3}$)(Fig.3.8(a)) the TEXTOR internal gas inlet system supplies continuously around 7×10^{19} molec/s in order to stabilize the line-averaged density. High density shots ($\bar{n}_{e0} = 3.0 \times 10^{19}\ m^{-3}$)(Fig.3.8(b)) need around $(8-9) \times 10^{19}$ molec/s to remain stationary. Therefore, the GPI gas-puff flow and the TEXTOR internal gas-flow are comparable and the established line-averaged density is the result of the competition between these two systems. In high density shots, the GPI gas inlet system simply replaces the TEXTOR gas inlet system so that the net effect is the same. In low density shots, the lower internal TEXTOR gas flow rate is overshadowed by the GPI gas flow leading to a visible increase in the line-averaged density. We should therefore limit the puffing flux to 7×10^{19} molec/s. In practice, we operate in the range of $(6-8)\times 10^{19}$ molec/s, depending on the plasma parameters.

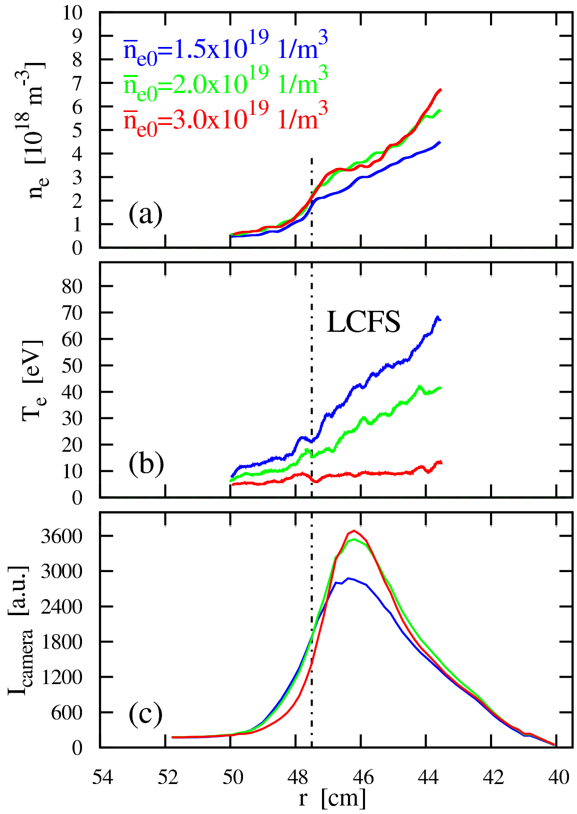

Figure 3.9: Comparison of the equilibrium radial profiles of (a) electron density n_e, (b) electron temperature T_e and (c) the 300-frames averaged radial profile of the D_α emission measured with the GPI. Each figure shows three profiles obtained for shots with different central line-averaged densities.

We now come to the discussion of the dependence of the emission intensity of the gas cloud on the local plasma parameters. Figure 3.9 compares the equilibrium radial profiles of (a) electron density n_e, (b) electron temperature T_e (measured with the fast reciprocating Langmuir probe) and (c) the 300-frames averaged D_α emission intensity I_{camera} (measured with the GPI), corresponding to three shots with different central line-averaged densities $\bar{n}_{e0} = 1.5\times10^{19}$, 2×10^{19}, 3.0×10^{19} m^{-3} (I_p and B_T are the same). The D_2 puff flows for all three shots are the same and, due to $I_{camera} \propto n_0$, we can directly compare I_{camera} for different plasmas. It is important to note that while figure (b) shows apparent dependence of the T_e profile on the $\bar{n}_{e0}$, both n_e and D_α emission profiles are less sensitive to variations of $\bar{n}_{e0}$. This result suggests that their dependence is rather strong than the

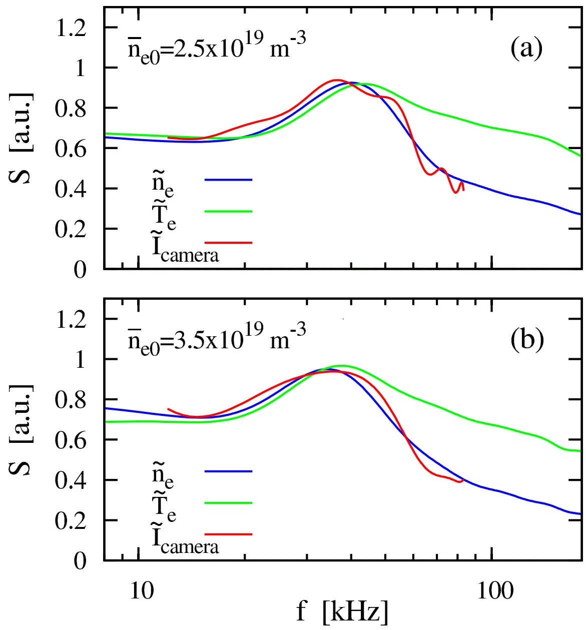

Figure 3.10: Comparison of the frequency spectra of $\tilde{n}_e$ (blue) , $\tilde{T}_e$ (green) and $\tilde{I}_{camera}$ (red). Each result is an average of six spectra corresponding to different shots with the same line-averaged density. Figures (a) and (b) correspond to series of shots with $\bar{n}_{e0} = 2.5 \times 10^{19}\ m^{-3}$ and $\bar{n}_{e0} = 3.5 \times 10^{19}\ m^{-3}$ respectively.

dependence of the I_{camera} on T_e. It provides support in favour of the principle that the GPI is a diagnostic that measures density rather than temperature events. However, the accurate interpretation of the results in terms of plasma parameters requires more systematic comparison between emission intensity, n_e and T_e, which has never been done by us. Therefore, the experimental results in this work will be presented and analysed in terms of the D_α light emission itself without attempting to unfold the density or temperature fluctuations.

In addition, as seen in Fig. 3.9(c), the I_{camera} is higher in high density shots.

Based on results of figure 3.8 and figure 3.9, we can conclude that high density shots are preferential for the operation of the GPI system. On the one hand plasma parameters are less sensitive to the gas puff, on the other hand the fluctuation magnitude is higher, which is favourable for the signal to noise ratio of the GPI diagnostic. Meanwhile, in ohmic plasmas high density shots have higher turbulence magnitudes (before detachment or density limit). This is favourable as far as we are interested in the fluctuating part of the signal.

The fluctuation properties of the GPI signal depend on both density and temperature fluctuations. In order to gain deeper insight into this issue, we performed additional studies. Figure 3.10 shows the comparison of powers spectra of $\tilde{n}_e$, $\tilde{T}_e$ and $\tilde{I}_{camera}$, measured at r=45.5 cm for two sets of shots (corresponding to $\bar{n}_{e0} = 2.5 \times 10^{19}\ m^{-3}$ (a) and $\bar{n}_{e0} = 3.5 \times 10^{19}\ m^{-3}$ (b)). The power spectra of $\tilde{T}_e$ and $\tilde{n}_e$ were measured by triple Langmuir probes. In the figure, each curve is an average of spectra over 6 shots under the same discharge conditions. Because in the performed experiment the Langmuir probe and the GPI system have different sampling time (2 and 6 μs respectively), the corresponding Nyquist frequencies are also different (250 and 83.3 kHz, respectively). Therefore, the frequency range of the GPI signal in Figure 3.10 is shorter than that of the Langmuir probe. Meanwhile, the frequency spectrum of the fast camera signal contains a parasitic low frequency noise which has most of its energy in the range below 10 kHz. Therefore, the frequency spectrum of the GPI signal fluctuations in the figure 3.10 starts from 10 kHz. Thus, the comparison betwen the GPI fluctuation spectrum and the Langmuir probe spectrum can only be made in the frequency range between 10 and 83 kHz. The remarkable similarity between the $\tilde{I}_{camera}$ spectrum and $\tilde{n}_e$ spectrum indicates that the $\tilde{I}_{camera}$ is more sensitive to $\tilde{n}_e$ than to $\tilde{T}_e$. It is noted that this phenomenon remains the same regardless the plasma density $\bar{n}_{e0}$ in figure (a) and (b), even though the positions of peaks in two figures are slightly different.

3.3 Typical turbulent structures from the GPI system at TEXTOR

Figure 3.11 shows a series of frames taken during an ohmic deuterium discharge with $\bar{n}_{e0} = 3.0 \times 10^{19}\ m^{-3}$, I_p=300 kA, B_T=2.6 T and with an exposure time of 6 μs. The images have been processed to remove noise sparks from frames. Each frame of GPI data was filtered with the 2D low-pass filter (with the convolution kernel [3 x 3]) to partially suppress the pixel noise and hold main turbulent events.

Previous authors [44,59] have presented their GPI results in terms of the absolute intensity value (scaled from 0 to some positive value). In our case, as we are interested only in turbulent behaviors, we subtract the time-averaged mean values from the light intensity detected at each pixel for every image. In this way we leave the fluctuating part of the signal only.

The radial distribution of the emission intensity exhibits a significant radial inhomogeneity as seen in figures 3.6 and 3.11. For some applications, it might be necessary to highlight far SOL and edge regions and, therefore, compensate such an inhomogeneity. It has not been performed in Fig. 3.11 as we prefer to draw readers' eyes directly to the important dynamics of the central structure. However, details of this technique will be discussed later in this section.

The red colour structures in figure 3.11 represent edge turbulent structures. The typical radial and poloidal dimension of structures is ~ 2 cm and 6 cm, re-

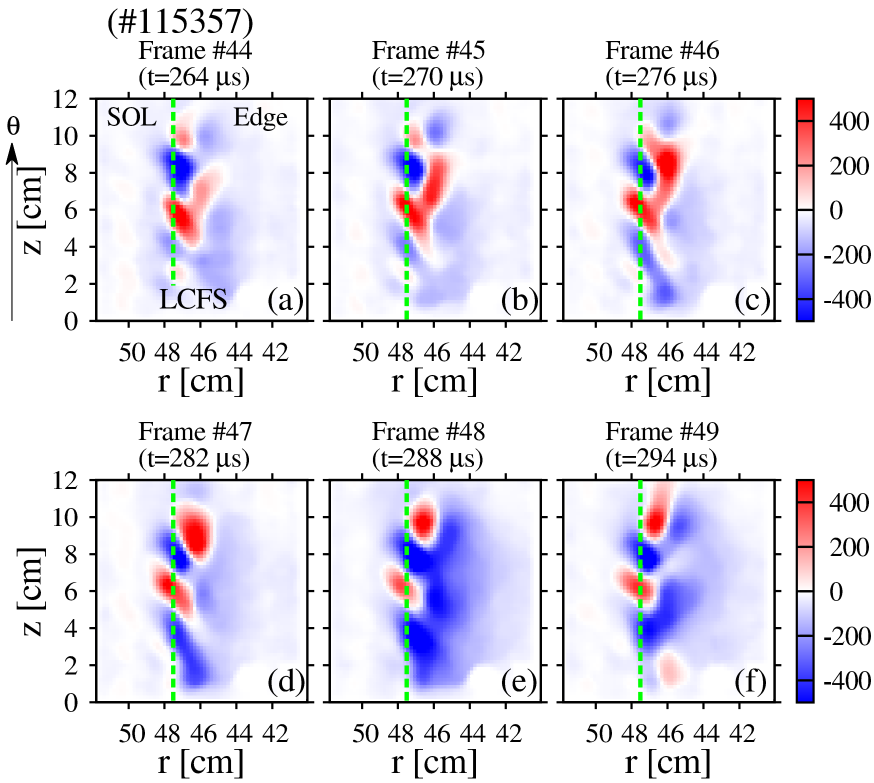

Figure 3.11: A set of GPI images taken with an exposure time of 6 μs during a typical ohmic discharge at TEXTOR (I_p=300 kA, $\bar{n}_{e0} = 3 \times 10^{19}\ m^{-3}$, B_T=2.6 T). The measurements have been performed in the deuterium D_α line. The radial (TEXTOR minor radius) and vertical (poloidal) scales are indicated in the first frame. The green dashed line indicates the position of the separatrix. The radial outward direction is towards the left.

spectively. The typical moving speed of turbulent eddies in the plasma edge is about 0.3-0.5 km/s along the radial and 1-3 km/s along the poloidal directions. In the poloidal direction, the eddy moves downward in the SOL (along the ion diamagnetic drift direction) and upward in the plasma edge (along the electron diamagnetic drift direction), following up mainly with the $E_r \times B$ drift (will be discussed in chapter 5). One can clearly see in Figs. 3.11(d)-(f) that the turbulent eddy in the plasma edge moves poloidally upward at a speed of $V_\theta \approx 1.1\ km/s$.

It is interesting to note that in all of our measurements the decay of turbulent structures appears to be very fast once they move out across the LCFS position. They decay so fast that it is difficult to observe turbulent behavior further than

2-3 cm outside the LCFS. This result is different from what has been observed in NSTX and C-Mod, where long-lasting structures propagate far outside the separatrix. This difference can be partially explained by shorter connection length of the magnetic field line to the TEXTOR toroidal (or even poloidal) limiter and consequently more effective dissipation of turbulent structures due to fast parallel particle flux. Furthermore, because of some features of limiter tokamaks, the SOL plasma of TEXTOR usually has temperatures lower than that of diverter machines like NSTX and C-Mod, which results in a lower emission intensity in this region.

✠ ***Radial inhomogeneity of the emission intensity***

It has been discussed already in section 3.2 that the radial distribution of the emission intensity exhibits a significant radial inhomogeneity. This is seen also in figures 3.6(a) and (b). This feature is also reflected in the fluctuating part of the GPI images in Fig. 3.11. We already discussed before that this inhomogeneity comes from the opposite radial dependency of the electron density $n_e(r)$ and the density of a neutral particles in the beam $n_0(r)$ included in the expression for $\epsilon(r)$ in Eq. (3.6). For some practical applications (such as the optical flow approaches), it might be necessary to highlight far SOL and edge regions and, therefore, compensate such an inhomogeneity. This compensation becomes especially important if one needs to emphasize studies on the SOL region. ~~To make this compensation, one can divide the instant value of the fluctuations at each pixel either by the root mean square (RMS) value of fluctuations~~ $\cancel{\tilde{I}^{RMS}_{camera}}$ ~~or by mean time-averaged value of~~ $\cancel{I_{camera}}$ ~~at that pixel.~~ In the following excerpt we will make some attempts to deal with this problem.

Figures 3.12(a)-(c) show the set of a GPI frames with obviously uneven radial distribution of fluctuation magnitudes. Namely, structures in the central region ($r = 46 - 48\ cm$) are much more visible whereas structures in the far SOL ($r = 50 - 52\ cm$) are hardly observed. ~~One can clearly see that the dynamics of far SOL and edge regions is not clear.~~ In the end of our "corrections" one would like to see the set of GPI frames where the level of the fluctuations does not exhibit radial variations, i.e., far SOL, edge and central regions are equally accesible for the analysis. We then propose to normalize by dividing each instant value of fluctuations measured at each pixel by the quantity that characterize the time-averaged magnitude of fluctuations at that pixel. For instance, one can divide by the root mean square (RMS) value of fluctuations. The GPI frames processed in this way are shown in Figs. 3.12(d)-(f). Comparing Figs. 3.12(a)-(c) and Figs. 3.12(d)-(f), it is visible that our correction highlights far SOL and edge regions, where the natural emission intensity is low. Having done this, new SOL and edge physics might get out. For instance, some regular poloidally extended wave-like structures with the typical poloidal wave legths of $\approx 2\ cm$ can be observed in the far SOL. These

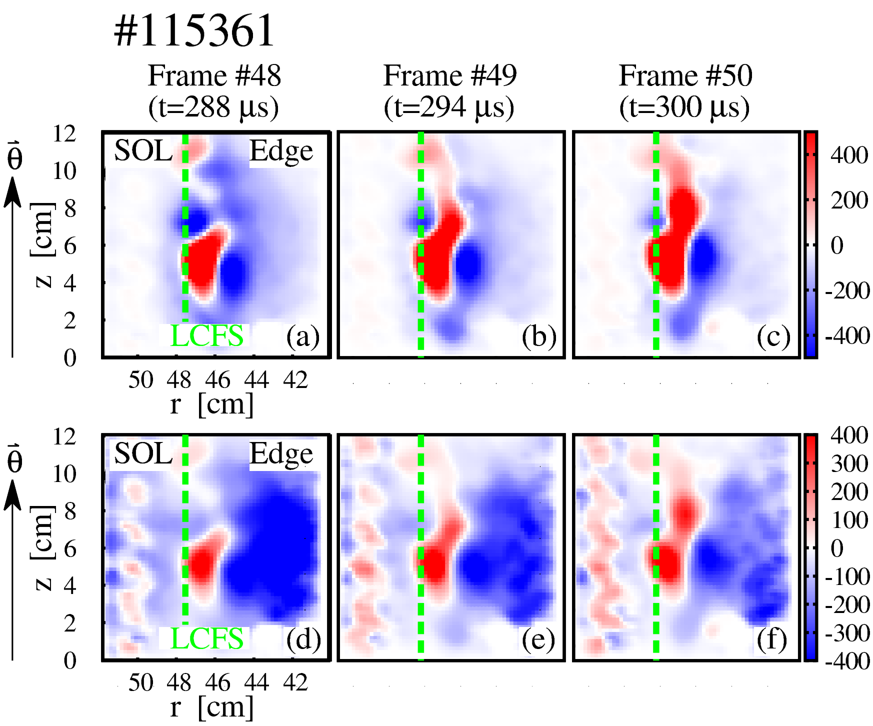

Figure 3.12: (a)-(c): The typical set of GPI frames. The only central region around LCFS is visible. (d)-(f): The set of GPI frames where the level of fluctuations does not exhibit radial inhomogeneity. This is achieved by dividing the instant value of the fluctuations at each pixel by the root mean square (RMS) value of fluctuations at that pixel.

structures are visible in every GPI frame and in every TEXTOR discharge.

We have never seen such kind of regular structures on the right hand side of GPI frames (at the far edge region). In addition, these wave-like structures are not artefacts coming for instance from the camera performance because they are not observed without plasma. This is confirmed by an imaging of the fixed object illuminated by an external light source (halogen lamp). The real physical nature of those structures has not yet been systematically studied although this phenomena might be scientifically interesting.

3.4 Langmuir probes

One of the most popular diagnostics for studies of plasma parameters is the Langmuir probe. This technique was developed by american physicist Irving Langmuir, who used this technique to determine plasma parameters. The basic idea is to insert one or more metallic electrodes into a plasma and apply a constant or time-varying electric potential between the various electrodes or between them and the vessel. The currents passing through the electrodes and their potentials allow to determine the physical properties of the plasma. One of the unique features of this diagnostic is that it can simultaneously measure local plasma density, potential and electron temperature, thereby providing an almost complete set of plasma parameters.

The most simple probe configurations is called a “single probe”, which consists of one electrode biased with a voltage (or voltage ramp) relative to the vessel. The volt-ampere characteristic of a single probe is shown in Fig. 3.13, from which one can distinguish three regions. If the potential applied to the probe is sufficiently negative, all electrons are repelled and only ions contribute to the current drawn by the probe. At relatively high negative bias voltage all ions in the vicinity of the probe are collected and the ion-current saturates (region A in Fig. 3.13).

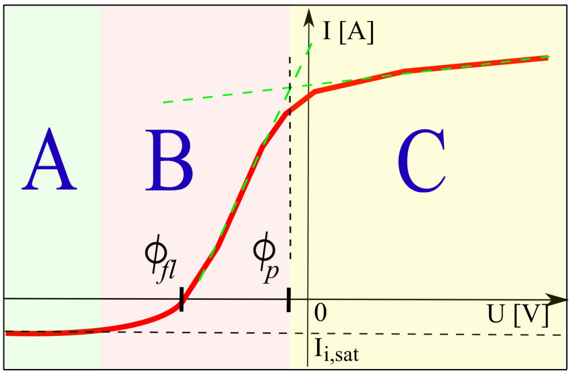

Figure 3.13: The volt-ampere characteristic of a single probe.

Increasing the bias, more and more electrons have sufficient kinetic energy to reach the probe. The contribution of the electrons to the current passing through the electrode increases exponentially until the electrode potential equals to the plasma potential ϕ_p (region B in Fig. 3.13). Ambipolarity requires that in the absence of the potential applied to the probe the electric current to the probe is zero, i.e., the probe is floating. The higher mobility of the electrons (in comparison with the mobility of ions) causes the probe to become charged more negatively with respect to the plasma potential (probe is charged to the so called floating potential ϕ_{fl}).

The third region (region C) starts at the plasma potential. In this region, even suprathermal electrons propagating outward from the probe reach the probe surface. In the ideal case of a planar probe of infinite size, all electrons in the vicinity of the probe surface are collected and the electron current saturates. In reality, mostly cylindrical probes or sometimes spherical probes are used. They can be regarded as planar only if the Debye shielding length $\lambda_D = \sqrt{\epsilon_0 k_B T_e / n_e e^2}$ (where ϵ_0 is the permittivity of free space, k_B is the Boltzmann constant, n_e is the electron density, e is the elementary charge) is much smaller than typical probe dimensions. In the opposite case, the probe current grows slowly with increasing the probe potential due to an enlargement of the collection area of the probe.

Under conditions when plasma parameters are not so severe to damage probe collectors, this diagnostic seems to be the most effective in terms of measurement capabilities and operating costs. In fact, this diagnostic is suitable for studies of edge plasma parameters in most medium size tokamaks.

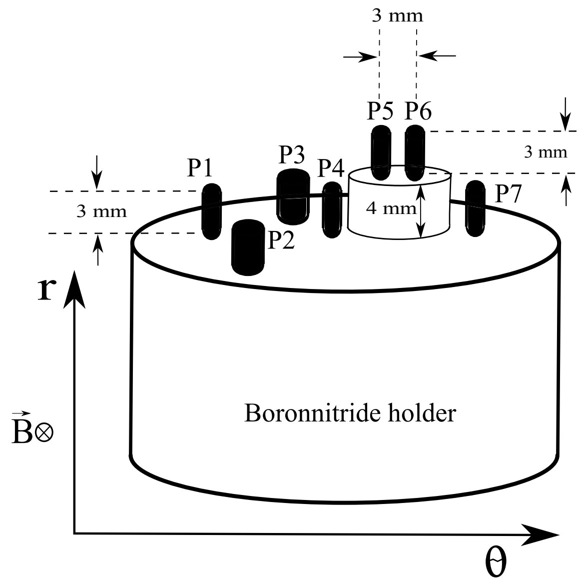

Figure 3.14: Schematic drawing of the fast reciprocating Langmuir probes. Multi-array probe pins mounted on a boronnitride (BN) holder. Coordinates r and θ denote the radial and poloidal directions whereas B is in the toroidal direction.

The TEXTOR tokamak is equipped with the fast reciprocating Langmuir probe system, mounted at the outer midplane (toroidally 40° away from the GPI system). For years, this Langmuir probe system has been used for a wide range of experiments and studies. For instance, this was a main diagnostic tool for turbulence studies in Refs. 36, 58, 60, 61. Within the frame of this work, this system has been used as a complementary diagnostic, in addition to GPI system, to measure the equilibrium and fluctuating plasma parameters. This probe system is installed in the outer equatorial plane of the TEXTOR tokamak. This probe can provide radial profiles of density, electron temperature, floating potential and electric field in the plasma edge with high spatial resolution. The head of the probe consists of seven molybdenum pins mounted on a boronnitride holder. Schematic drawing of the

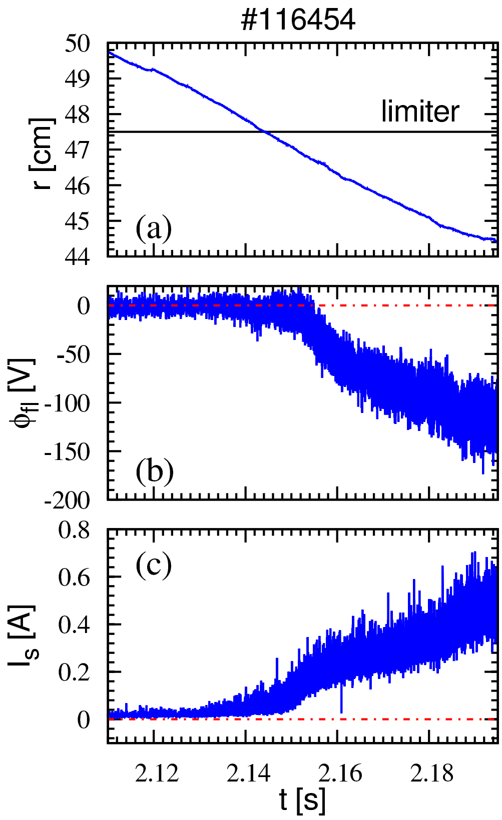

Figure 3.15: (a): The time trace of the fast probe radial position measured during the forward plunge. The black solid line indicates the radial position of the limiter. (b)-(c): The corresponding time traces of ϕ_{fl} and I_s.

probe is shown in Fig. 3.14. All probe pins are 3 mm long with a diameter of 2 mm for P2 and P3 and of 1 mm for the others. All pins are located so that to avoid the shadowing effect between them along magnetic field lines. Among these seven pins, four (P1−P4) are set up as a triple probe [62, 63]. To that end, pins P1 and P4 are used to detect the floating potential, ϕ_{fl1} and ϕ_{fl4}, whereas P2 and P3 are biased to measure the ion saturation current (I_{sat}). The remaining three pins, P5−P7, measure the floating potential signals, ϕ_{fl5} , ϕ_{fl6} and ϕ_{fl7}.

All signals are digitized at a sampling rate of 500 kHz (the corresponding Nyquist frequency $f_{Ny} = 250\ kHz$) to provide simultaneous measurements of both the time-averaged and fluctuating quantities. With such configurations, the local equilibrium electron temperature T_e, density n_e and the plasma potential ϕ_p can be determined by the triple probe. The radial electric field E_r is derived from the radial derivative of the plasma potential $\phi_p = \phi_{fl} + 2.8T_e$.

For better clarity, the raw signals of the probe are depicted in Fig. 3.15 for the discharge #116454. Figure 3.15(a) shows the time trace of the fast probe radial position measured during the forward plunge, where one can see that the probe moves from the SOL into the edge up to the radial position of $r = 44.5\ cm$. The black solid line in this figure indicates the radial position of the limiter. The corresponding time traces of ϕ_{fl} and I_s are shown in Figs. 3.15(b) and (c), respectively.

3.5 Summary and future directions

Within the frame of this PhD project, the GPI diagnostic, assigned to measure 2D effects of the plasma turbulence, has been developed for the TEXTOR tokamak. The main points presented in the course of this chapter are the following:

- The main technical novelty of this system, with respect to previous GPI systems in C-Mod and NSTX, is the novel design of the in-vessel GPI optical telescope which can sustain severe thermal load and coating. The presented design, with some small modifications, might well be used as a basis for the GPI systems on next generation machines.
- The results of this chapter suggest that the local gas puff with the flux $(6-8) \times 10^{19}$ molec/s, typical for the GPI experiment on TEXTOR, does not influence substantially on local and global plasma performance neither on plasma turbulence properties.
- We have shown that the equilibrium/fluctuating emission intensity is more sensitive to the equilibrium/fluctuating electron density than the equilibrium/fluctuating electron temperature, supporting the idea that the GPI is the diagnostic that measures primarily density events.
- The two-dimensional structure and dynamics of turbulence in the edge of TEXTOR have been observed for the first time.
- We have shown that the dynamics of turbulence in the SOL of divertor and limiter tokamaks are very different. The decay of structures in the SOL of limiter tokamaks is much faster due to probably shorter connection length of the magnetic field line to the toroidal (or even poloidal) limiter.

The GPI diagnostic is the rapidly developing technique for the study of plasma turbulence. Therefore, in that context, one would like to discuss about some trends in the development of this technique.

A significant drawback of this system is a very limited radial range (approximately 6-8 cm in the vicinity of LCFS) where the emission intensity is localized. On the other hand, several technical approaches aimed to extend this radial range are widely used in imaging techniques. For instance movable reciprocating gas puff system is implemented in the beam emission spectroscopy on thermal helium at TEXTOR [64]. Alternatively, the supersonic gas puff system is used in the supersonic helium beam diagnostic at TEXTOR [65]. The development of the GPI gas puff in these directions is seen worthwhile.

The interpretation of an emission intensity in terms of n_e and T_e is another challenging diagnostic issue which should be studied thoroughly in the context of a development of the GPI technique. One possible approach to simplify this interpretation is to use the *helium line intensity ratio technique* [66], which is a common method used to determine the electron temperature and density in the boundary region of magnetic fusion devices. This, however, requires the use of a helium gas puff instead of deuterium one. The basic idea is that emission lines from two singlet state transitions (at $667.8\ nm$ and $728.1\ nm$) and one triplet state transition (at $706.5\ nm$) of neutral helium is sufficient to accurately determine the local electron temperature and density. In particular, the ratio of the $667.8\ nm$ to $728.1\ nm$ gives the electron density and the ratio of the $728.1\ nm$ to $706.5\ nm$ gives the electron temperature. This effort requires the development of an atomic physics modelling such as DEGAS 2 to accurately describe the physics processes of the helium cloud interacting with plasma. Meanwhile, it requires much more complex imaging system (optics and cameras) where the resulting image is splitted into 3 equivalent images so that one can make simultaneous observations in different spectral lines.

The inherent feature of the GPI diagnostic is that GPI observations are essentially two-dimensional. This feature is based on the assumption that turbulent structures are believed to have a parallel wavelength $k_{\parallel}$ much longer than the perpendicular wavelength $k_{\perp}$. However, it is not clear whether the turbulent structure is completely homogeneous along the magnetic field so that $k_{\parallel} = 0$ or whether some finite scales may be involved. The measurement of the tree-dimensional turbulence geometry is the another subject of the development of the GPI technique which is receiving much attention today [32, 47]. For this purpose, the GPI measurements of plasma turbulence are made simultaneously at two different poloidal and toroidal locations and these two GPI views are designed so as to view the same magnetic field line [32].

4

The derivation of the velocity vector field

The experimental reconstruction of the velocity vector field is one of the common data processing tools applied to GPI data. This approach can substantially improve our understanding of plasma turbulence and its link to the turbulent particle flux. In particular, the reconstruction of the time-resolved velocity vector field can disclose a phase shift between the density and velocity fluctuations, which is necessary for the estimation of the turbulent flux. In addition, information about the time-resolved velocity vector field can disclose an interplay between the vorticity $\vec{\Omega} = (\vec{\nabla} \times \vec{v})$ and the plasma density and, in this way, deepen our insight into the turbulence physics. In recent times, there has been rising interest in deriving velocity vector fields from spatially and temporally resolved density fluctuation data obtained either with BES or GPI diagnostics [13–15]. One just has to emphasize the recent work where the two-dimensional spatial time-correlations have been applied to the gas puff imaging data collected at the edge of EAST tokamak plasmas [15]. Of particular relevance is the hybrid technique, combining optical flow [16] and local pattern matching techniques, which has been implemented and tested on GPI data from the National Spherical Torus Experiment (NSTX) machine [14].

This chapter considers the reconstruction of the velocity vector field using data from GPI diagnostic at TEXTOR. We start from the basic principles of the optical flow methods in Sec. 4.1. The simple and perhaps most popular algorithm, which is based on the traditional Horn and Schunck method, is reviewed in Sec. 4.2.

Some challenges faced by experimentalists in the reconstruction of velocity vector fields from GPI data are addressed in section 4.3. The multiresolution optical flow scheme, which has been used for the processing of GPI data in this work, is discussed in section 4.4. The characterisation of zonal flows based on optical flow analysis of GPI data is addressed in section 4.5. As a matter of further development of our algorithm, an alternative approach based on the two-dimensional cross-correlation is addressed in section 4.6. The summary and ideas for the future development of the optical flow technique are presented in section 4.7.

4.1 Optical flow methods

The optical flow estimation algorithms, developed for machine vision and weather tracking, are the most popular methods of reconstructing of the velocity vector maps. Therefore, they are considered to be one of the primary research areas in image and video processing techniques [67, 68]. Their distinctive feature is extremely high spatial resolution (of the order of a few pixels in a raster image) which allows for relatively accurate tracking of the individual turbulent structures. A detailed review of the optical flow technique can be found in the following reviews: [69, 70].

The goal of the technique is to calculate the optical flow vector

$$\vec{\mathbf{v}} = (u(x, y, t), v(x, y, t)), \tag{4.1}$$

between two successive images of an image sequence, where (x, y, t) is a point in the spatio-temporal domain with t denoting the time axis. In order to estimate this flow vector, it is necessary to introduce the "intensity constancy assumption", i.e., that the intensity structures of local time-varying regions within the image are approximately constant over several GPI image frames. This is the starting point for all optical flow approaches. Assuming that the intensity of a structure remains unchanged between the pixel (x, y) in the image at time t and the shifted pixel $(x + u\delta t, y + v\delta t)$ in a successive image at time $t + \delta t$ yields the constraint

$$I(x, y, t) = I(x + u\delta t, y + v\delta t, t + \delta t), \tag{4.2}$$

where I denotes the local intensity value and δt is the sampling time. Note that this is a nonlinear equation with respect to u and v.

In order to simplify our work with this equation and resolve it for u and v, it is usually linearized by a first order Taylor expansion. This leads to the linearized intensity constancy assumption:

$$\frac{\partial I}{\partial t} + u\frac{\partial I}{\partial x} + v\frac{\partial I}{\partial y} = \frac{\partial I}{\partial t} + \vec{\mathbf{v}} \cdot \vec{\nabla} I = 0. \tag{4.3}$$

It must be noted that the linearization is only valid under the assumption that the image object changes linearly along the displacement, which, in genaral, is not the case, especially for large displacements.

One can reformulate equation (4.3) in terms of a substantial derivative

$$\frac{dI}{dt} = 0. \tag{4.4}$$

Equation (4.4) is known as the ***optical flow constraint*** [69, 70] equation.

The optical flow algorithms are subject to some limitations which require us to interpret the results with caution. The next section provides the detailed discussion on this topic.

4.1.1 Limitations of the optical flow approach

Following are some of the common requirements which should be fulfilled in order for the optical flow results to be exactly the image motion.

(a) The assumption (already mentioned in the previous section) that the image object intensity changes linearly along the displacement.

(b) The optical flow constraint stated in equation (4.4). This constraint is equivalent to the requirement that the divergence of the velocity field sought is zero $\vec{\nabla} \cdot \vec{\mathbf{v}} = 0$. It comes from the fact that equation (4.4) is simply the continuity equation written for the intensity signal I

$$\frac{\partial I}{\partial t} + \vec{\nabla} \cdot (\vec{\mathbf{v}} I) = 0, \tag{4.5}$$

provided that the flow is divergence-free flow. Therefore, a statement equivalent to the optical flow constraint is that the divergence of the velocity field is zero.

(c) From equation (4.4), it is easy to see that one intensity constancy assumption only is not enough to determine all components of the velocity vector v. Based only on Eq. (4.4), one can merely reconstruct so-called "normal components" of velocity, which are in the direction of the image intensity gradient ∇I. For instance, the rotational motion when structures move primarily perpendicular to the intensity gradient could not be observed using optical flow methods. This is commonly known as the "aperture problem". It presents a critical limitation on the determination of plasma velocity from the optical flow approach and must be taken into account when interpreting the velocity results obtained using this approach. In that sense, the problem of the reconstruction of the vector field on the basis of equation (4.4) only is *ill-posed*. That is to say, this problem should be considered as a *regularization problem* (see Sec. 4.2 for more details about regularization).

(d) An important technical limitation of this approach is that data must be sufficiently resolved in the time domain in order to uniquely track the structures in the series of consecutive images. In other words, for large displacements, the algorithm can interpret the translation of a structure as simply disappearance in the first frame and sudden appearance in the second, rather than the travelling from one location to the other. This implies another constraint

$$|\mathbf{v}|\ \delta t \ll l_c, \tag{4.6}$$

where l_c is the typical spatial scale of the structures and δt is the sampling time of the imaging. In other words, the frame-to-frame displacement of structures should be less than the size of a structure. However, this condition is improved linearly with an increase in the frame rate of the camera.

Realistically, these requirements are never completely satisfied within the image frame. The degree to which these conditions are fulfilled partially defines the accuracy of the optical flow analysis. Consequently, further steps that are capable of minimizing at least some of these constraints are required.

4.2 Standard Horn and Schunck formulation of optical flow

The aperture problem has historically been confronted using a variety of techniques and one common approach is to perform the *Tikhonov regularization* [71] of Eq. (4.4). *Regularization* refers to a process of introducing an additional information (additional term) in order to solve an ill-posed problem. Tikhonov regularization is the most commonly used method of the regularization, in which the regularization term enforces the smoothness of the vector field sought. Put simply, the regularization term simply smoothes the velocity vector field in each pixel over neighboring pixels, improving the conditioning of the problem. Indeed, it is reasonable to enforce smoothness of the flow as the underlying vector field is believed to be mostly continuous. It would be very suspicious if every point of the image moved completely independently. One of the most simple and traditional optical flow estimations using the Tikhonov regularization has been proposed by Horn and Schunck [70]. **This approach, although with some modifications (multiresolution strategy) discussed in Sec. 4.4, will be used in this thesis to analyse the velocity vectors of GPI image sequences.** Therefore, in this section, we would like to discuss this approach more deeply.

For better readability, the following notations will be used in this section from now onwards:

$$
\begin{aligned}
I_t &= \frac{\partial I}{\partial t} \\
I_x &= \frac{\partial I}{\partial x} \\
I_y &= \frac{\partial I}{\partial y} \\
u_x &= \frac{\partial u}{\partial x} \\
u_y &= \frac{\partial u}{\partial y} \\
v_x &= \frac{\partial v}{\partial x} \\
v_y &= \frac{\partial v}{\partial y}
\end{aligned}
$$

The algorithm implies the minimization of the following energy functional:

$$E(u,v) = \int_{\Omega} (\underbrace{(I_x u + I_y v + I_t)^2}_{\text{Data term}} + \underbrace{\alpha(|\nabla u|^2 + |\nabla v|^2)}_{\text{Smooth term}})dxdy. \tag{4.7}$$

That is the common concept of *calculus of variations*. In a variational approach one formulates some model assumptions L in terms of an energy functional

$$E(u(x,y), v(x,y)) = \int_{\Omega} (L(u(x,y), v(x,y)))dxdy \tag{4.8}$$

and tries to find those functions u, v that minimize the energy $E(u,v)$. We know that the maxima and minima of a given function may be located by finding the points where its derivative vanishes. By analogy, solutions of a smooth variational problem such as in Eq. (4.7) may be obtained by finding a function where the functional derivatives are equal to zero. The minimisation of $E(u,v)$ is to be accomplished by solving the associated Euler-Lagrange equations:

$$
\begin{aligned}
\frac{\partial L}{\partial u} - \frac{\partial}{\partial x}\frac{\partial L}{\partial u_x} - \frac{\partial}{\partial y}\frac{\partial L}{\partial u_y} &= 0 \\
\frac{\partial L}{\partial v} - \frac{\partial}{\partial x}\frac{\partial L}{\partial v_x} - \frac{\partial}{\partial y}\frac{\partial L}{\partial v_y} &= 0.
\end{aligned} \tag{4.9}
$$

In our particular case, the function $L(u,v)$ is the integrand in Eq. (4.7):

$$L(u(x,y), v(x,y)) = (I_x u + I_y v + I_t)^2 + \alpha(|\nabla u|^2 + |\nabla v|^2). \tag{4.10}$$

Therefore, the corresponding Euler-Lagrange equations can be rewritten in the following manner:

$$
\begin{aligned}
(I_t + uI_x + vI_y)I_x - \alpha\Delta u &= 0 \\
(I_t + uI_x + vI_y)I_y - \alpha\Delta v &= 0.
\end{aligned} \tag{4.11}
$$

Discretization of these equations leads to a linear system of equations, where for each pixel i in the frame there are two rows in the system matrix (one for u_i and one for v_i). The following iterative scheme is proposed in Ref. 70:

$$\begin{aligned} u^{k+1} &= \bar{u}^k - \frac{I_x(I_x\bar{u}^k + I_y\bar{v}^k + I_t)}{\alpha^2 + I_x^2 + I_y^2} \\ v^{k+1} &= \bar{v}^k - \frac{I_x(I_x\bar{u}^k + I_y\bar{v}^k + I_t)}{\alpha^2 + I_x^2 + I_y^2}, \end{aligned} \tag{4.12}$$

where $k+1$ denotes the next iteration step, and k is the last calculated result. $\bar{u}$ and $\bar{v}$ denote the local average of these quantities over neighboring pixels. We omit the details of the numerics and refer the reader to the more detailed discussion in Ref. 70.

It should be noted that the regularisation of the optical flow approach with the regularization term which respects the smoothness has one important shortcoming: the smoothness term in Eq. (4.7) is additive with respect to the data term, i.e., it does not depend on the intensity I. Therefore, the smoothness term does not act equally well on all structures within one frame. Let's assume that all structures move with the same u and v. The data term in Eq. (4.7) includes intensity and its gradients, and, because the intensities of particular structures may vary significantly from one structure to another, the data term will also follow these variations. However, the smoothness term remains robust independently of the magnitude of the data term because α is just a constant for all pixels in the frame. Actually, the parameter α should be adjusted to some "typical" size and magnitude of structures. However, the fully developed turbulence implies a simultaneous coexistence of many eddies in a wide range of scales and magnitudes. Therefore, the outliers in the analysis of real GPI data are inevitable. This is the main drawback of the majority of optical flow approaches and must be tackled in a way when smoothness term respects the emission intensity value. However, the implementation of this idea is outside the scope of this thesis.

4.3 Some challenges faced by experimentalists in the reconstruction of velocity vector fields

This section is aimed to demonstrate some challenges faced by experimentalists in the reconstruction of velocity vector fields from GPI data. To that end, the original Horn and Schunck approach has been implemented and applied to artificial test images imitating some examples of a real turbulent motion. They include synthetic sequences with both translational and divergent motions (we refer to divergent motion as to a growth or decay of structures, which is equivalent to the violation of the optical flow constraint) as well as the application of the approach to large frame-to-frame displacements. Let's discuss them one by one.

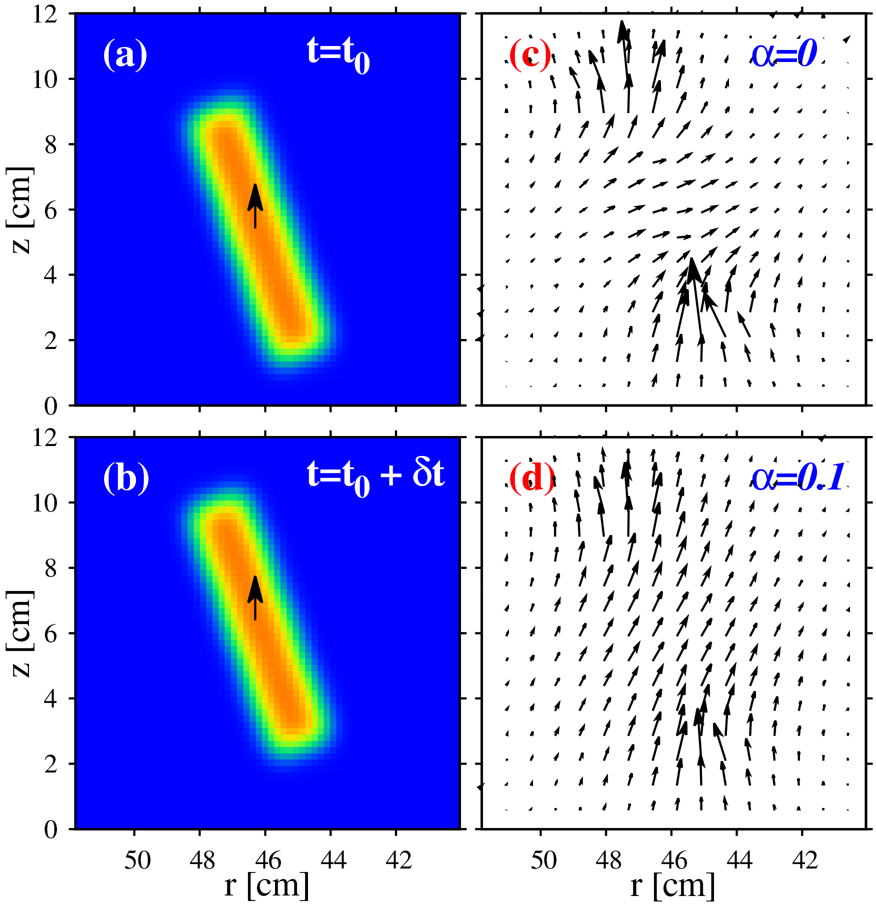

Figure 4.1: (a)-(b): Intensity map from an artificial test data set imitating the poloidal propagation of the poloidally stretched turbulent structure. (c)-(d): The velocity vector map obtained with the Horn and Schunck approach for two different smoothing parameters α.

One of the most practical test sequences, relevant to our GPI studies and imitating the propagation of a poloidally stretched turbulent structure, is shown in Fig. 4.1. The main issue in this case is that equation (4.4) naturally tends to estimate the motion predominantly along ∇I, as we have already mentioned before. Figures 4.1(a) and (b) show the poloidally elongated structure ~~displacing~~ displaced linearly upward from Fig. 4.1(a) to Fig. 4.1(b), almost along the direction of the elongation. Such shape of structure is very typical for plasma turbulence, especially in weakly sheared flow regimes when the splitting process does not occur.

In Fig. 4.1(c), we applied the Horn-Schunck regularisation when the smoothness term is minimised (i.e. only equation (4.4) is included or $\alpha = 0$). One can clearly see that the motion estimation in the main body of the structures (in the middle) is suspicious because it shows the velocity vectors pointing to the right (along ∇I), whereas the whole structure actually moves upward. Only velocity vectors in the bottom and top of the structure suggest a more or less reasonable direction, although their lengths are sometimes overestimated. These outliers come most likely from the above stated rough assumption that the intensity of structure changes linearly along the displacement.

Results of the Horn-Schunck approach with the introduction of the regularisation term (smoothing parameter $\alpha = 0.1$) are shown in Fig. 4.1(d). One can clearly see the obvious improvement of the performance. The vectors become more unidirectional with more or less equal lengths because the flow information missing in inner parts of homogeneous objects is filled in from the motion of boundaries. However, the resulting field is more blurred due to smoothing. Higher values of the parameter α lead to stronger smoothing and therefore velocity values in the inner part of a structure can be understated. In practice, the parameter α is selected emphyrically to achieve a reasonable smoothness in the flow over the whole image.

The results of this paragraph show that the derivation of the poloidal displacement of poloidally stretched turbulent structures is the subject to some obstacles imposed by optical flow constraints. Special emphasis should be put on the centre of a structure, where the change in ∇I is marginal and optical flow tends to underestimate the absolute value of the velocity. The smoothing of the vector field partially corrects it at the expense of some degradation in spatial details of the vector field sought.

Another test sequence, highly relevant to the real behavior of turbulent structures is the divergent motion shown in Figs. 4.2(a)-(b). This motion is related to a fast growth or decay of a structure between two consecutive frames (this is related to the deviation from the optical flow constraint $\frac{dI}{dt} \neq 0$). The typical life-time of structures, as estimated from the tracing of individual structures through the sequence of the GPI frames, is around several tens of μs. Therefore, with typical sampling time of 2 μs there should not be significant alteration of the intensity corresponding to a certain structure. Nevertheless, there is always some minority of structures with drastically short life-time of few μs. One needs to understand that the life-time of turbulence is also the same multiscale quantity as magnitude and size of structures and should be considered only statistically. Anyway, such short-lived structures exist and to a certain degree limit the performance of the optical flow approach.

The optical flow, corresponding to the intensity weakening in two consecutive frames is shown in Fig. 4.2(c). The smoothing parameter in this example can not be

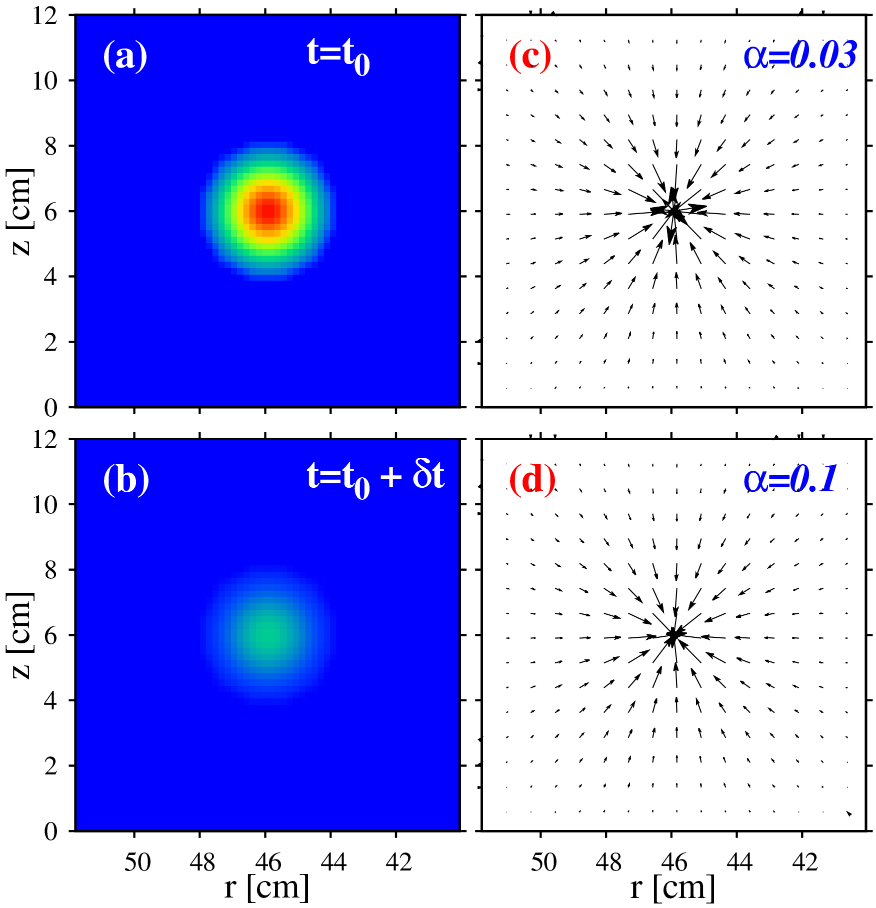

Figure 4.2: (a)-(b): The artificial test data set imitating the divergent motion of turbulent structures. (c)-(d): The corresponding velocity vector map obtained with the optical flow approach based on the Horn and Schunck algorithm for two different smoothing parameters α.

equal to zero, because it would lead to big outliers in results. Therefore, the small smoothing parameter $\alpha = 0.03$ has been chosen for this case. Obviously, even though the structure stays quietly without any "real" displacement, the approach shows some inward convergent motion following the change in ∇I. It should be noted that one can not remove this obstacle simply enhancing the smoothness of the vector field as we can see in Fig. 4.2(d), where the higher parameter $\alpha = 0.1$ has been chosen. Moreover, it is not possible to overcome this problem staying merely within the frame of the gradient-based methods, such as all optical flow methods.

The divergent/convergent motion of turbulent structures, associated with their fast growth or decay, is the challenging problem for the correct reconstruction of the velocity field from GPI data. Fortunately, the divergence is the quantifiable characteristic and might be taken into account when we interpret the results of the optical flow methods. For instance, the regions of high divergence could be simply excluded from the analysis.

The impact of the divergent/convergent events on the detection of displacements may be represented in a simple mathematical way. Let's denote δI as the change in the intensity of some structure between two consecutive images caused by the divergence/convergence. Meanwhile, the expression $\lambda \cdot \nabla I$ denotes the change in the intensity at some pixel due to linear displacement along ∇I, where λ denotes the linear frame-to-frame displacement of structure within the image plane. Then, the divergence is negligible in the motion analysis if the following condition holds:

$$\delta I \ll \lambda \cdot |\nabla I|. \tag{4.13}$$

Note that the sampling time is not included in the condition (4.13) inferring that one can not fix this problem of a divergent motion by just using shorter sampling time, i.e., the key role here is not the continuity of our measurements but the internal dynamics of turbulent structures.

The real dynamics of turbulence contain both divergent and linear motions and, in fact, more complex dynamics including bending, stretching and so on. The close mixture of these motions complicates the velocity vector field reconstruction.

We would like also to illustrate the performance of the Horn-Schunk technique on another test pattern which represents large frame-to-frame displacements of turbulent structures, i.e., when the displacement is comparable to a size of structures. In that case, the condition (4.6) is satisfied only marginally. Results are shown in Fig. 4.3. The circular shape of the structure is taken for simplicity. In this example, the structure displaces from Fig. 4.3(a) to Fig. 4.3(b) over a distance approximately equal to it's own size. Figure 4.3(c) shows the derived velocity map corresponding to a weakly smoothed field with the smoothing parameter $\alpha = 0.03$. As in the previous case, we could not chose the zero smoothing parameter α due to high outliers in the vector field sought. It is clearly seen that the weakly smoothed approach results in significant errors and outliers. This is primarily the consequence of the optical flow limitation. With the higher smoothing parameter $\alpha = 0.5$ in Fig. 4.3(d) the velocities are tracked more or less correctly so that spurious velocity components are "washed out". However, this also washes out some spatial details of the flow. For instance, some essential velocity vectors are visible far from the spatial localisation of both structures in Figs. 4.3(a) and (b). Therefore, the smoothing parameter $\alpha = 0.5$ in Fig. 4.3(d) was chosen to strike a balance between these competing factors. Nevertheless, whatever smoothing parameter α we choose, the large displacement of turbulent structures is one of the key challenges in the optical flow approaches. In the general case, the correct reconstruction of the velocity vectors for large displacements requires some advanced approaches, supplemental or alternative to optical flow methods.

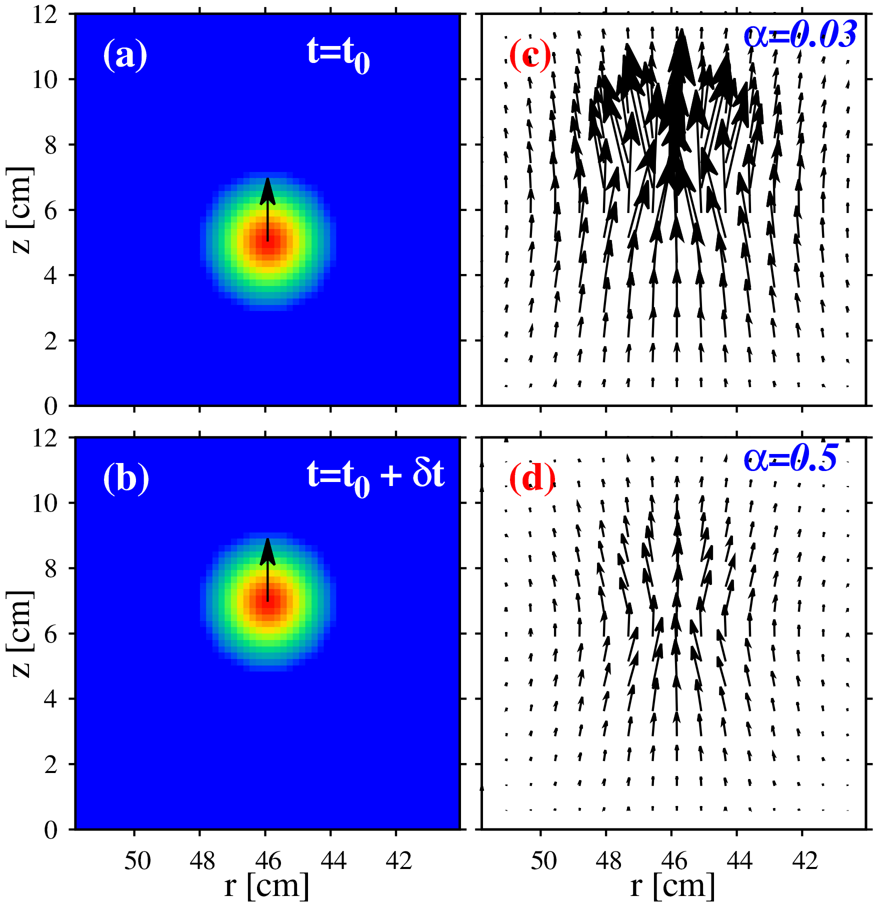

Figure 4.3: Illustration of the performance of the Horn-Schunk technique on large frame-to-frame displacement. (a)-(b):Artificial intensity map showing some typical turbulent structure propagating through the scene upward in the direction of the arrow. (c)-(d):Derived velocity maps using the Horn and Schunck algorithm for two values of the smoothing parameter α.

4.4 The improved estimation of optical flow based on the multiresolution strategy

In our work, we used the improved algorithm, which implements so-called "multiresolution scheme", in addition to the traditional Horn and Schunck method.

Except of the linear translational movement, turbulent structures also exhibit bending, stretching and even more complex deformations (formation of tails and bridges due to interaction between structures). Therefore, there is the supplementary problem of local minima, caused by the complexity of turbulence dynamics. The problem of local minima means that the energy functional of Eq. (4.7) can have multiple local minima even though there exists a much better global one. Consequently, the local minimization strategies converge depending on the initialization in the vicinity of one of these local minima. There is no common efficient method that can overcome this problem of local minima and guarantee a global optimisation. One popular solution is the use of multiresolution methods. The basic idea is to transform the complicated original functional to a simplified smoother functional, where a unique minimum exists. The smoothing of the image can remove minor unnecessary details in the dynamics of the structure leaving only reciprocal motion. Basing on the idea that the minimum of the simplified functional is a good initialization for solving a less simplified one, it becomes possible to reach the global optimum of the original functional step by step. The full pyramid of images is used, starting with the smallest possible image at the coarsest grid. As soon as a fixed solution is reached, the resolution is changed to the next finer scale and the result is used as an initialization for the iteration on this scale. The numerical scheme used in this section combines both the Horn and Schunck method and a multi-resolution optimisation strategy. It is widely accepted (see for instance [13,72,69]) that this improvement gives a more accurate velocity vector field (although not perfect) than the conventional Horn and Schunck method alone. The details of the numerical implementation can be found in the more specific discussion in Ref. 72.

4.4.1 Test of the multiresolution approach

In order to assess the relevance of the multi-resolution approach to our work, the technique has been applied to TEXTOR GPI data. Figures 4.4(a) and (b) show typical GPI frames where some turbulent structure travels vertically up in the poloidal direction and radially outward. The motion is visible as a displacement of the front edge of the structure (indicated by black dashed and solid lines) between figures 4.4(a) and (b). The displacement direction is shown by green arrows in figure 4.4(b). Figure 4.4(c) illustrates the derived velocity fields showing the noticeable motion of the structure in predominantly poloidal direction upward. Values and directions of derived velocities approximately correspond to the real motion, (which is shown by green arrows in Fig. 4.4(b)) of the structure in Figs. 4.4(a) and (b). On the other hand, it is clearly visible that our optical flow approach provides correct reconstruction of the vector field only in the region where there are identifiable structures in the brightness. In fact, this is the essential feature of the majority of optical flow algorithms. In that sense there is a little hope of finding the velocity vectors for quiet and laminar flows (without turbulent structures). In some approaches a brightness threshold is set, below of which the velocity vectors are not shown, i.e., the vector field is displayed only where there are some pronounced structures in the brightness [14], thus enabling a high level of ∇I. Figure 4.4(d) shows such an example. This technique was used for the processing of GPI data in this work.

To illustrate the temporal dependence, time traces of the poloidal velocity $v_\theta(t)$ and radial velocity $v_r(t)$ measured using the optical flow method for the shot #115361 are shown in Fig. 4.5. In the figure, each time trace represents values, corresponding to the radial position $r \approx 44\ cm$ (approximately 3.5 cm inside the separatrix), which is within the 2 cm distance from the time-averaged GPI intensity maximum. The GPI intensity is normalized by subtracting from each pixel its mean value taken over the full 300-frame exposure and then dividing by the root mean square (rms) of fluctuations, as described in Sec. 3.3. Typically, the poloidal velocity fluctuates between $\pm 1.5\ km/s$ around the mean value of $\bar{v}_\theta = 0.8\ km/s$. These values for the radial velocity are $\pm 1.4\ km/s$ and $\bar{v}_r = 0.4\ km/s$, respectively. We would like to go ahead and note that $\bar{v}_\theta = 0.8\ km/s$ is in good agreement with $v_{E_r \times B} = 0.75\ km/s$ velocity in the edge for the same shot #115361 in Fig. 5.1(d)(black line) and very close to the phase velocity of turbulence $\bar{v}_{ph} \approx 1\ km/s$ for the same shot in Fig. 5.2(black line), measured using the time-delay estimation method.

4.5 Identification of zonal flows using optical flow analysis of GPI data

The time-dependent poloidal velocity of edge turbulence could be used for the identification of the time-varying large-scale poloidal flows(zonal flows) in the plasma edge. These zonal flows are naturally formed in the majority of TEXTOR discharges. More details on the nature of these flows will be given in chapters 7 and 8. In this paragraph, the search of such zonal flows using the optical flow analysis provides an additional test of our algorithm for reconstruction of velocity vector field. In the first step of this test, the sample time dependence of the poloidal velocity field $v_\theta(t)$ has been derived from GPI data in the same way as it has

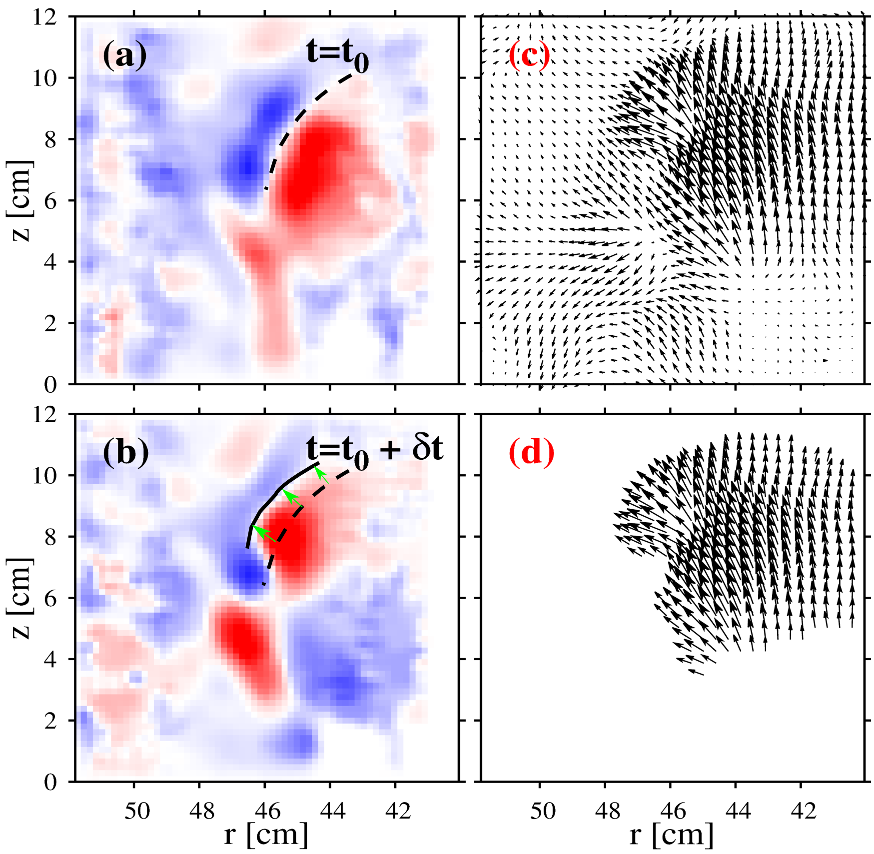

Figure 4.4: Performance of the "improved optical flow" technique on typical GPI data. (a)-(b):Intensity maps for two GPI frames for TEXTOR shot #115361 showing some structure propagating poloidally upward and radially outward. The propagation direction is shown by green arrows in figure (b). (c):Derived velocity fields. (d):Vector field only in the region where there are identifiable structures in the frame area.

been discussed in the previous section. The analysis has been done for representative TEXTOR discharges where zonal flow fluctuations in the frequency range $\sim 8-11\ kHz$ are clearly observed in the Langmuir probe data (in the frequency spectrum of $\tilde{\phi}_{fl}$). Note that these $\sim 8-11\ kHz$ zonal flow fluctuations have been systematically studied at TEXTOR and identified as GAM zonal flows [41–43]. Fluctuating velocity data were taken in the plasma edge $46\ cm > r > 42\ cm$ because zonal flow structures are thought to exist in the closed field line region. Figure 4.6 shows the frequency spectra for this test. It compares the frequency

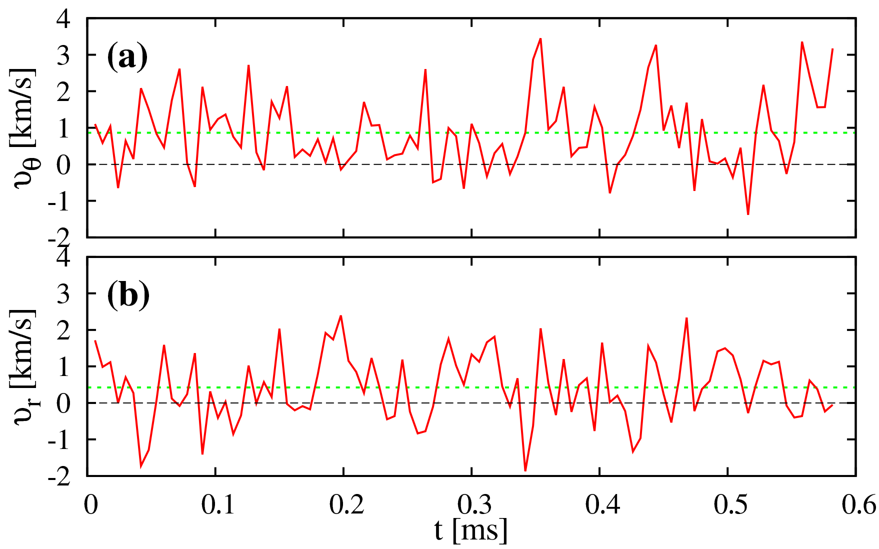

Figure 4.5: Time traces of the poloidal (a) and radial (b) components of the velocity of turbulent structures derived from GPI data using the optical flow method. The time traces correspond to the radial position of $r \approx 44\ cm$

spectrum of the poloidal velocity $\upsilon_\theta(t)$(red line) with that spectrum of $\tilde{\phi}_{fl}$(green line). The spectrum of $\upsilon_\theta(t)$ has been averaged over 4 different discharges with similar conditions. It is visible that both spectra overlay one upon another in the

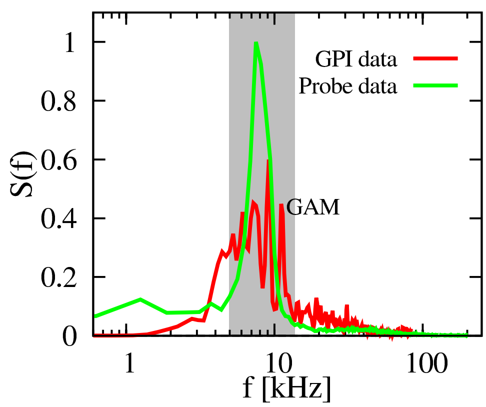

Figure 4.6: (red line) frequency spectrum of $\upsilon_\theta(t)$ derived using GPI data. (green line) frequency spectrum of $\tilde{\phi}_{fl}$. The pronounced peak in the frequency range $\sim 8 - 11\ kHz$, associated with GAM zonal flow fluctuations, is visible in both spectra.

frequency range of GAM zonal flows. This correspondence shows that poloidal velocity field evaluated using GPI data could be used as an additional tool for studies of edge turbulence velocity, together with Langmuir probes and other diagnostics.

4.6 The complementary approach based on the two-dimensional cross-correlation

Based on the limitations of the optical flow technique, one would like to discuss another promising approach in the context of further development of our algorithm in the future. This approach has been implemented and acts to alleviate some systematic drawbacks exhibited by the optical flow. In this approach the subsections of each image are correlated with subsections of previous and subsequent images to form a map of local translation or velocity. The displacement vector for each subsection is calculated from the position of the maximum of the two-dimensional (2D) cross-correlation function. This maximum corresponds to the offset of the matching exhibiting the highest similarity between subsections. The normalised cross-correlation function tends to be independent of the magnitude of both correlated samples and, therefore, this approach should be less sensitive to the divergent/convergent motion of turbulent structures discussed in Sec. 4.3. Meanwhile, the cross-correlation technique has an advantage over the optical flow technique in that it is free of the intensity constancy assumption and, therefore, the local velocity vectors are not constrained to lie merely along the local intensity gradient.

In order to illustrate the performance of the cross-correlation approach and to demonstrate the improvement gain over the traditional optical flow method, the test image sequence together with the velocity maps are shown in Fig. 4.7. The typical turbulent structure was translated vertically from Fig. 4.7(a) to (b). Figures 4.7(c) and (d) show the derived velocity field maps, corresponding to two different values of the operation parameter ρ_c. The parameter ρ_c defines the maximum search radius for the cross-correlation between two neighboring subsections of the image. If this search radius is less than the real displacement of the structure then the reconstruction of the displacement becomes unreliable as seen in Fig. 4.7(c). However, once the search radius is extended and embrace the real displacement zone, the most accurate velocity field reconstruction is achieved, and such an example for $\rho_c = 10$ is shown in Fig. 4.7(d).

It is seen that the cross-correlation algorithm, applied to the simple motion of solitary structure, gives substantially more accurate velocity vector maps than the traditional optical flow methods. However, when this analysis is applied to real complex turbulent motion, it tends to provide more suspicious results. Therefore, this technique, when used alone, is less relevant for studies of turbulent motion and has not been used for the GPI data processing in our work. However, further

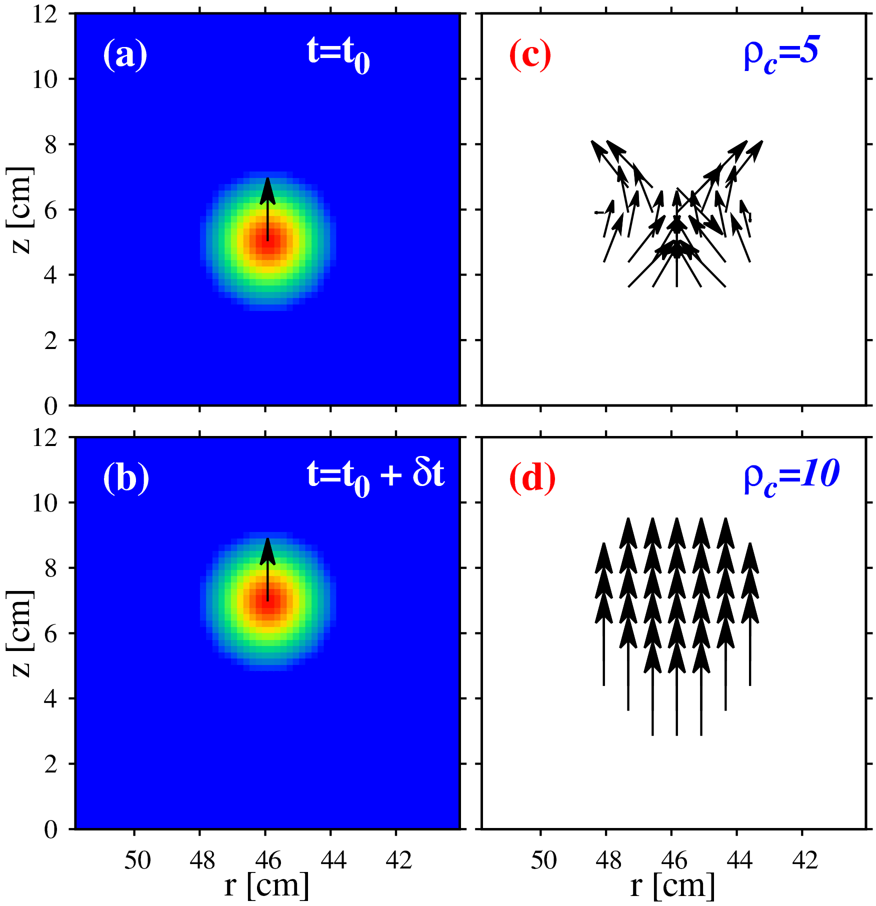

Figure 4.7: Performance of the cross-correlation technique on large frame-to-frame displacement for two different values of the operation parameter ρ_c. The parameter ρ_c defines the maximum search radius for the cross-correlation between two neighboring subsections of the image. (a)-(b):Artificial intensity map showing some typical turbulent structure propagating through the scene upward in the direction of the arrow. (c)-(d):Derived velocity maps for two values of the operation parameter ρ_c.

improvements of this technique are considered to be promising. We are counting on significant improvements of the velocity vector field reconstruction using the hybrid technique, when the outcome from the cross-correlation technique is used as an input to the optical flow technique. The idea to implement such a hybrid algorithm is not novel [14] and is the subject of our future activity.

4.7 Summary and future work

The basic principles which underlie the optical flow analysis was described in this chapter. It is clear from this chapter that the traditional optical flow method works only for limited range of scales and intensities of structures, representing some “typical” turbulent eddies.

We have shown that the derivation of the poloidal displacement of poloidally stretched turbulent structures (shown in Fig. 4.1) is the subject to some obstacles imposed by the optical flow constraint. Although, such type of stretched structures is very typical for plasma turbulence, especially in weakly sheared flow regimes, one should be carefull with the interpretation of the results. Special emphasis must be put on the centre of the structure, where the change in ∇I is marginal and optical flow tends to underestimate the absolute value of the velocity. This is especially important in the light of the role of stretched structures for the Reynolds stress production [73, 74]. However, albeit in slightly deformed fashion, the derived velocity vector fields for these structures are qualitatively correct and do not reveal a spurious nature. We have shown that both (a) the divergent/convergent motion of turbulent structures, associated with their fast growth or decay and (b) large frame-to-frame displacements of turbulent structures between two consecutive frames are challenging problems for the correct reconstruction of the velocity field.

In this work we used the algorithm, which uses the multiresolution (coarse-to-fine) strategy. There is a problem of local minima of the functional (4.7) caused by the fact that the turbulent structures do not simply move but also change the shape, i.e., they are simultaneously bended, stretched and flattened. The smoothing of images removes these small details, remaining only a translational motion. Therefore, one can expect that the energy functional containing smoothed images has considerably less local minima. In fact, the downsampling of the image removes small details in the same way as a smoothing. In addition, it leads to a much more fast performance of the algorithm. In the multi-resolution technique the output from the coarse image is used as an initialization at a finer scale. The full pyramid of images is used, starting with the coarsest grid.

4.7.1 Future directions

As a matter of a further development in the future, significantly more challenging dynamics is the divergent/convergent motion, associated with the fast growth or decay of a structure as shown in Fig. 4.2. This obstacle is also the consequence of the brightness constancy assumption. Some technique to deal with this problem has been proposed, for instance, in Ref. 67. They claim that the brightness constancy assumption turns to be inappropriate for the turbulent motion. Indeed, the image sequences involving turbulent motion often exhibit dramatic temporal change of brightness. A number of physical processes, depending on the nature of the flow and the principle of imaging, can be responsible for such kind of behavior. Obviously, the turbulent motion naturally does not impose any constancy on the amplitude of the turbulent structures along trajectories. In addition, the simulation performed for the NSTX and C-Mod tokamaks [44, 59] shows that the GPI light intensity is some nonlinear function of both n_e and T_e. Consequently, the influence of T_e can not be completely excluded for all individual structures along their trajectories. Based on these considerations, an alternative brightness constraint, which would be more suitable for the physics of turbulence, has been proposed. The suggestion is to use directly the continuity equation (4.5), as a more physically-grounded constraint. The assessment of the validity of this new brightness constraint in the particular case of the GPI imaging is the subject of our future work.

The 2D cross-correlation approach, followed by the optical flow technique, is considered to be the promising strategy. The cross-correlation method applied to the simple test sequence of the motion of an isolated structure gives substantially more accurate results than the conventional Horn and Schunck algorithm, as has been shown in Fig. 4.7. The cross-correlation technique has an advantage over the optical flow technique in that the local velocity vectors are not constrained to lie along the local intensity gradient. However, this technique, when applied to a real turbulent motion, which is far from being so regular as in Fig. 4.7, tends to produce spurious results, primarily due to the spontaneous change in the shape of turbulent structures. Therefore, this technique, when used alone, is not suitable for studies of turbulent motion. However, some hybrid combination of two techniques, in which the output from one technique is used as an input to another algorithm, could overcome the limitations imposed on each of these techniques individually. This is also the subject of further improvements of our algorithm.

5

The natural $E_r \times B$ flow shear layer in the edge of TEXTOR

Our motivation for edge flow studies is that the turbulence-flow interaction is an important aspect of edge physics. The interest in the study of plasma rotation arose due to understanding of the role of $E_r \times B$ flow shear in the suppression of turbulence and reduction of radial transport. The dynamics of and an interplay between mean shear flows, zonal flows and turbulence modes are key mechanisms behind the turbulence-flow interaction [25, 75]. The suppression of turbulent transport in the edge region is believed to result from the formation of a localized region of sheared poloidal rotation, the so called "*shear layer*". The local reduction of fluctuations in the shear layer is observed at the L-H transition [17, 18] as well as in standard ohmic regimes [19, 20].

The deep understanding of the turbulence-flow interaction requires the detailed characterisation of the poloidal flows in the plasma edge. In this chapter, experiments on the measurement of the edge poloidal flow at TEXTOR are reported. In Sec. 5.1, the basic model of the formation of the natural mean poloidal plasma rotation is presented. One of the traditional ways of characterising the mean poloidal plasma rotation in the edge is based on the estimation of the phase velocity of plasma turbulence. However, one should understand that the link between the turbulence phase velocity and poloidal plasma rotation velocity is very indirect. This issue will be also discussed in details. The measurements of the phase velocity have been done using the time-delay estimation between turbulence signals from two poloidally separated points. The corresponding measurements using the Langmuir probe and GPI diagnostics are compared to the edge $E_r \times B$ poloidal flow. These results are discussed in Sec. 5.2.

5.1 Model for the formation of the edge $E_r \times B$ flow.

The complete picture about the formation of mean edge flows in toroidal plasmas is not yet clear. The $E_r \times B$ rotation of the bulk plasma and that of the SOL are determined by different physics, because the field lines are closed in the plasma but connected to the limiter in the SOL. Consequently, each region has different equations describing the averaged poloidal rotation and must be dealt with separately. The poloidal rotation in the SOL is presumed to arise from a potential sheath parallel to the magnetic field that exists near the limiter due to fast electron runaway to the limiter surface. The real mechanism of poloidal rotation in the bulk plasma, however, is of some debate [76]. Some distinct mechanisms have been proposed to drive poloidal rotation in the closed flux region: ion orbit loss [77,78], Reynolds stress [58] and anomalous Stringer spin-up. However, the majority of models are variations of the well-established neoclassical theory. In that context, this would be the appropriate place to mention the following references: 58, 79–84.

In the following excerpt we provide a qualitative explanation of the nature of poloidal plasma rotation in the closed flux region. The starting point for the derivation of poloidal rotation velocity is the momentum balance equation for each particle species α

$$m_\alpha n_\alpha(\frac{\partial \vec{v}_\alpha}{\partial t} + (\vec{v}_\alpha \nabla)\vec{v}_\alpha) = -\nabla p_\alpha - \nabla \cdot \hat{\Pi}_\alpha + Zen_\alpha(\vec{E} + \vec{v}_\alpha \times \vec{B}) + \vec{R}_\alpha, \quad (5.1)$$

where Z is the charge number of the particle and $\vec{v}_\alpha$ is the fluid velocity of a given species. Here, we consider a completely ionised two-component plasma with electron ($Z = -1$) and ion ($Z = 1$) particles only. Considering stationary flow ($d\vec{v}_\alpha/dt = 0$) and neglecting the viscosity term ($\nabla \cdot \hat{\Pi}_\alpha = 0$), the corresponding equations for the ion and electron components are the following:

$$\begin{aligned} -\nabla p_e - en(\vec{E} + \vec{v}_e \times \vec{B}) + \vec{R}_{ei} = 0 \\ -\nabla p_i + en(\vec{E} + \vec{v}_i \times \vec{B}) + \vec{R}_{ie} = 0 \end{aligned} \quad (5.2)$$

with the collision term given by $\vec{R}_{ei} = m_e n(v_e - v_i)\nu_{ei}$. In the expression for the collision term, we neglect the thermal force, proportional to the electron temperature gradient ∇T_e.

The radial projections of equations 5.2 then read:

$$\begin{aligned} -\frac{dp_e}{dr} - en(E_r + v_{\theta e} B_\phi) = 0 \\ -\frac{dp_i}{dr} + en(E_r + v_{\theta i} B_\phi) = 0. \end{aligned} \quad (5.3)$$

Here, we have tacitly assumed that the collision term $\vec{R}_{ei}$ does not have a radial component. Otherwise, it implies the radial current, which would be unphysical. Thus, poloidal velocities for both species are expressed from Eqs. (5.3) as follows:

$$\begin{aligned} v_{\theta e} &= -\frac{1}{enB_\phi}\frac{dp_e}{dr} - \frac{E_r}{B_\phi} \\ v_{\theta i} &= \frac{1}{enB_\phi}\frac{dp_i}{dr} - \frac{E_r}{B_\phi}. \end{aligned} \tag{5.4}$$

One can see that poloidal rotation velocities for both electrons and ions have only two components: the diamagnetic rotation term $v_D \propto dp_{e,i}/dr$ and the $E_r \times B$ rotation $v_{E_r \times B} \propto E_r/B_\phi$.

On the other hand, the poloidal projections of Eqs. 5.2 are the following:

$$\begin{aligned} env_{re}B_\phi - m_e n(v_e - v_i)\nu_{ei} = 0 \\ -env_{ri}B_\phi + m_e n(v_e - v_i)\nu_{ei} = 0 \end{aligned} \tag{5.5}$$

Now, substituting poloidal velocities from (5.4) into (5.5), we get:

$$v_{re} = v_{ri} = -\frac{m_e \nu_{ei}}{e^2 n B_\phi^2}\frac{d(p_e + p_i)}{dr} \tag{5.6}$$

Obviously, the radial transports of ions and electrons are equal and, therefore, do not lead to the formation of E_r. In that context, it is said that the classical radial transport in a completely ionised plasma is "naturally" ambipolar.

Alternatively, the radial velocities of electrons and ions might also be interpreted as a result of $\vec{R}_{ei} \times \vec{B}$ drift. Because of the property that $\vec{R}_{ei} = -\vec{R}_{ie}$ and since both particles have equal and opposite charges, the corresponding radial drifts are equal. The origin of the radial electric field becomes understandable when one takes into account the viscosity term in the momentum balance equation (see for instance [85, p. 204]; [86, pp. 118 and 246]). This is the starting point of the neoclassical theory of plasma rotation.

The poloidal viscosity term in the momentum balance equations is often referred to as being the result of *poloidal flow damping*. The poloidal rotation viscosity and associated decay of the poloidal rotation have been theoretically identified as the work done by *magnetic pumping* [87, 88]. The reason for the poloidal rotation damping is the toroidal shape of a tokamak and resulting difference between the toroidal magnetic fields on the low-field-side and the high-field-side. A poloidally rotating plasma sees a time-varying field when it moves from the low-field-side to the high-field-side of the tokamak. This is equivalent to the motion of particles in a magnetic mirror. Due to conservation of the magnetic moment of the particle $\mu_m = m_\alpha v_\perp/2B$, when it moves to the high-field-side, its energy parallel to the magnetic field $m_\alpha v_\parallel^2/2$ will be continuously transferred to the perpendicular energy $m_\alpha v_\perp^2/2$. If a particle experiences collisions on the high-field-side, then it will redistribute its extra perpendicular energy into the thermal energy channel, leading to net reduction of $\upsilon_\perp$ after the return to the low-field-side. In other words: the poloidal rotation decays because the kinetic energy of the poloidal rotation is used to heat the plasma.

When the viscosity term is included, the radial velocities are not equal anymore:

$$\begin{aligned} \upsilon_{re} &= -\frac{m_e \nu_{ei}}{e^2 n B_\phi^2} \frac{d(p_e + p_i)}{dr} + \nabla \Pi_e^{neo} \\ \upsilon_{ri} &= -\frac{m_e \nu_{ei}}{e^2 n B_\phi^2} \frac{d(p_e + p_i)}{dr} + \nabla \Pi_i^{neo} \end{aligned} \tag{5.7}$$

The viscosity term for electrons is less than that for ions by a factor of $\sqrt{m_i/m_e}$, therefore, the net outward radial velocity is defined mainly by the ion contribution. This violates ambipolarity, and the negative E_r rises to the value such that the $E_r \times B$ drift cancels the mean poloidal ion viscosity:

$$\nabla \Pi_i^{neo} \approx 0. \tag{5.8}$$

In fact, the viscous force acting in the poloidal direction depends on υ_θ [85]: Then the ambipolar radial electric field follows from $\upsilon_{\theta i}$ set to zero:

$$\upsilon_{\theta i} = \frac{1}{enB_\phi} \frac{dp_i}{dr} - \frac{E_r}{B_\phi} = 0 \Longrightarrow E_r = \frac{1}{en} \frac{dp_i}{dr} \tag{5.9}$$

The resulting $E_r \times B_\phi$ drift cancels the diamagnetic drift of ions. For the electrons, the $E_r \times B_\phi$ drift points in the same direction as the electron diamagnetic drift. Provided that $p_e = p_i = p$, it results in a velocity $\upsilon_{\theta e}$ which is twice the diamagnetic one:

$$\upsilon_{\theta e} = -\frac{2}{enB_\phi} \frac{dp}{dr} \tag{5.10}$$

Our previous discussion was primarily expository in nature, and therefore we have not striven for the greatest quantitative accuracy. More complete neoclassical considerations (see for instance [80, p. 272]; [81]; [82, p. 100]) are based on the hydrodynamical description of plasma in a single fluid model [89, 90]. However, the models used in neoclassics to derive the poloidal flow are far from complete, and due to the complexity of the subject, there exists a wide range of models [83]. For instance, the neoclassical model in Ref. 79 leads to an expression for the neoclassical ambipolar radial electric field of the form:

$$E_r^{neo} = \frac{k_T}{e} \frac{\partial T_i}{\partial r} + \frac{T_i}{en} \frac{\partial n}{\partial r}, \tag{5.11}$$

where k_T depends on the plasma collisionality and has a value of order 1. The corresponding ambipolar poloidal velocity of the ions is the following:

$$\upsilon_{\theta i}^{neo} = (1 - k_T) \frac{1}{eB} \frac{\partial T_i}{\partial r}. \tag{5.12}$$

Because the $E_r \times B$ plasma rotation improves the confinement of a plasma, having a spontaneous radial electric field is very beneficial. Our previous discussion shows that a natural ambipolar radial electric field E_r is expected in tokamaks. The poloidal $E_r \times B_\phi$ rotation predicted by the neoclassics does not differ too much from real measured values. This is true not only for measured values but also for the direction of the resulting poloidal rotation.

Shortly summarising all that we have discussed in this section, one needs to point out several concerns about the poloidal rotation in the closed flux region, which have important experimental implications:

- Poloidal rotation velocities for both electrons and ions have only two components: the $E_r \times B$ rotation term $\upsilon_{E_r \times B}$ and the diamagnetic rotation υ_D

$$\upsilon_\theta = \upsilon_{E_r \times B} + \upsilon_D. \tag{5.13}$$

- According to neoclassics, the $\upsilon_{E_r \times B}$ drift is the consequence of the diamagnetic one.

- The $\upsilon_{E_r \times B}$ drift in the edge points in the same direction as the diamagnetic drift of electrons and in the opposite direction to the ion diamagnetic drift.

- In the experiment, one should clearly understand which of the two velocities is measured.

5.2 Measurements of the edge poloidal plasma rotation at TEXTOR

5.2.1 Edge E_r and $E_r \times B$ flow measured by a Langmuir probe

One of the traditional and simple ways of characterising the mean $\upsilon_{E_r \times B}$ velocity in the edge is based on Langmuir probe measurements. To estimate the $\upsilon_{E_r \times B}$ value, the experiments were carried out in a series of discharges for $B_T = 2.6\ T$ and a wide range of $\bar{n}_{e0}$ values: $\bar{n}_{e0} = (1.5-3.5) \times 10^{19}\ m^{-3}$. The measurements have been made in the plasma edge and the SOL using a fast reciprocating Langmuir probe system mounted at the midplane on the low field side of the torus. The probe system could be moved radially during each shot to infer the radial dependency of measured values. The mean $\upsilon_{E_r \times B}$ plasma rotation velocity is calculated from the first radial derivative of the plasma potential $\phi_p = \phi_{fl} + 2.8 T_e$, where ϕ_{fl} (floating potential) and T_e (electron temperature) are measured by a triple probe model. The results are shown in Figs. 5.1. Each curve in the figure corresponds to a certain value of $\bar{n}_{e0}$. Curves are distinguished by different colours corresponding to a certain value of $\bar{n}_{e0}$, which is indicated in the bottom-left corner of figure 5.1.

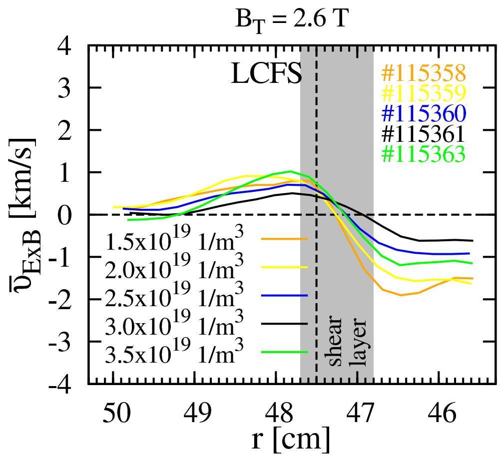

Figure 5.1: The radial profile of the $v_{E_r \times B}$ plasma rotation velocity in the plasma edge measured in shots with different $\bar{n}_{e0}$ values. The E_r value is estimated from the first radial derivative of the plasma potential $\phi_p = \phi_{fl} + 2.8T_e$, where ϕ_{fl} (floating potential) and T_e (electron temperature) are measured by a triple probe model. Different lines in a figure correspond to shots with different $\bar{n}_{e0}$ values

The separatrix position ($r \approx 47.5\ cm$) is shown by the vertical dashed black line. All curves are shown for the radial range (in terms of minor radius) from 50 cm in the SOL to 45.5 cm in the edge. It is noticeable in Fig. 5.1 that the poloidal flow in very far SOL regions is very marginal. However, it is rising gradually towards the centre and then falling in the plasma edge to certain significant negative values. Note that $v_{E_r \times B}$ changes the sign from propagation in the ion diamagnetic drift direction in the SOL to propagation in the electron diamagnetic drift direction in the plasma edge which is qualitatively consistent with the neoclassical model discussed in the previous section.

The narrow radial range (indicated by the grey colour) with a thickness of $1\ cm$, where the $E_r \times B$ velocity changes the sign from propagation in the electron diamagnetic drift direction in the bulk plasma to propagation in the ion diamagnetic direction behind the limiter, is called the *shear layer*. This velocity shear layer is an essentially universal feature of all tokamaks. For instance, a similar velocity shear layer has been characterized on the TEXT tokamak [19,20]. The radial location of the shear layer is independent of the plasma density and magnetic field for the range studied by us and it is always observed approximately 0.5 cm inside the LCFS. This layer is characterized by high velocity shear values

$$\frac{dv_{E_r \times B}}{dr} = \frac{dE_r}{Bdr} \tag{5.14}$$

Therefore, it plays an important role in the suppression of turbulent structures via the shear decorrelation mechanisms [21, 91].

5.2.2 Phase velocity of turbulence measured by probes and GPI

Rotation characteristics of plasma ions are measured by spectroscopic diagnostics such as charge exchange recombination spectroscopy. Our measurements, however, are based on measurements of plasma turbulence. In that case, one of the traditional and simple ways of characterising the mean poloidal plasma rotation in the edge is based on the measurements of the mean phase velocity of plasma turbulence $\bar{\upsilon}_{ph}$. In general, this phase velocity is not linked directly with the poloidal rotation for either electrons or ions. The phase velocity of a certain turbulent wave in the laboratory reference frame is the sum of the natural phase velocity of a given wave in the nonrotating plasma $\bar{\upsilon}^0_{ph}$ and the $E_r \times B$ rotation velocity

$$\bar{\upsilon}_{ph} = \bar{\upsilon}^0_{ph} + \upsilon_{E_r \times B}. \tag{5.15}$$

The phase velocity $\bar{\upsilon}^0_{ph}$ substantially depends on the physics of a given turbulent wave; be it drift wave, interchange wave, or other type of wave. Only in one particular case when the edge plasma turbulence is dominated by drift waves, the phase velocity of which is equal to the electron diamagnetic drift velocity [90, 92]

$$\bar{\upsilon}^0_{ph} = \upsilon_{De}, \tag{5.16}$$

the measured phase velocity of turbulence is equal to the electron poloidal rotation velocity

$$\bar{\upsilon}_{ph} = \upsilon_{De} + \upsilon_{E_r \times B} \equiv \upsilon_{\theta e}. \tag{5.17}$$

Therefore, as far as it is assumed that edge plasmas are dominated by drift-wave turbulence, the measured phase velocity is considered to be approximately equal to the poloidal rotation velocity for electrons. This has been shown, for instance, in the TEXT tokamak [93]. That is why measurements of $\bar{\upsilon}_{ph}$ might be used to characterise the electron poloidal rotation velocity.

In the experiment, $\bar{\upsilon}_{ph}$ is obtained via the time delay estimation (TDE) between fluctuation signals measured at two poloidally separated points (with known poloidal distance d). In the classical sense, the time delay estimation is identified from the position of the maximal value of the cross-correlation function between the reference and the delayed signals. The mean poloidal phase velocity can thus be evaluated as follows:

$$\bar{\upsilon}_{ph} = \frac{d}{\tau}, \tag{5.18}$$

where τ is the estimated time delay in the laboratory frame of reference. This approach also imposes another technical limitation that the time delay should be larger than the sampling time of the signals τ_s:

$$\tau \gg \tau_s, \tag{5.19}$$

implying that very fast motion where $\tau \ll \tau_s$ cannot be resolved. In addition, the TDE method works well only if the corresponding cross-correlation function has a well defined and well localised maximum. Otherwise, if the maximum is very broad and extended, the results will be very uncertain.

To estimate the $\bar{v}_{ph}$ value, the GPI experiments were carried out in a series of discharges for $B_T = 2.6\ T$ and a wide range of $\bar{n}_{e0}$ values. For this study, the emission intensity ($\tilde{I}_{camera}$) signals from two poloidally separated pixels were used and the time delays were inferred from the cross-correlation between these signals. The results are presented in Fig. 5.2. Note that Fig. 5.2 and Fig. 5.1

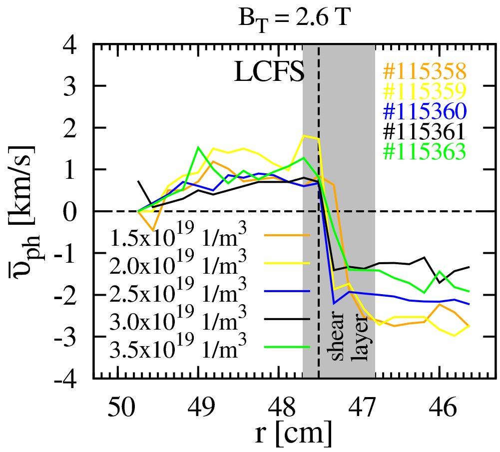

Figure 5.2: The radial profile of the mean poloidal phase velocity of fluctuations in the plasma edge measured with the time delay estimation technique in shots with $B_T = 2.6\ T$ and different $\bar{n}_{e0}$ values. The velocity is estimated on the basis of the time delay between two $\tilde{I}_{camera}$ signals measured at two poloidally separated CCD camera pixels. Different lines correspond to shots with different $\bar{n}_{e0}$ values (corresponding $\bar{n}_{e0}$ values are indicated in the bottom-left corner). The separatrix position is shown by the vertical dashed black line. The grey shadowed area indicates the position of the shear layer.

correspond to the same set of TEXTOR discharges. The B_T and $\bar{n}_{e0}$ values are indicated in the same manner as in Fig. 5.1.

It is noticeable that radial dependencies of $\bar{v}_{ph}$ in Fig. 5.2 show very similar behavior to $v_{E_r \times B}$ in Fig. 5.1. Higher $\bar{n}_{e0}$ values correspond to lower $\bar{v}_{ph}$ in the edge and the SOL in both figures. The explanation for the observed similarity is that in the presence of the mean radial electric field, the measured phase velocity is the sum of $v_{E_r \times B}$ and the phase velocity of turbulence in the nonrotating plasma $\bar{v}^0_{ph}$, as we discussed in the beginning of this section. The $\bar{v}^0_{ph}$ values in the edge and the SOL are substantially lower due to the small pressure gradient, and the poloidal rotation is defined primarily by $v_{E_r \times B}$.

5.2.3 Poloidal rotation velocity derived using the optical flow approach

Alternatively, one can use the optical flow technique to derived the radial profile of a poloidal velocity from GPI data, following the description in chapter 4. In this section (and everywhere in this work) we used the multiresolution optical flow approach, introduced in section 4.4. Before we present results in this section we briefly describe some features of this analysis.

- In many cases, a particular GPI frame is dominated by several bright structures. Therefore, the results of the optical flow method tend to represent the velocity of those structures. Indeed, that represents the quantity which is most physically interesting: the motion of brightest structures. However, in cases where a GPI frame contains relatively weak structures, and especially in cases where there are many structures superimposed upon each other, the optical flow analysis tends to produce spurious results. Thus, in our analysis, the results of the optical flow technique output are limited to include only those vectors corresponding to solitary structures with a brightness above some threshold (in other words, if we limit results to velocity vectors corresponding to solitary bright structures).

- Another important issue is the divergent/convergent motion of turbulent structures, associated with their fast growth or decay. We have discussed in section 4.3 that such a behavior can substantially affect optical flow results. Fortunately, the divergence is the quantifiable characteristic and might be taken into account when we interpret the results of the optical flow methods. In our analysis, the regions of high velocity divergence were also excluded.

Figure 5.3 is a plot of the average poloidal velocity profile derived from the optical flow technique. These results correspond to a set of shots with $B_T = 2.6\,T$ and different $\bar{n}_{e0}$ values. The $\bar{n}_{e0}$ values are indicated in the bottom-left corner. The average period length is about $1.7\,ms$.

The poloidal velocities in Fig. 5.3 in the edge are approximately consistent with the results in Fig. 5.1 or Fig. 5.2. Higher $\bar{n}_{e0}$ values also correspond to lower $\bar{v}_{OF}$ in the edge. However, this agreement is far from being admirable in the SOL. The optical flow technique tends to provide undervalued velocities in this region because the decay of turbulent structures appears to be very fast once they move out across the LCFS position. Due to fast decay, the magnitudes of turbulent structures in the SOL are substantially lower than typical magnitudes in the edge. However, as already mentioned in section 4.7, the optical flow method works only for limited range of intensities of structures, representing some "typical" turbulent eddies. Therefore, the velocity vector field corresponding to weak structures in the SOL tend to be oversmoothed, which results in undervaluation of velocity values.

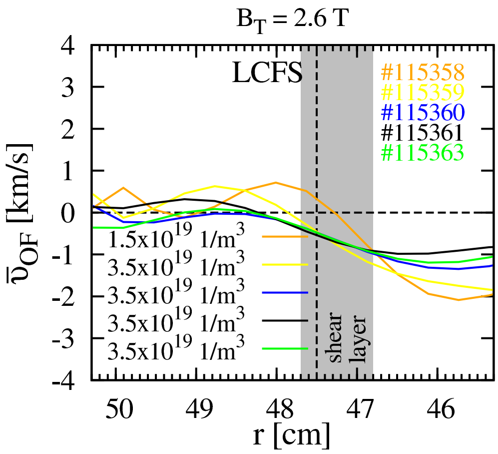

Figure 5.3: The radial profile of the mean poloidal velocity $\bar{v}_{OF}$ measured using the optical flow approach. The figure corresponds to a set of shots with $B_T = 2.6\,T$. Different lines in the figure correspond to shots with different $\bar{n}_{e0}$ values.

5.3 Summary of the edge flow results

In this chapter, the mean poloidal plasma flows in the edge have been systematically studied for different plasma densities and magnetic fields. On the basis of the measurements from the Langmuir probes and GPI diagnostics, the following conclusions can be drawn:

- We have shown that in the poloidal direction, the turbulent structures move downward in the SOL (along the ion diamagnetic drift direction) and upward in the plasma edge (along the electron diamagnetic drift direction), following up mainly with the $E_r \times B$ drift.
- GPI measurements give edge turbulence phase velocities of $-(1-3)\ km/s$. The corresponding velocities in the SOL are $1-2\ km/s$.
- The magnitude of the poloidal plasma rotation in the edge gradually reduces with increasing line-averaged density.
- The observed phase velocity of a turbulent wave is slightly higher than the $v_{E_r \times B}$ value. This seems to be a consequence of the shift induced by the eigen phase velocity of turbulence in the nonrotating plasma.
- The thickness of the shear layer, where the poloidal flow sharply changes sign, is estimated to be $5-8\ mm$.

6
Impact of the natural $E_r \times B$ flow shear on turbulent structures

It is well-known that turbulent transport can be reduced significantly in the presence of sheared flows due to their shearing effects on turbulent eddies. At present, there exists robust experimental evidence on the importance of the radial electric field (E_r) and associated $E_r \times B$ shear flows in reducing turbulent transport [17, 19, 20, 40]. There are two fundamental concepts of the theory of velocity shear effects on turbulence:

Stabilisation The effect of velocity shear on the growth of turbulent eddies

Stretching The effect of velocity shear on the stretching of turbulent eddies

Whereas the first concept considers the reduction of the growth rates of turbulence in the presence of the external sheared flow, the second one is based on the decrease in the effective correlation length of the eddy due to stretching or splitting processes. In the literature, the stabilisation and stretching mechanisms are usually referred to as *linear stabilisation* [94] and *radial decorrelation* [21, 33, 91, 95–97]. There are multiple of linear stabilisation mechanisms, since much of the physics is mode specific. The radial decorrelation mechanisms are in turn endowed with that universality which is needed to explain the suppression of turbulence by sheared flows observed on different machines in different regimes with various turbulent modes.

The radial decorrelation mechanism was proposed by Biglari, Diamond and Terry [21] (BDT model) and since that time their hypothesis has been supported by many experiments [8, 10, 20]. However, the interpretation of these experimental results is not necessarily straightforward because these measurements are based on the Langmuir probe measurements using the statistical two-point cross-correlation technique. The specific feature of the studies presented in this chapter is the use of essentially two-dimensional (2D) gas-puff imaging (GPI) measurements for a systematic study of the eddy decorrelation mechanism. For the first time we present the direct experimental evidence of eddy breaking by sheared flows in fusion plasmas. These sheared flows are spontaneous poloidal flows naturally formed in the plasma edge, as discussed in chapter 5.

The basic mechanisms which underlie the radial decorrelation are addressed in section 6.1. The experimental visualization of the radial decorrelation using essentially two-dimensional GPI measurements is presented in section 6.2. Main experimental results are summarised in section 6.3.

6.1 Nature of the radial decorrelation

In order to understand the mechanism of radial decorrelation, let's take a brief look at the nature of turbulent motion.

—***Nature of turbulent motion***

The driving mechnism of drift, interchange or balloning modes, which accounted for the main contribution to the plasma edge turbulence, is the pressure gradient. Therefore, the excited local turbulent modes will never decay, till they lead to the local "relaxation" of this gradient and, in this way, remove the causes of their development. An developed turbulent eddy leads to a flattening of the density gradient ∇n_0 in the spatial range of its size l_c (or coherence lengths). This implies that the lifetime of turbulent eddy τ_c is equal to the time needed for the eddy to travel (with the fluctuation velocity $\tilde{v}$) the distance approximately equal to its own size:

$$\tau_c^{-1} \approx \frac{\tilde{v}}{l_c}. \tag{6.1}$$

Such kind of stepwise turbulent transport is called the turbulent "diffusion", as opposed to "ballistic" transport, when the turbulent structures during the lifetime travel much further than l_c. The statements above are the basement for the *mixing-length model* of turbulent transport [85, p. 251, 91, p. 13]

$$\frac{\tilde{n}}{l_c} \approx \nabla n_0 \tag{6.2}$$

and the following approximation for the turbulent diffusion coefficient

$$D \approx \frac{l_c^2}{\tau_c}. \tag{6.3}$$

From what has been said, it follows that the growth of turbulent eddy and its decay are two closely linked processes.

Alternatively, the relation 6.1 can be viewed as the result of the self-advection of the turbulent flow $\tilde{\upsilon}$. At each position, the turbulent flow is a superposition of many eddies of different scales all contributing to the advection process. Therefore, the eddy size l_c can be thought of as roughly the distance between two adjacent eddies of comparable scales, a distance on the order of the eddy diameter in fully developed turbulence. Fluid elements that move an eddy size (with the speed of $\tilde{\upsilon}$) become subjected to the flows of other neighboring eddies and are no longer identifiable with their original eddy motion. In the absence of the background shear flow, the time scale for this loss of coherence defines the eddy lifetime. By the time an eddy moves the distance l_c, its energy has been transferred to other eddies and it has decayed. **In short, in order for the turbulent transport to be really "diffusive" transport, the eddy must decay at the moving distance approximately equal to its own size**. Indeed, this is the case if we have a look at TEXTOR GPI data showing two-dimensional displacement of turbulent eddies.

Figure 6.1 shows the set of GPI frames with some apparent turbulent eddy (indicated by the black arrow) with typical size of $\approx 2\ cm$, born in the edge plasma at the radial position of ≈ 45.5 cm. As soon as it is born, this eddy moves radially outward and continuously interfere with the flow of other neighboring eddies. In the end, the initial eddy is almost suppressed by the neighboring eddy at the radial position of ≈ 47.5 cm. Note that this process is not the merging of two small eddies into one large scale structure, though that is also possible for two-dimensional turbulence such as turbulence in magnetised plasma [85,p. 248]. Fortunately, one can say with an assurance that the decay or splitting of eddies as a result of their interaction is substantially more frequent and common process than the formation of large scale structures from small ones. Now we see that the radial turbulent transport in the edge of TEXTOR is of diffusive nature due to random and stepwise character of eddy motion.

—Radial decorrelation in shear flows

Now, let us come to the discussion about the influence of the sheared $E_r \times B$ flows on turbulent eddies. In the presence of a background shear flow whose speed varies transverse to the flow direction an eddy undergoes the differential stretching along the flow as different areas of the eddy are advected at different velocities. The key quantities here are the shearing rate ω_s and the eddy turnover rate (the natural scatterring rate of turbulence) ω_D. The shearing rate is defined as follows [21, 95]:

$$\omega_s = \frac{d\upsilon_{E_r \times B}}{dr} l_{cr} l_{c\theta}^{-1} = \frac{dE_r}{Bdr} l_{cr} l_{c\theta}^{-1}, \tag{6.4}$$

where l_{cr} and $l_{c\theta}$ are the radial and poloidal coherence lengths of turbulent eddies, respectively. The eddy turnover rate describes the rate at which eddies decay. It

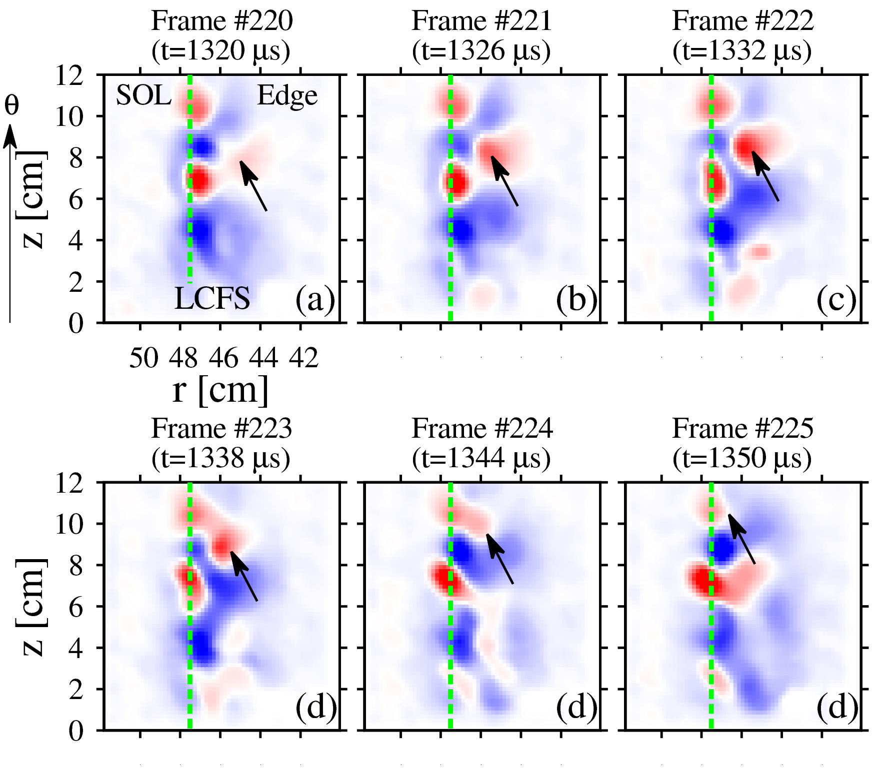

Figure 6.1: Time sequences of GPI images taken in the shot #115352. The eddy structure, which is born in the plasma edge, moves and concurrently decays. Finally, the eddy has decayed after passing the distance approximately equal to its own size.

can be roughly approximated by the inverse of the autocorrelation time of turbulent fluctuations measured in a region away from the flow shear.

According to the radial decorrelation model, when the shear strain rate ω_s is smaller than the eddy turnover rate ω_D, eddies are only marginally distorted by the flow shear. This picture is illustrated in Fig. 6.2(a). The effective decorrelation appears when the shearing rate ω_s is comparable to or greater than the natural scattering rate of ambient turbulence ω_D in the absence of the $E_r \times B$ flow. When the stretching length along the flow is equal to l_c, or distance to the next eddy, the eddy loses coherence and breaks up (see Fig. 6.2(b)) due to the random advection by other neighboring eddies. This results in multiple positive effects leading to the reduction of the turbulent radial transport

$$\varGamma = \langle \tilde{n}\tilde{v}_r \rangle, \tag{6.5}$$

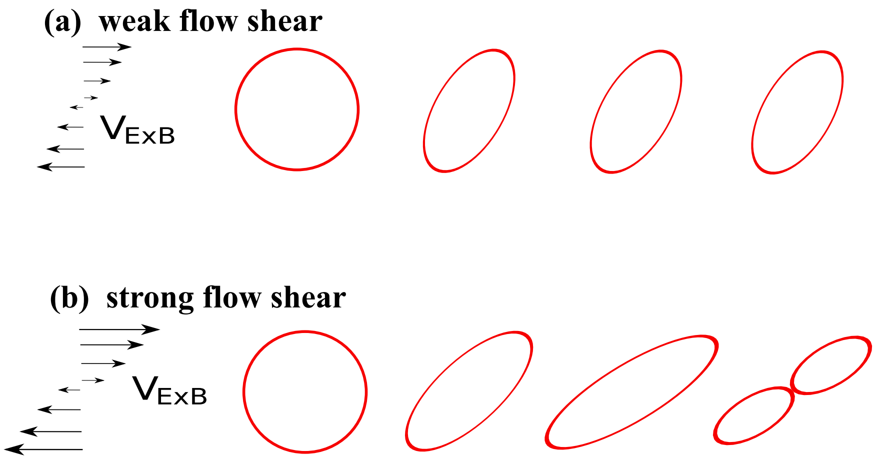

Figure 6.2: The effect of a velocity shear on a turbulent eddy: (a) illustrates the distortion of an individual eddy in a weak flow shear into an elongated elliptic shape. (b) shows the breakup of an individual eddy into two eddies when the stretching length equals to a coherence length. The loss of coherence reduces the eddy scale relative to that of the reference eddy.

where $\tilde{v}_r$ denotes the radial component of turbulent velocity fluctuations and angle brackets denote time average. These effects are the following:

- decrease in the radial correlation length of eddies
- change in the phase relationship between the density and velocity perturbations
- decreases in the amplitude of the turbulent fluctuations [91]

For instance, the decrease of the radial extent of the eddies essentially reduces the effective step size for turbulent transport according to the random-walk model [85,p. 223]. We refer the reader to Refs. 94, 95 for more information in this direction.

The link between a reduced transport and the sheared $E \times B$ flow arises from mixing-length estimate (see Eq. (6.2)) for a density fluctuations [91, 98]. In Fig. 6.3, the sheared velocity $V_y(x) = S_v x$ is superimposed on a turbulent eddy of size L. The stretching of the turbulent structure implies its transformation from circular to elliptic in shape (with a major and minor axes). In this process the perpendicular wavenumber (the wave number corresponding to a minor axis of the ellipse $k_\perp = 2\pi/L_\perp$) is effectively enhanced.

After a time t, the circular eddy becomes stretched ellipse with a major axis $L_l = L(1 + S_v^2 t^2)^{1/2}$. The conservation of an eddy area leads to an effective

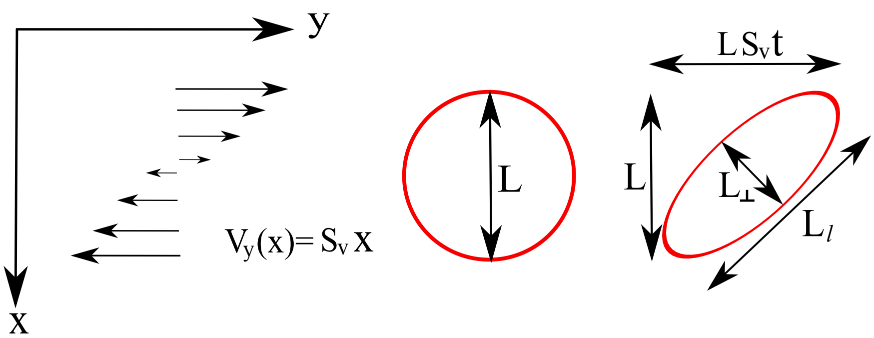

Figure 6.3: The stretching of an eddy in the sheared flow [91, 98]. The circular eddy is distorted into an ellipse after time t so that the major axis of the ellipse is given by $L_l = L(1 + S_\upsilon^2 t^2)^{1/2}$.

perpendicular wavenumber: $k_{eff} = k_{\perp 0}(1 + S_\upsilon^2 t^2)^{1/2}$. The time of this process t is limited by the correlation time τ_c, and

$$k_{\perp eff} = k_{\perp 0}(1 + S_\upsilon^2 \tau_c^2)^{1/2}. \tag{6.6}$$

Following to the mixing-length estimation in Eq. (6.2), the density fluctuations are suppressed relative to its value $\tilde{n}_0$ in the absence of the velocity shear:

$$\frac{\langle \tilde{n}^2 \rangle}{\langle \tilde{n}^2 \rangle_0} = \frac{1}{(1 + S_\upsilon^2 \tau_c^2)} \tag{6.7}$$

It imposes a significant reduction of fluctuations if $S_\upsilon \tau_c \gg 1$.

Experimentally, visualizing the predicted stretching of convective cells and eventually their break-up once the shear flows reach certain critical values, has been a challenge for experimentalists. Direct evidence of eddy tilting by shear flows has already been reported in toroidal devices TJ-II and NSTX [99] as well as in linear devices [8]. However, the eddy breaking by sheared flow have for the first time been observed by us in 2011. Details of these experimental studies are addressed in the sections below.

6.2 Experimental visualization by the GPI on eddy tilting/splitting by radially sheared flows

The contribution in this section addresses the systematic experimental study on the turbulence decorrelation by sheared flow. These sheared flows are spontaneous poloidal flows naturally formed in the plasma edge, as discussed in chapter 5. In order to directly view 2D (radial versus poloidal directions) edge turbulence structures, a GPI diagnostic has been used. For investigating the impact of mean $E_r \times B$ sheared flows on the turbulence eddy, the radial electric field E_r has been measured using fast reciprocating Langmuir probes. Technical details of the GPI and fast reciprocating Langmuir probe systems are addressed in chapter 3.

Figure 6.4 shows two sets of GPI images in two different shots [type (i) and type(ii)], each with an exposure time of 6 μs. Each image covers an area of 12×12 cm^2 in the radial vs poloidal plane. The vertical dashed line denotes the LCFS position (defined by the toroidal ALT limiter). As we are interested only in turbulent behaviors, we subtract the time-averaged mean values from the light intensity detected at each pixel for every image. The fluctuating light intensity is scaled by the colour bar at the right side and the turbulence eddy (coherent) structures can be seen in red colour (positive values). Here, we characterize each eddy structure by the local maximum of the light intensity in the contour plot of the image (red colour structures). Note that the eddies are mainly visible in the middle part of the image in the radial direction, because in the SOL the emission light is relatively weak due to very low temperature and in the inner edge area (r<44 cm) the neutral gas is fully ionized and thus no emission occurs there. From the time sequence of those pictures, we can see that the turbulent eddy is moving radially outward at a speed of $\upsilon_r \approx 300$ m/s. In the poloidal direction, the eddy moves downward in the SOL (along the ion diamagnetic drift direction) and upward in the plasma edge (along the electron diamagnetic drift direction), following up mainly with the $E_r \times B$ drift. The radial dependencies of the E_r detected by Langmuir probes for these two shots are depicted in Fig. 6.5(a), where one can clearly see a E_r shear existed in the edge region nearby the LCFS.

It is this $E_r \times B$ shear flow that plays a crucial role in stretching the turbulence eddy structure. As seen in images in Figs. 6.4(a, b) of type (i) and Figs. 6.4(g, h) of type (ii), when the eddy moves across the shear layer at $r \cong 47$ cm it starts to be tilted as different parcels in the eddy are advected at different $E_r \times B$ velocities in the poloidal direction. In the first image sequence of type (i), the images show a continuous tilting effect on the eddy when it passes through the shear layer and gradually becomes smaller owing to natural diffusive decay of the structure. However, for type (ii) the situation is rather different. The eddy is broken and split into two pieces at the time from 564 to 570 μs, as shown in Figs. 6.4(h) and (i). And then, the two small eddies continue to evolve individually. For both types (i) and (ii), in the tilt phase prior to breaking, the eddies show similar size of the radial (l_{cr}) and poloidal ($l_{c\theta}$) coherence length, as illustrated in Figs. 6.4(c) and (h). After the eddy breaking (see Fig. 6.4(i) in type (ii)), the radial correlation length l_{cr} is largely reduced, resulting in a reduction of the step size in turbulent transport, consistent with theoretical expectations [21, 33, 95]. It should be pointed out that such kind of eddy breaking by sheared flow have for the first time been observed by us in 2011.

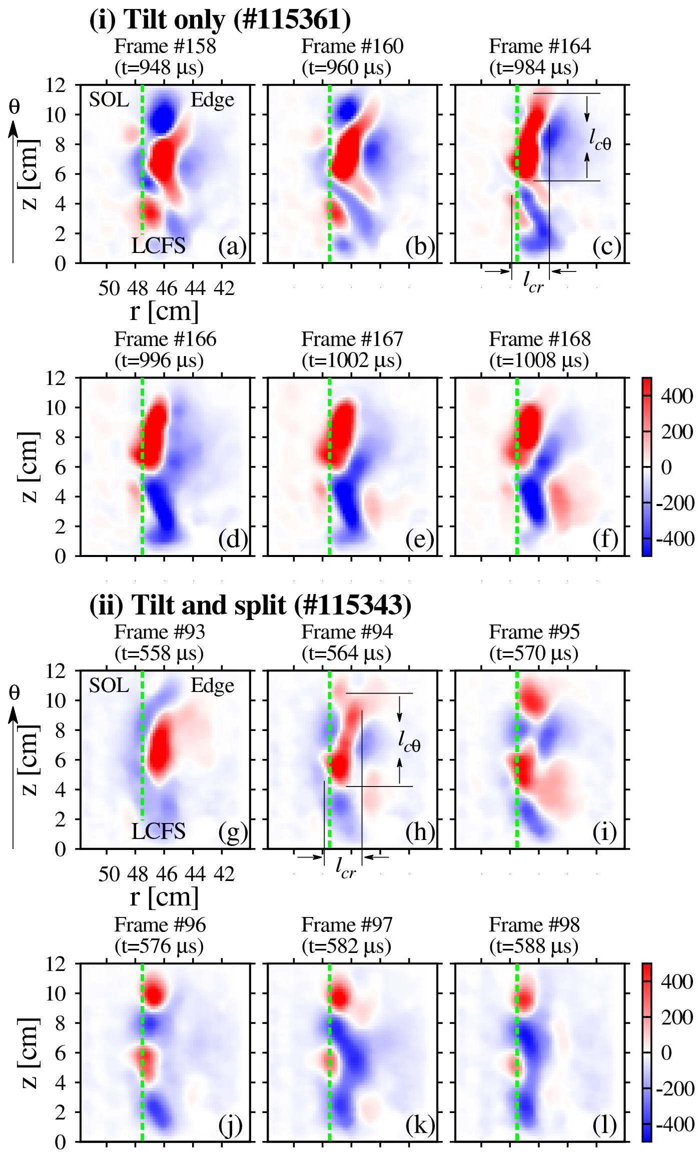

Figure 6.4: Time sequences of GPI images, showing the influence of $E_r \times B$ sheared flows on tilting and breaking the turbulence eddy at the edge of the TEXTOR tokamak for two different types: (i) The eddy structure is tilted only in the poloidal direction by a weak flow shearing; (ii) The eddy structure is tilted and broken by a strong flow shearing. The green dashed line denotes the LCFS location.

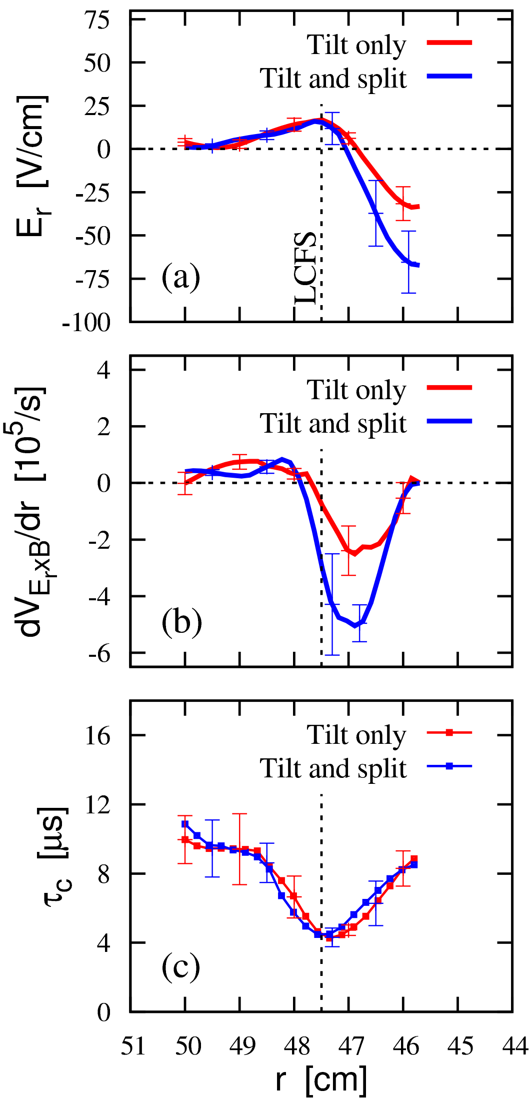

Figure 6.5: Radial profiles of (a) the mean radial electric field E_r, (b) $E_r \times B$ flow shear and (c) auto-correlation time in potential fluctuations measured by Langmuir probes for the two types of eddy evolution shown in Fig. 6.4. Data are averaged in similar discharges for each type: (i) "tilt only" and (ii) "tilt and split" of the eddy. The vertical dashed line denotes the LCFS position. The error bars indicate the standard deviation about the mean measured in similar discharges.

In order to understand the physics behind different behaviors of the turbulent eddy in types (i) and (ii), we compared the radial profiles of the $E_r \times B$ shear flow

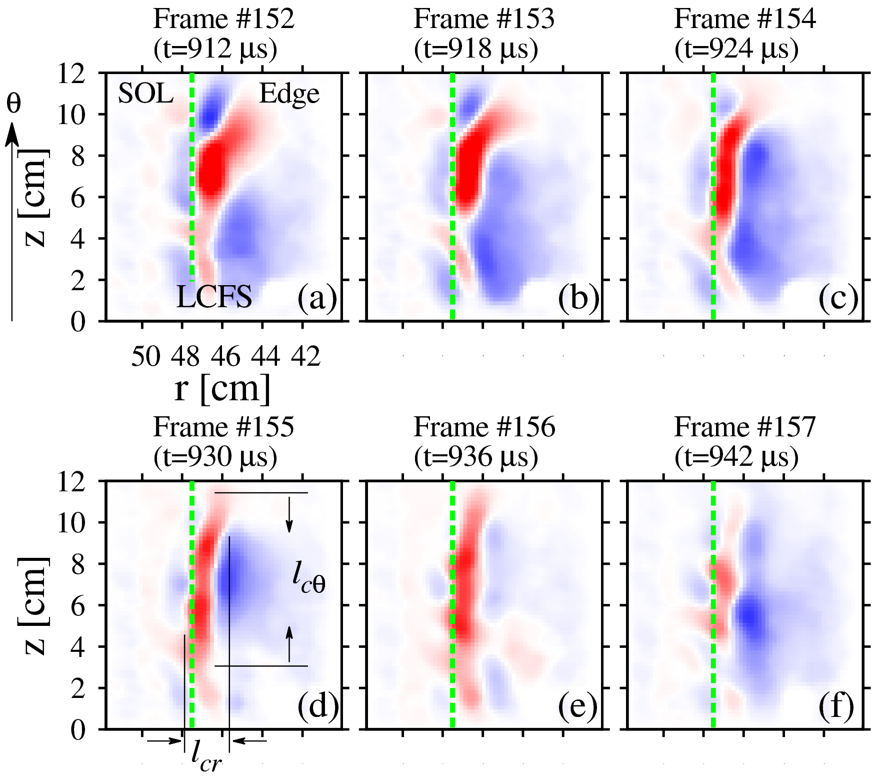

Figure 6.6: Time sequences of images taken in the same shot (#115343) as in type (ii) of Fig. 6.4 in a strong flow shearing case. The eddy is "tilted only" due to large poloidal elongation of the eddy structure along with a narrow radial extent.

in these two different type discharges. Plotted in Fig. 6.5 are the radial dependence of the mean E_r and $E_r \times B$ flow shear stated in Eq. (5.14). For each type, the profile is averaged over several similar discharges. Apparently, the poloidal $E_r \times B$ flow shearing, $d\upsilon_{E_r \times B}/dr$, is much stronger in the case of type (ii), where the eddy is broken. For further comparison with a simple Biglari-Diamond-Terry model [21], we calculated the ratio of the local $E_r \times B$ flow shear rate (which takes the eddy correlation lengths into account) ω_s, in the vicinity of the maximal shear layer, to the natural scattering rate of ambient turbulence, ω_D. Here we computed ω_D from the inverse of the autocorrelation time (τ_c) of potential fluctuations, i. e., $\omega_D = 1/\tau_c$. The radial profiles of τ_c for the type (i) and (ii) scenarios in figure 6.4 have been plotted in Fig. 6.5(c). Around the $E_r \times B$ flow shear region, the value of τ_c is generally decreased due to the flow shearing effects, as observed earlier in the TEXT tokamak [20]. In the region with strong rotations at r$\approx$ 46 cm, the τ_c detected in the laboratory frame of reference could be affected due to the "frozen-

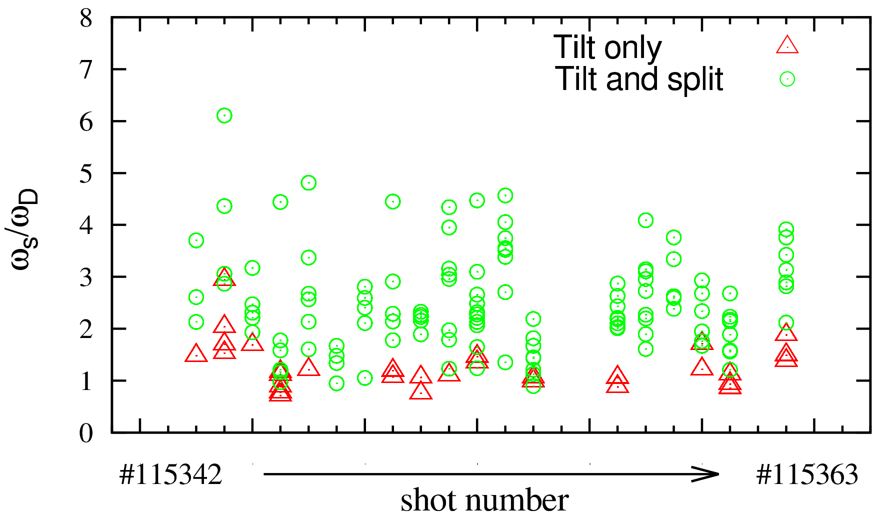

Figure 6.7: The ratio of the $E_r \times B$ flow shear rate (ω_s) to the natural diffusive scattering rate of ambient turbulence (ω_D) in a number of discharges at TEXTOR for the eddy "tilt only" and "tilt and split" events. The x-axis corresponds to different shot numbers.

flow" behavior, i. e., the decorrelation time (τ_{flow}) of eddy structures might be dominated by the correlation length and moving speed. Nevertheless, in our case this influence is small because $\tau_{flow} \approx l_{c\theta}/v_{E_r\times B} \approx 10-15\ \mu s$, which is slightly larger than the local τ_c values measured. Inside the shear layer, nearly the same reduction of τ_c under different flow shearing rates in type (i) and (ii) implies that the decrease in τ_c seems quite sensitive to a small shearing rate and is saturated at certain levels. In the shear-free zone, either in the SOL or at r≈ 46 cm, we get the natural (random without flow shear effects) turbulence decorrelation rate $\omega_D \approx 1 \times 10^5\ \mathrm{s}^{-1}$ for both cases. With values of $E_r \times B$ flow shear ($dv_{E_r\times B}/dr$) and radial/poloidal correlation lengths, we obtain $\omega_s = 1.2 \times 10^5\ \mathrm{s}^{-1}$ in type (i) and $\omega_s = 2.6 \times 10^5\ \mathrm{s}^{-1}$ in type (ii). Thus, the ratio of ω_s/ω_D is 1.2 and 2.6 for the "tilt only" and "tilt and split", respectively. Obviously, the occurrence of the eddy breaking depends on the magnitude of the flow shearing rate.

In this investigation, we have looked through 4940 (=260×19) images taken in 19 discharges. Among them, there are about 5% recorded the "tilt only" events [type (i)] of the turbulence eddy while 30% related to "tilt and split" events [type (ii)]. Each event can be seen in 5-10 successive images. The rest of the images are relatively ambiguous when watching for the flow shearing effects on eddies because each image contains several eddy structures with a mixture of the eddy dynamics.

In one shot, the ”tilt only” and ”tilt and split” events can also be seen in different periods of the discharge from the GPI images. Such an example is shown in Fig. 6.6 in comparison with those of type (ii) in Fig. 6.4 for the same shot #115343. In Fig. 6.4 the frames No. 93-97 show a breaking event of a turbulence eddy while in Fig. 6.6 the latter frames No. 152-156 illustrate a ”tilt only” event of another eddy. In the experiment, the probe measurements before and during the GPI exposure indicated that the edge equilibrium E_r profile is quite steady in a single shot. Because the GPI exposure only lasts 1.56 ms (260 images $\times$ 6μs/image) in one discharge, we reasonably assume that in one shot the mean E_r and $E_r \times B$ flow shear are roughly stable and the statistical decorrelation rate of turbulence is also constant during the GPI measurement. In such a case, the shearing effects on eddies will depend on the coherence dimension of the eddy structure, namely, the poloidal and radial correlation lengths ($l_{c\theta}$ and l_{cr}) [21]. A wide radial structure with a short poloidal extent is easier being tilted and broken, compared to a narrow radial one with a large poloidal elongation, and vice versa. This appears to be the case in our observations. In Fig. 6.6 when the eddy passes through the shear layer it is strongly elongated in the poloidal direction and the radial coherence length l_{cr} is slightly shorter, as compared Fig. 6.6(d) to Fig. 6.4(g). The shearing rate $\omega_s \propto l_{cr} l_{c\theta}^{-1}$ is therefore much weaker in case of figure 6.6, resulting in a ”tilt only” event of that eddy.

To substantiate the relation between the $E_r \times B$ flow shear rate and the eddy breaking phenomena, we have estimated the ratio of ω_s/ω_D in each type of the ”tilt only” and ”tilt and split” events observed in all discharges of this experiment. The results are depicted in Fig. 6.7. For all events the ratio is close to or above 1, revealing a fact that the eddy tilting can merely happen when the background flow shear rate exceeds the eddy scattering rate itself. In the case of ”tilt and split” (circular points) the value of ω_s/ω_D is much higher than that in the ”tilt only” (triangles). For the ”tilt only ” type the ratio is usually less than 2 whereas for ”breaking” type it is mostly in a range of 2-5. These data clearly demonstrate the crucial role of a strongly sheared $E_r \times B$ flow in breaking a turbulence eddy at the plasma edge.

6.3 Summary

In this chapter we present direct experimental evidence of eddy breaking and tilting events observed at the edge of the TEXTOR tokamak using a 2D GPI diagnostic.

In the following excerpt, the main poins of this chapter are listed:

- The breaking of eddies in fusion plasma by sheared $E_r \times B$ flow has been observed for the first time.
- The shearing effects on eddies depends on the coherence length of the eddy

structure, namely, the poloidal and radial correlation lengths $\omega_s \propto l_{cr} l_{c\theta}^{-1}$.

- The magnitude of the flow shearing rate plays a key role for the eddy breaking and needs to be larger than some lower limit.
- In one shot, both ”tilt only” and ”tilt and split” events can be seen depending on poloidal and radial extensions of eddies.

7
Turbulence-flow interaction in biasing-induced plasmas

The formation of the high energy confinement state (H-mode) is attributed to the spontaneous development of the mean negative edge radial electric field E_r [40, 100] and corresponding mean $E_r \times B$ flow. The causal relationship between the edge $E_r \times B$ flow layer and H-mode has been shown, for instance, in CCT, TEXTOR, CASTOR, T-10 and ISTTOK tokamaks [17, 101, 102], where the edge flow was generated externally using biasing electrodes. Similar externally driven improved confinement has also been obtained in other machines [8, 103]. The radial decorrelation, or reduction of the radial size of turbulent eddies by $E_r \times B$ flow shear is one possible mechanism by which turbulent transport might be suppressed. This mechanism has been discussed in detail in chapter 6.

Except of mean $E_r \times B$ flows, the suppression of turbulence can occur by zonal flows. In contrast to mean flows, zonal flows are poloidally and toroidally symmetric modes with very low, but finite, frequencies. The suppression of turbulence and concomitant anomalous transport by zonal flows has been clearly reported in some laboratory experiments [104]. Recently, several experimental results further indicated that the zonal flows and associated E_r oscillations play a crucial role in triggering the transition to H-mode [24, 105, 106]. In this chapter we present the detailed experimental observation on the mechanisms behind the generation of zonal flows and then the role which zonal flows play in the transition to an improved confinement.

The physical mechanisms behind the turbulence-flow interaction are addressed in Sec. 7.1. The Reynolds stress and its capability to drive zonal flows across a transition to improved confinement have been systematically studied in the biasing H-mode experiment at TEXTOR. These results are discussed in Sec. 7.2. In the end, the entire physical picture is briefly reviewed in Sec. 7.3.

7.1 Turbulence-flow interaction

At first glance, it may seem intuitively that there is no interaction between low frequency zonal flows and fluctuating turbulent flows. It is indeed difficult to imagine how fast, random and small scale turbulent flows can provide the energy supply to slowly-oscillating large scale flows. In this section we will show by the example of neutral fluid that turbulent motion indeed can lead to the interaction between turbulence and mean or slowly-oscillating flows.

Let us decompose the velocity of the fluid flow $\upsilon(x,t)$ into its mean value $\bar{\upsilon}(x,t)$ and the fluctuation $\tilde{\upsilon}(x,t)$

$$\upsilon(x,t) = \bar{\upsilon}(x,t) + \tilde{\upsilon}(x,t). \tag{7.1}$$

This is referred to as the *Reynolds decomposition*. Here, the mean value refers to the time average over a finite time interval. Therefore, $\bar{\upsilon}(x,t)$ is also a function of time, although a much slower varying function than $\tilde{\upsilon}(x,t)$. Further, the *Navier-Stokes equation*, describing the momentum conservation of fluid substances, is the following:

$$\rho\frac{d\upsilon}{dt} = -\nabla p + \eta\nabla^2\upsilon, \tag{7.2}$$

where η is the coefficient of dynamic viscosity (as opposed to turbulent viscosity), ρ is the mass density, p is the pressure. Let's continue the discussion only for cylindrical geometry (in terms of a radial and poloidal directions r,θ), provided that everything is homogeneous in the longitudinal direction z. Actually, this is similar to a turbulence in magnetised plasma where rapid streaming of the highly mobile electrons along magnetic field lines smoothes fluctuations along the field and thus restricts significant variations to the $r-\theta$ plane. We look at forces which are responsible for the mean acceleration of the poloidal flow υ_θ in the turbulent fluid. Meanwhile, we consider only the hypothetical case of an ideal fluid, the viscosity coefficient of which is equal to zero $\eta = 0$

$$\rho\frac{d\upsilon_\theta}{dt} = -\frac{1}{r}\frac{\partial p}{\partial\theta}. \tag{7.3}$$

Taking the mean of Eq. (7.3) gives

$$\rho\langle\frac{d\upsilon_\theta}{dt}\rangle = -\langle\frac{1}{r}\frac{\partial p}{\partial\theta}\rangle. \tag{7.4}$$

It implies that the mean acceleration of an element of the fluid can be driven only by the mean pressure gradient $\langle \frac{1}{r}\frac{\partial p}{\partial \theta}\rangle$. Taking into account the Reynolds decomposition and the rule that the differentiation commutes with the operation of ensemble averaging [107, p. 542]

$$\overline{\frac{\partial v_\theta}{\partial t}} = \frac{\partial \bar{v}_\theta}{\partial t}, \tag{7.5}$$

the substantial derivative can be rewritten in the form [108, p. 84]

$$\langle \frac{dv_\theta}{dt} \rangle = \frac{\partial \bar{v}_\theta}{\partial t} + \bar{v}_r \frac{\partial \bar{v}_\theta}{\partial r} + \bar{v}_\theta \frac{1}{r}\frac{\partial \bar{v}_\theta}{\partial \theta} + \frac{\partial \langle \tilde{v}_r \tilde{v}_\theta \rangle}{\partial r} + \frac{1}{r}\frac{\partial \langle \tilde{v}_\theta \tilde{v}_\theta \rangle}{\partial \theta}. \tag{7.6}$$

In the cylindrical geometry, there are no reasons for the poloidal assymetry of the mean poloidal flow. Therefore, we can assume that the term $\bar{v}_\theta \frac{1}{r}\frac{\partial \bar{v}_\theta}{\partial \theta}$ is equal to zero. For the fluid in the cylindrical tube there is no net radial transport so that $\bar{v}_r \frac{\partial \bar{v}_\theta}{\partial r} = 0$. The last term on the right hand side is associated with the poloidal pressure gradient and, in principle, can be mixed with the right hand side of Eq. (7.3). Taking into account these comments, equation (7.6) can be rewritten

$$\langle \frac{dv_\theta}{dt} \rangle = \frac{\partial \bar{v}_\theta}{\partial t} + \frac{\partial \langle \tilde{v}_r \tilde{v}_\theta \rangle}{\partial r}. \tag{7.7}$$

The velocity covariance $\langle \tilde{v}_r \tilde{v}_\theta \rangle$ is called the *Reynolds stress*. ~~Evidently, the mean of the acceleration of the flow~~ $\cancel{\langle \frac{dv_\theta}{dt} \rangle}$ ~~does not equal to the acceleration of the mean flow~~ $\cancel{\frac{\partial \bar{v}_\theta}{\partial t}}$~~.~~

Now, let us assume that the mean pressure gradient is very small so that there is only minor mean acceleration of an element of fluid

$$\langle \frac{dv_\theta}{dt} \rangle = 0 \Longrightarrow \frac{\partial \bar{v}_\theta}{\partial t} = -\frac{\partial \langle \tilde{v}_r \tilde{v}_\theta \rangle}{\partial r}. \tag{7.8}$$

The last equation means that the acceleration of the mean flow still can happen on ~~the~~ account of the momentum transfer by the fluctuating velocity field [109, pp. 34-42], even though the mean momentum of turbulent velocity fluctuations is zero $\bar{\tilde{v}}_\theta \equiv 0$.

It is the convective part of the substantial derivative which is responsible for the transport of the poloidal momentum in radial direction. This derivative describes the transport of a physical quantity in the velocity field. The Reynolds stress term $\partial \langle \tilde{v}_r \tilde{v}_\theta \rangle / \partial r$ in the form as it appears in Eq. (7.8) implies that only stretched vortices have the effect on the mean velocity field [108, p. 89]. Indeed, the existence of the Reynold stress requires that the velocity fluctuations $\tilde{v}_\theta$ and $\tilde{v}_r$ be correlated. In the context of turbulent motion, the turbulent eddies that are most effective in the production of the Reynolds stress are vortices whose correlation between $\tilde{v}_\theta$ and $\tilde{v}_r$ is substantial. The circular eddies produce negligible net correlation (zero Reynolds stress) because all directions in turbulent velocity fluctuations are equivalent. On the other hand, the Reynolds stress produced by stretched vortices is finite [22, 110].

For turbulence in fusion plasma, the generation of a sheared flow from turbulence has been proposed by Diamond and Kim [22, 23, 111] by considering the azimuthal momentum balance equation:

$$\frac{\partial\langle v_\theta\rangle}{\partial t} = -\frac{\partial\langle\tilde{v}_r\tilde{v}_\theta\rangle}{\partial r} - \mu\langle v_\theta\rangle. \tag{7.9}$$

The first term on the right-hand side represents the turbulent Reynolds stress whereas the second term describes the damping of poloidal flow, where μ is the damping rate of the flow (note that this is not a viscous damping effect). The balance between driving and damping forces determines the level of flows.

This mechanism can be interpreted within the framework of mode coupling by considering the spatial Fourier transform of Eq. 7.9, as discussed in Ref. 112.

$$\frac{\partial|v_\theta(k)|^2}{\partial t} \underbrace{- 2k_r \sum_{\substack{k_1,k_2\\ k=k_1+k_2}} Im[v_r(k_1)v_\theta(k_2)v_\theta^*(k)]}_{\text{Three-wave interaction}} = -\mu|v_\theta(k)|^2. \tag{7.10}$$

The second term on the left-hand side is the power transferred between the large-scale shear flow and small-scale turbulent fluctuations due to nonlinear three-wave interactions. This interaction should be visible in the real part of the bispectrum. This suggests the use of the bicoherence analysis as a technique to evaluate the strength of three wave couplings. If shear flow is driven by three-wave interactions, then an increase in the sheared flow amplitude should be accompanied by an increase in either the bicoherence and/or by an increase in the absolute value of Reynolds stress.

7.1.1 Vortex stretching and Reynolds stress production in hot fusion plasmas

The model of Reynolds stress production via the stretching of turbulent vortices could also be interpreted as a symmetry breaking of the $k_r - k_\theta$ spectrum of turbulent eddies [25, 75]. The experimental evidence of this phenomenon is one important step forward towards our understanding of turbulence in fusion plasma. This section presents the direct experimental visualization of the vortex stretching and concomitant Reynolds stress production as obtained using the 2D GPI measurements.

In this experiment, turbulent vortices have been stretched in the mean $E_r \times B$ flow, externally induced by means of a graphite biasing electrode inserted at $r \approx 43\ cm$. The positive bias voltage $V_{bias} = 60\ V$ was applied between the electrode and the toroidal belt limiter in order to induce the poloidal flow in the plasma edge. The only weak flow has been induced in order to ensure effective stretching of vortices but not breaking them apart. This process is shown in Fig. 7.1. The flow is qualitatively indicated by dark green arrows at the bottom of each frame. Figures 7.1(a)-(l) display the set of GPI frames showing the gradual strain of turbulent vortex along the direction indicated by the black arrow. The aspect ratio of the given eddy $a = l_{c\theta}/l_{cr}$, where $l_{c\theta}$ and l_{cr} are poloidal and radial correlation lengths, gradually rises from $a \approx 1$ in the initial stage in Fig. 7.1(a) to $a \approx 2.5$ in the final stage in Fig. 7.1(l). This result clearly shows that eddy stretching in the externally induced $E_r \times B$ flow shear indeed takes the place.

Now, as soon as we admitted turbulent eddy stretching, it would be reasonable to show how this process is linked to the Reynolds stress production. To that end, the optical flow approach, discussed in chapter 4, has been applied to the GPI frame sequences to reconstruct the 2D velocity vector fields $\tilde{v}_r$,$\tilde{v}_\theta$. Using the obtained velocity vector fields we can obtain the turbulence Reynolds stress $\langle\tilde{v}_r\tilde{v}_\theta\rangle$ (RS). Recall that the Reynolds stress arises from the correlation between radial and poloidal components of the turbulent velocity fluctuations [74]. Figure 7.2 shows that veloity vector field, corresponding to a stretching of vortices in the flow shear, indeed results in such kind of a correlation. Figure 7.2(a) shows a GPI frame whereas Fig. 7.2(b) shows displacement (velocity field) of this frame with respect to Fig. 7.2(c). We intentionally derive the vector field between two distant frames in Figs. 7.2(a) and (b) (frames #137 - #142) in order to make results more apparent. Figure 7.2(d) shows the velocity field corresponding to a stretching of the structure in Fig. 7.2(b) between frames #142 - #144. Obviously, the derived velocity fields in Figs. 7.2(b) and (d) show noticeable "diagonal" velocities with finite product $\tilde{v}_r\tilde{v}_\theta$. In that sense, pure "vertical" ($\tilde{v}_r = 0$) or "horizontal" ($\tilde{v}_\theta = 0$) displacements obviously do not contribute to the Reynolds stress.

One has to notice that such kind of stretching does not always take a place and general behavior is rather stochastic. However, the stretching of vortices is the main contributor to the mean product $\langle\tilde{v}_r\tilde{v}_\theta\rangle$ although this mean product is substantially less than instantaneous fluctuating values. In that context, one would like to arise the question about the physical meaning of the fluctuating stochastic part of the product $\tilde{v}_r\tilde{v}_\theta$.

7.2 The interaction among sheared flows, eddy structures, Reynolds stress and zonal flows across a transition to improved confinement

The Reynolds stress and its capability to drive poloidal flows have been systematically studied at the linear plasma device CSDX [113]. Concerning the turbulence in hot magnetised fusion plasmas, this process has been studied at the ISTTOK and TEXTOR tokamaks and TJ-IU stellarator [58, 114]. The relationship between turbulence and mean shear flows has been studied experimentally for the H-mode

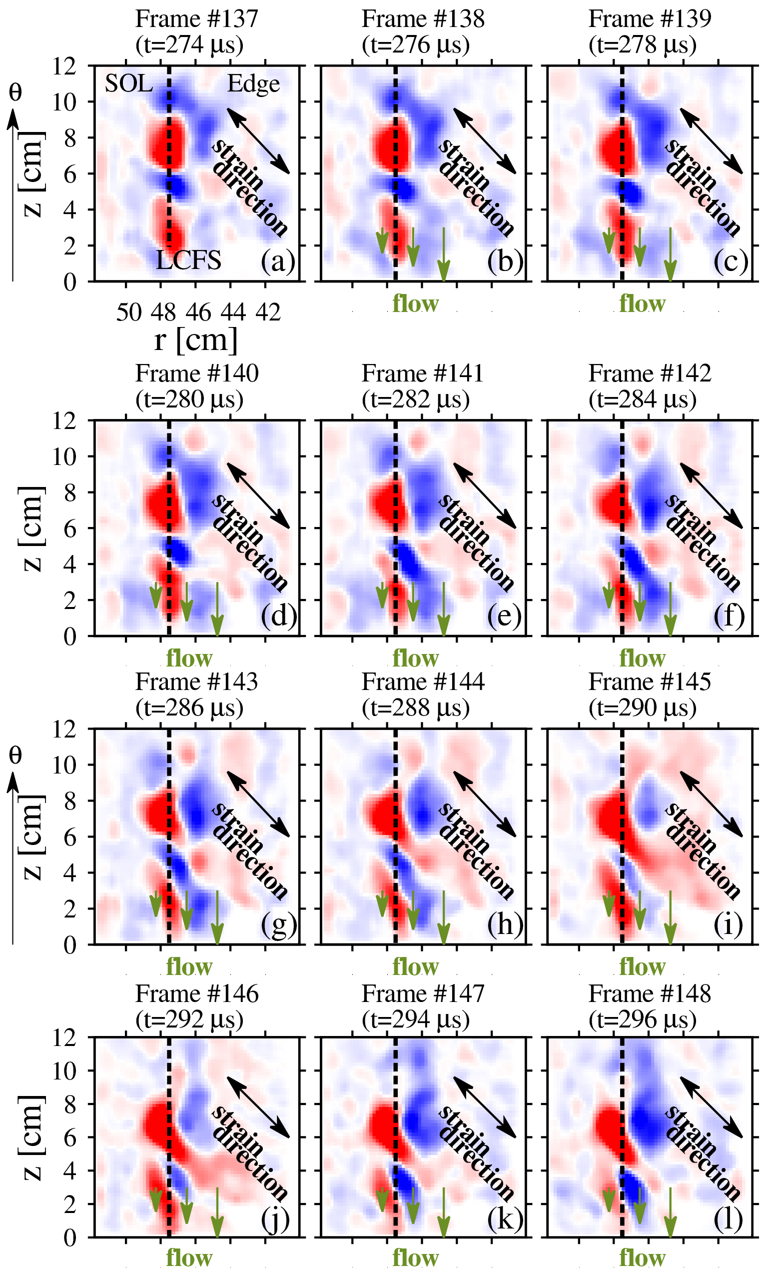

Figure 7.1: The set of GPI frames (#137 - #148) showing the stretching of turbulent structures in the externally driven weak $E_r \times B$ flow shear using the electrode positively biased to a voltage $V_{bias} = 60\ V$.

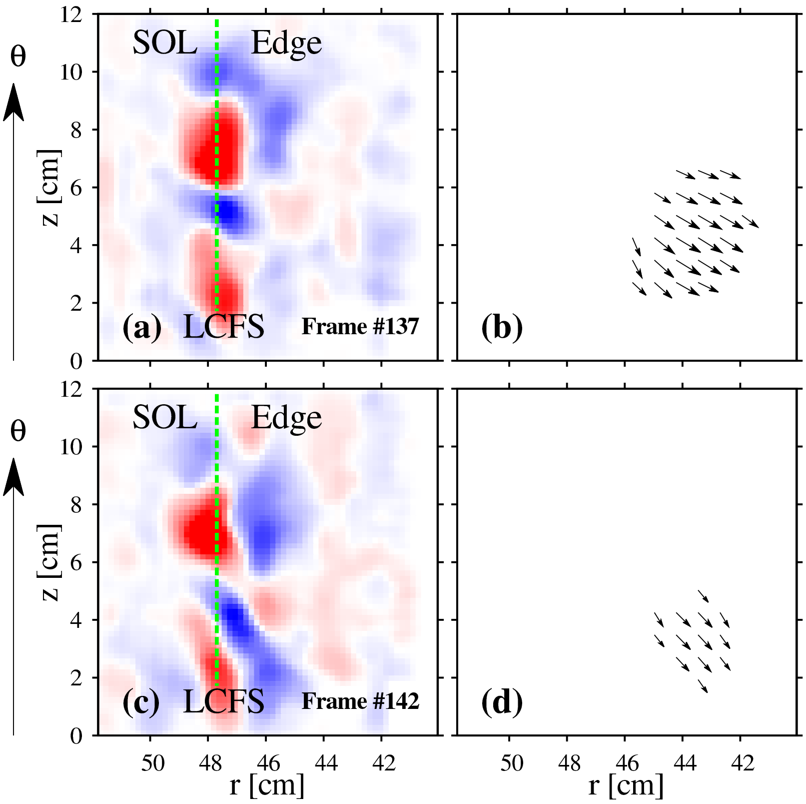

Figure 7.2: Production of the Reynolds stress by stretching of turbulent vortices in the radial versus poloidal direction. Figure (a) shows a GPI frame whereas Fig. (b) shows a stretching (velocity field) of the structure in figure (a) with respect to figure (c). Figure (d) shows the velocity field corresponding to a stretching of the structure in Fig. (b) between frames #142 - #144.

transition in the HT-7 tokamak [115].

The vortex stretching and corresponding Reynolds stress production are also suggested to be responsible for the development of zonal flow structures due to efficient energy transfer from turbulent eddies to zonal flows [25, 75, 116]. These zonal flows are toroidally uniform electrostatic potential fluctuations with zero or very low frequency of several kHz. In contrast to the mean flow, these flows have finite, though small, oscillation frequency. For more details on zonal flow properties, see chapter 8.

Some models [25, 75] show that zonal flow structures may be as important as mean flows in regulating turbulence and, therefore, play an important role in the L-H transition physics. However, hitherto a complete picture of the dynamic interaction between mean flows, zonal flows, eddy structures and the Reynolds stress across the transition to H-mode has not yet been achieved. In particular, the following steps **eddy stretching** $\mapsto$ **Reynolds stress production** $\mapsto$ **excitation of zonal flows** have not been directly observed. To test the role of zonal flows in the L-H transition, the mean $E_r \times B$ flow should be ramped up slowly across the transition to improved confinement, thereby we can gradually monitor the stretching of vortices and concomitant generation of zonal flows.

7.2.1 The biasing-triggered H-mode

To improve our understanding on the role of above-mentioned mechanisms in the L-H transition physics, we have performed dedicated experiments at TEXTOR. The $E_r \times B$ shear rate has been controlled using the externally applied bias voltage. In this experiment, we first reached H-mode at a certain bias voltage (V_{bias}) and then carefully tuned V_{bias} at different levels to explore the underlying physical processes at each biasing stage. The experiments were executed in ohmic deuterium discharges ~~in the TEXTOR tokamak~~ with plasma current I_p=250 kA, toroidal magnetic field B_T=1.6 T and 2.25 T and central line-averaged electron density $\bar{n}_e$=(1.5-2.3)$\times 10^{19}$ m^{-3}. In order to generate an edge radial electric field E_r and a $E_r \times B$ flow shear layer, a positve V_{bias} in the range from 0 to 250 V has been imposed between a graphite electrode (inserted at r$\approx$43 cm) and the toroidal belt limiter. The edge electric field was measured by fast reciprocating Langmuir probes, and the sampling rate is 500 kHz (see section 3.4 for more details on Langmuir probe technique).

Typical regimes of a biasing-triggered H-mode and related discharge waveforms are plotted in Fig. 7.3. In Fig. 7.3(a) the solid curve shows the time evolution of the bias voltage with a maximal value (V_{bM}) of 250 V. The V_{bias}, ramping almost linearly from 0 to 250 V and then holding constant for about 0.6 s and eventually decaying, was applied in the stationary discharge stage. During the ramping phase, a transition of plasma confinement to H-mode occurs at $V_{bias} \cong$130 V (see the vertical dashed line), along with an increase in the line-averaged density and a reduction in the D_α signal, as illustrated by solid curves in Fig. 7.3(b). Note that this transition threshold of V_{bias} has also been confirmed in other biasing discharges, e. g., for $V_{bM} = 150\ V$, the signals in Figs. 7.3(a) and (b) show similar transition to H-mode at time t = 2.38 s, for which the bias voltage is also around 130 V. Obviously, to unravel the L-H transition mechanisms as well as the interaction between sheared flows and turbulence properties, the ramping phase in V_{bias} before and after the transition should be the focus of our studies, i. e., one should trace the changing of related quantities at times of A, B, C, D, E during the rising period of V_{bias} (see circular points in Fig. 7.3(a)). Whereas the probe measurements can cover the entire rising period of V_{bias}, the GPI diagnostic used in this

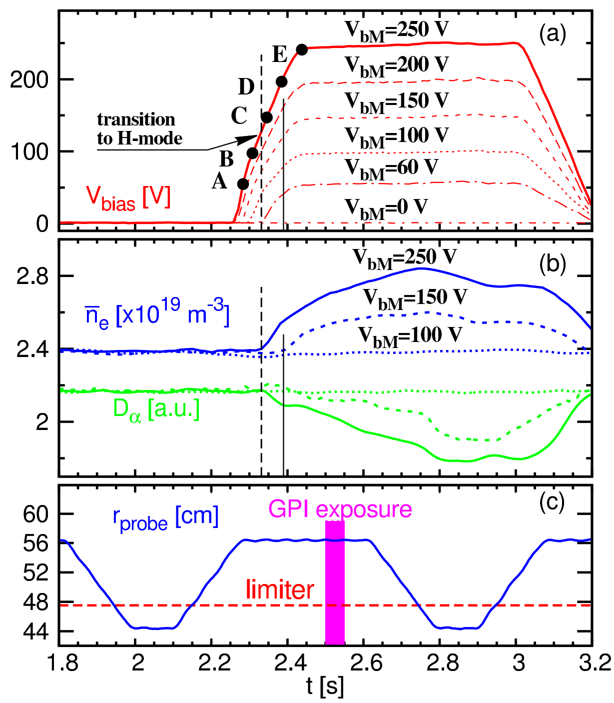

Figure 7.3: Typical waveforms of biasing H-mode discharges at TEXTOR. Time traces of (a) bias voltages V_{bias} in different V_{bM} discharges; (b) line-averaged density $\bar{n}_e$ and D_α emission on limiter in three V_{bM} shots; (c) radial position of reciprocating probes (dashed line denotes the limiter position) and the GPI exposure time window. A more scientific approach would be to make measurements in one discharge during the rising phase of V_{bias} from $0\ V$ to $250\ V$ and trace the changing of related quantities at times of A, B, C, D, E (see circular points in figure (a) which correspond to the bias voltages $0, 60, 100, 150, 200, 250\ V$). However, an exposure time of our camera ($\approx 1 - 2\ ms$) is much shorter than the duration of a rising phase of V_{bias} ($\approx 100\ ms$). Therefore, we made a step-wise increase of the flat top bias voltage V_{bM} shot by shot (red lines in figure (a)).

study can only expose about 0.6 ms in one plasma discharge because of the limitation in the frame number of the camera (300 frames/shot $\times$ 2 μs = 0.6 ms). Thus, it is impossible for the GPI to detect continuously the changing of turbulence structures from time A to E in one shot. Alternatively, we made a step-wise increase of the maximal bias voltage V_{bM} shot by shot (under the same discharge conditions) from 0 to 60, 100, 150, 200, 250 V. These V_{bM} correspond, respectively, to the V_{bias} values at the time of A, B, C, D, E, as depicted by dashed curves in Fig. 7.3(a). In such cases, we can perform both the probe and GPI measurements in the stationary phase of each V_{bM} in various biasing shots to explore the underlying physical processes at different V_{bias} stages across the transition. Figure 7.3(c)(blue line) shows the time trace of the fast probe, moving from the SOL into the plasma edge inside the last closed flux surface (LCFS). For a comparison between the phase before and during the biasing H-mode, the fast probe plunges twice in one discharge. The vertical pink colour bar shows the GPI exposure time window in the H-mode phase.

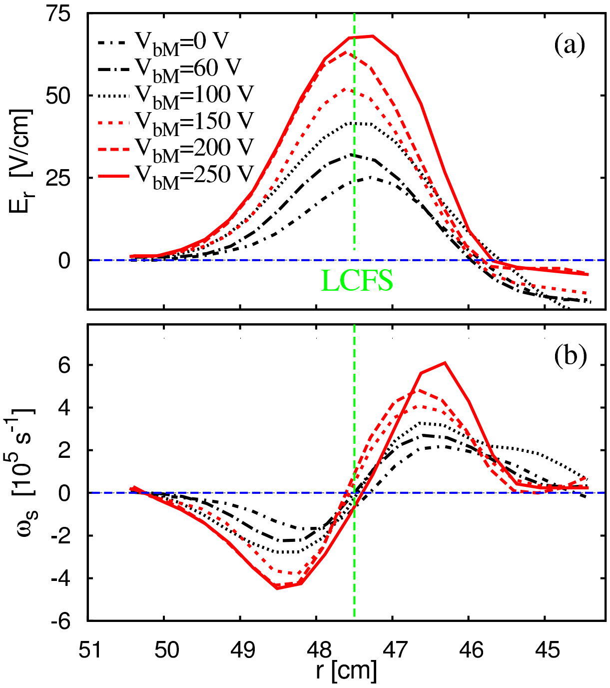

Figure 7.4: The radial dependence of (a) electric field E_r and (b) $E_r \times B$ flow shear ω_s measured by the fast reciprocating probe for the different V_{bM} shots shown in Fig. 7.3.

In all biasing discharges, the radial profiles of E_r have been deduced by probes from the plasma potential ϕ_p=ϕ_f+2.8T_e, where ϕ_f (floating potential) and T_e (electron temperature) are measured by a triple probe [62]. The results are plotted in Fig. 7.4(a). Each curve corresponds to one of the shots shown in Fig. 7.3(a) at a certain V_{bM}. Figure 7.4(b) depicts the corresponding radial profiles of $E_r \times B$ flow shear rate, $\omega_s = \frac{\partial E_r}{B \partial r}$. One can see that as the V_{bM} increases from 0 to 250 V, both edge E_r and its shear rate ω_s gradually increase nearby the LCFS, as expected.

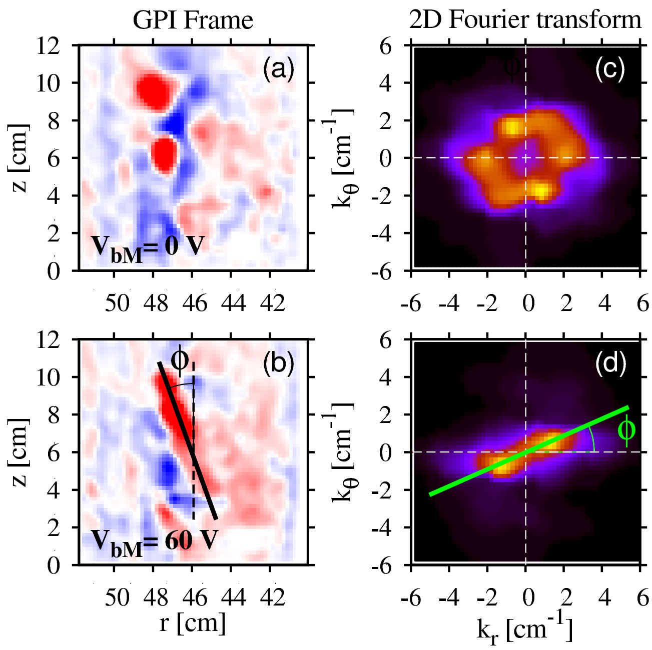

Figure 7.5: (a)-(b) GPI frames and (c)-(d) their 2D (k_r versus k_θ) wavenumber spectra measured in two V_{bM} discharges. Top panels (V_{bM}=0 V) for (a,c) and Bottom panels (V_{bM}=60 V) for (b,d).

7.2.2 Reynolds stress production and generation of zonal flows by vortex stretching

The aim of our next study is to systematically show that externally induced $E_r \times B$ flow shear stretches the structures in the same way as they are stretched in the natural $E_r \times B$ flow in ohmic plasmas. For the comparison reason - the stretching presented in Fig. 7.1 occupies only few GPI frames and, therefore, can not be considered as a systematic study. Figures 7.5(a) and (b) show the typical images of GPI measured in two different bias voltage discharges. In this study, we subtracted the time-averaged mean values from the light intensity detected at each pixel for every image, as we are interested only in turbulent behaviors. In Fig. 7.5(a) when V_{bM} = 0 the shape of turbulence eddies is close to circular, while in Fig. 7.5(b) the eddies are stretched with a tilted angle ϕ as the V_{bM} increases to 60 V. It has been found that the tilting of turbulence structures increases with the enhanced $E_r \times B$ shear rate prior to the transition to H-mode. To further characterize the shape of turbulence structures, a two-dimensional space fast fourier transformation (2D FFT) has been used. Figures 7.5(c) and (d) plot the 2D wave-number spectra (k_r versus k_θ) for the GPI images displayed in Figs. 7.5(a) and (b), respectively.

Similar to those in the images, the wavenumber spectra are quasi-symmetric and asymmetric (with preferential direction at tilting angle ϕ) in Figs. 7.5(c) and (d), respectively. The advantage of this approach is that the 2D FFT spectrum can be averaged over time and the systematic information about the shape and orientation of structures can be deduced.

To detect systematically the dynamical evolution of turbulence structures at different flow shear rates, we have applied the 2D FFT technique to analyse the variation of eddy shapes in a series of discharges (with different V_{bM}) across the transition period, as already explained in Fig. 7.3. For each V_{bM}, the bias voltage is shown at the top of each column in Fig. 7.6. Figures 7.6(a)-(f) show the contour plots of 2D wavenumber spectra of GPI data measured at different V_{bM} discharges. The spectrum is averaged over all 300 images in every shot. At zero bias voltage (Fig. 7.6(a)), the ratio of ω_s/ω_D approximately equals to 1.2 and the $k_r - k_\theta$ spectrum is roughly symmetric. When the ratio of ω_s/ω_D is enhanced up to 1.5 and 1.8 (V_{bM} = 60 V, 100 V), the shape of the spectrum gradually becomes elliptic, as seen in Figs. 7.6(b) and (c), with an orientation angle of $15^\circ - 30^\circ$ with respect to the k_r axis. The typical example of this phenomenon for $V_{bM} = 100\ V$ is shown in Fig. 7.7. The similar phenomenon has also been observed in TJ-II, NSTX and LAPD devices [8, 99]. As the V_{bM} exceeds the transition threshold (i. e. $V_{bias} \geqslant 130$ V) and further increases from 150 V to 250 V ($\omega_s/\omega_D \approx 2.5 - 3.1$), the spectrum becomes wider and meanwhile less stretched. The widening of the spectrum implies breakup of eddies at high shear rates when $\omega_s/\omega_D \geqslant 2.0$, as we observed earlier [117] (and discussed in section 6.2) in the naturally occuring $E_r \times B$ flow. The example of such a phenomenon for an externally induced flow in the discharge #116599 with $V_{bM} = 100\ V$ is shown in Fig. 7.8 (the splitting process is observed in figure (e)). Apparently, the stretching of eddies is less effective for small-size eddies once the large structures are broken into small pieces. A schematic view of the eddy structure shapes with increasing V_{bM} and ω_s is depicted at the bottom of Fig. 7.6. We have to emphasize that this is the first time that direct visualization of the eddy stretching and splitting process has been observed in a confinement device undergoing a transition to improved confinement.

Another technique suitable for the study of the morphology of turbulence structures is the wavelet-based directional analysis [118, 119]. Compared to 2D FFT, this approach can deal with individual turbulent structures instead of a whole GPI frame. In the first stage, turbulent structures in each frame were operationally defined as the regions above certain threshold level of the intensity. An example of such operation is shown in Fig. 7.9. Figure 7.9(a) shows some typical GPI frame with apparent turbulent structure on it. Figure 7.9(b) in turn displays some structure identified in figure (a) as the regions above a certain threshold level. By doing so, one can identify all structures that belong to every GPI frame. Note that the

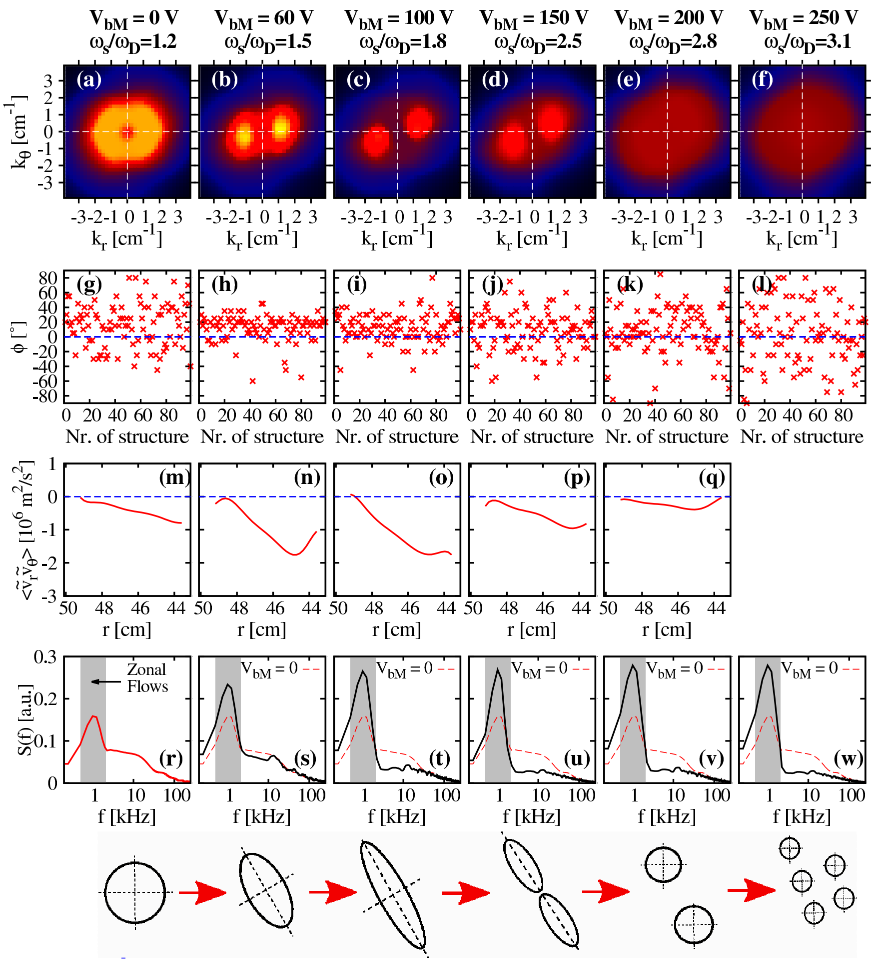

Figure 7.6: (a)-(f): Contour plots of 2D (k_r versus k_θ) time-averaged wavenumber spectra of GPI data detected in different V_{bM} shots. (g)-(l): The distribution of orientation angles for 100 randomly chosen individual turbulent structures. The x-axis denotes the individual number of structures in the database. (m)-(q): Radial profiles of the Reynolds stress measured at different V_{bM} discharges across the transition to the improved confinement. (r)-(w): The frequency spectra of floating potential fluctuations measured by Langmuir probes. The red dashed curve shows the reference spectrum for V_{bM} = 0. Bottom row: A schematic view of the shapes of eddy structures under different V_{bM}.

structure in Fig. 7.9(b) was placed in the centre of the figure because in our analysis we are not interested in the position of structures in image. A typical GPI video

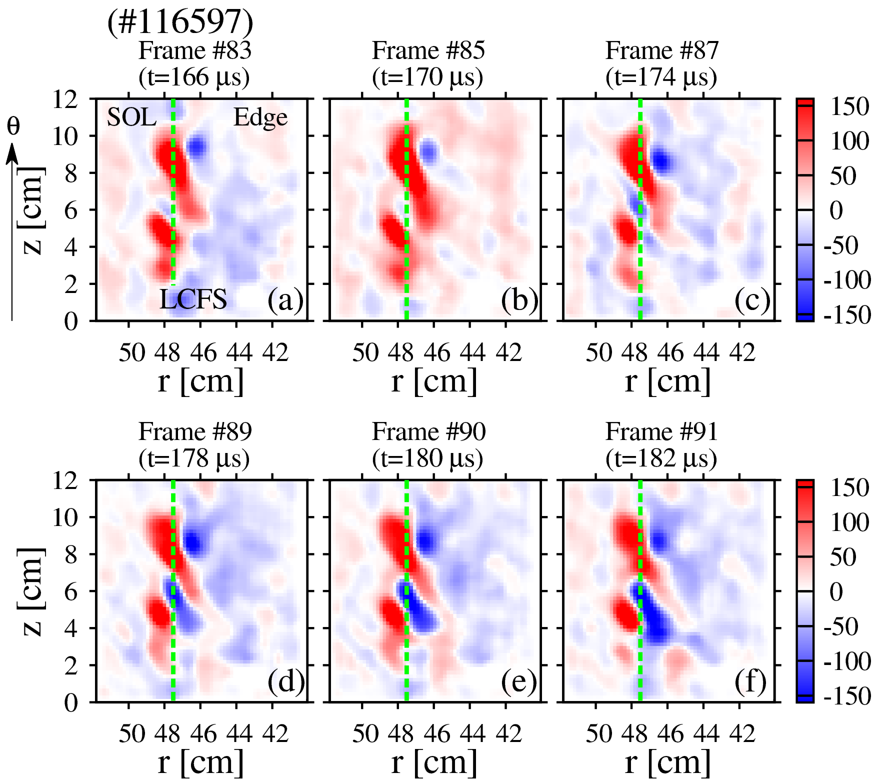

Figure 7.7: Time sequences of GPI images in the shot (#116597) with $V_{bM} = 100\ V$. This example shows a stretched structures formed in the sheared $E_r \times B$ flow, that is relatively weak in order to break structures.

contains approximately about 300-400 such kind of individual structures. Having done that, the database of 100 individual structures has been randomly selected in every V_{bM} discharge.

In the second stage, our aim is to detect the orientation angle ϕ of each individual structure. Figure 7.10(a) displays individual structure, the same as in Fig. 7.9(b). The directional analysis, based on the 2D Morlet wavelet, was applied to the structure in Fig. 7.10(a) to derive its orientation angle ϕ with respect to the vertical axis. The formula for the complex Morlet wavelet is the following:

$$\psi_{\rho,\phi}^{Morlet}(x,y) = (e^{-ik_o(xcos(\phi)+ysin(\phi))} - e^{-\frac{1}{2}k_o^2})e^{-\frac{1}{2}(x^2+y^2)}. \qquad (7.11)$$

Here, ϕ denotes the orientation angle of the wavelet and $k_o = 2\pi/\rho$ denotes its wave vector (ρ is the characteristic spatial scale of the wavelet). Example of the real part of the 2D Morlet wavelet is shown in figure 7.10(b) for the scale of

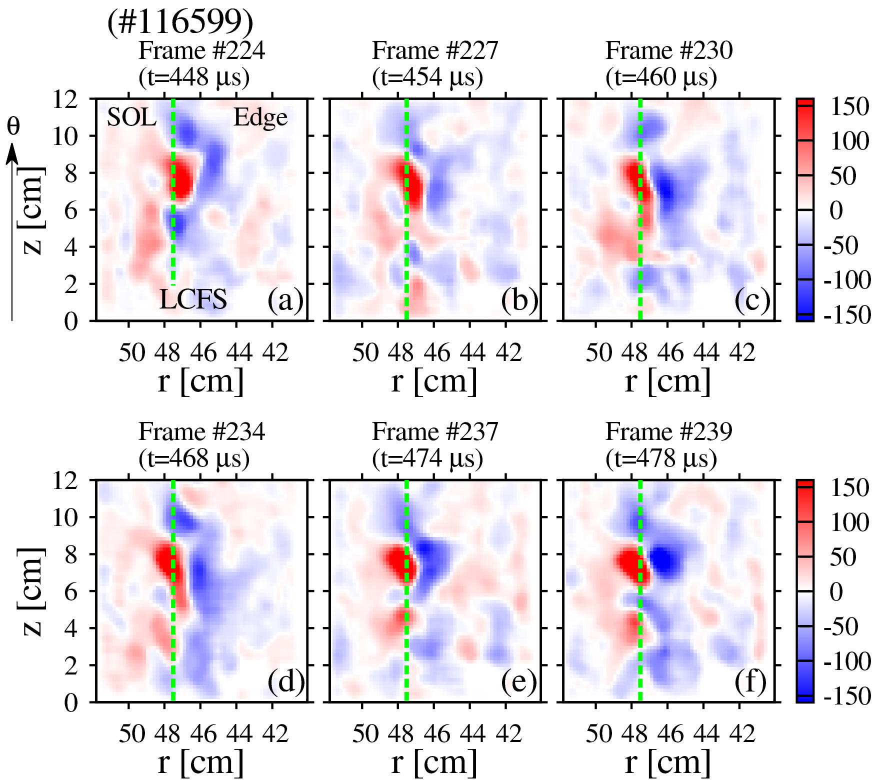

Figure 7.8: Time sequences of GPI images in the shot (#116599) with $V_{bM} = 200\ V$, showing the breaking of a turbulent structure in an externally induced $E_r \times B$ flow. The splitting processes is observed in Frame #237 (figure (e)).

$\rho = 0.8\ cm$ and orientation angle $\phi \approx 30^o$. The spatial convolution of a turbulent structure with the 2D Morlet wavelet

$$S_{\rho,\phi}(x,y) = \langle \psi^{Morlet}_{\rho,\phi}(x,y) \mid I^{turb}(x,y) \rangle \tag{7.12}$$

gives the convolution surface $S_{\rho,\phi}(x,y)$, which contains the information about the degree of similarity between the wavelet and detected structure. This is similar to a cross-correlation between two functions.

In the first step of our analysis, we put all defined structures in the centre of the frame, as for instance the structure in Fig. 7.10(a). Our interest is the maximum of $S_{\rho,\phi}(x,y)$ which contains the information about similarity between $\psi^{Morlet}_{\rho,\phi}(x,y)$ and $I^{turb}(x,y)$. Performing such a convolution for different orientations ($\phi \in [-90^o : 90^o]$ and scales $\rho \in [0\ cm : 3\ cm]$) and always taking the maximum of $S_{\rho,\phi}(x,y)$, one can obtain the 2D response surface (in ϕ-ρ coordinates) of the

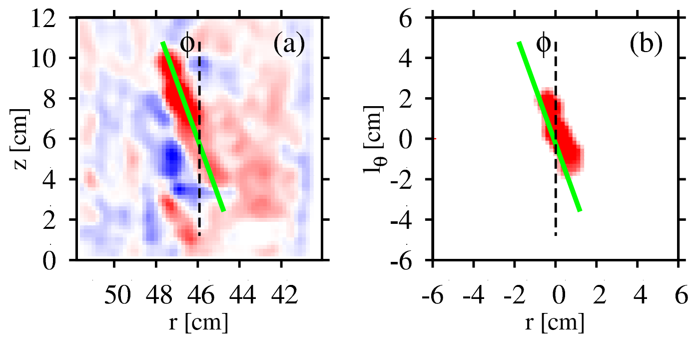

Figure 7.9: (a): The typical GPI frame with some apparent stretched turbulent structure. (b): The turbulent structure from (a) operationally defined as the regions above certain threshold level of the intensity.

given turbulent structure. This surface has a maximum where the scale and angle ϕ of the wavelet are close to these values corresponding the turbulent structure under analysis. The response surface for the structure in Fig. 7.10(a) is shown in Fig. 7.10(c). From this surface, an orientation angle ϕ of the structure can be inferred. This surface is peaked around the point of $\phi \approx 35^o$ and $\rho \approx 1\ cm$, which coincides with these values for the structure in Fig. 7.10(a).

Such kind of a directional analysis has been applied to every of 100 individual structures from the database of each GPI video. The essential feature of such a directional analysis is that it needs essential elongation for the structure to be analysed. For instance, this analysis applied to pure circular isotropic structure gives very sporadic orientation angles, simply because a circle does not have an orientation.

The second row of Fig. 7.6 displays the individual angle ϕ for all selected structures at different V_{bM}. At the zero bias voltage (Fig. 7.6(g)), the angular distribution is rather broad (from -40° to 80°), in accordance with the isotropic shape shown in Fig. 7.5(a) or Fig. 7.6(a). As the V_{bM} increases up to 100 V, the structures become stretched and uniformly aligned with an angle $\phi \approx 20°$ along a certain preferential direction, in agreement with the shape shown in Fig. 7.5(b) or Figs. 7.6(b) and (c). When the V_{bM} further increases from 150 V to 250 V, the angular distribution gradually changes back to the initial isotropic type without any preferential direction after the breaking of eddies, consistent with the wavenumber spectra shown in Figs. 7.6(d)-(f).

As the fact that the vortex stretching and concomitant symmetry breaking of $k_r - k_\theta$ spectrum are linked to the Reynold stress production, it is interesting to investigate the change in Reynold stress across the transition phase. To this end, an optical flow approach, discussed in detail in chapter 4, has been applied to the measured GPI frame sequences to reconstruct the 2D (radial *versus* poloidal) fluc-

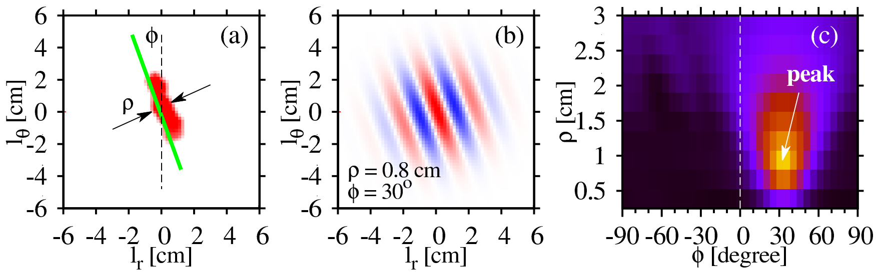

Figure 7.10: (a): The operationally defined turbulent structure with an inclination angle of $\phi \approx 30^o$ with respect to the vertical line. (b): The real part of the 2D Morlet wavelet with a scale of $\rho = 0.8\ cm$ and orientation angle $\phi \approx 30^o$. (c): The response surface of the structure in Fig. (a). The peak of this surface at $\phi \approx 35^o$ and $\rho \approx 1\ cm$ indicates the scale and orientation angle of the structure.

tuating velocity vector fields, $\tilde{v}_r$ and $\tilde{v}_\theta$, by which we can compute the turbulent Reynold stress $\langle \tilde{v}_r \tilde{v}_\theta \rangle$ (RS). Figures 7.6(m)-(q) show radial profiles of the RS derived in different V_{bM} shots from 0 to 200 V. For V_{bM}=250 V, the reconstruction of velocity fields is unreliable because of very poor signal to noise ratio. It can be seen that at zero V_{bM}, the RS and its radial gradient are both small. When the V_{bM} is increased to 60 V and 100 V, the RS and its gradient in Figs. 7.6(n) and (o) becomes much larger, in accordance with the stretched shape of eddies, as illustrated in Fig. 7.6. Here, we directly show that the vortex stretching and symmetry breaking of turbulent eddies is indeed linked to the Reynolds stress production. Similar results have been reported on the base of 2D GPI measurements performed in NSTX [120]. With further increasing of V_{bM} from 150 to 200 V, the RS gradually diminishes due to recovery of the symmetry of eddy structures after splitting.

*—**Production of zonal flows***

The fourth row in Fig. 7.6 plots the change in the fluctuation level with increasing shear rates in various V_{bM} discharges. Shown in Figs. 7.6(r)-(w) are the frequency spectra (S(f)) of floating potential fluctuations measured by Langmuir probes at $r \approx 47$ cm in the shear layer. When V_{bM} = 0 V, the frequency spectra display small coherent modes around 1.3 kHz, associated with low frequency zonal flow (LFZF) [61]. The grey colour bar indicates the power localisation of the zonal flow, as shown by the black arrow in Fig. 7.6(r).

As the flow shear increases with enhanced V_{bM}, the fluctuation power at high frequencies is generally reduced in comparison with the initial one, as marked by the red dashed curve as a reference. However, for the LFZF components, their fluctuation power is strongly amplified with the increase of V_{bM} from 0 to 100 V and then saturated at higher V_{bM} values after the transition to H-mode. Taking into account the results of Figs. 7.6(m)-(o) we can say that the radial derivative of the Reynolds stress term could be relevant to drive the production of zonal flows via nonlinear energy transfer from ambient turbulence, supporting the model of turbulence-driven zonal flow via the Reynolds stress [111] discussed in the beginning of this chapter.

7.2.3 The nonlinear energy transfer from the ambient turbulence into the zonal flow across the transition to H-mode

For a deep understanding of the H-mode transition physics, the nonlinear energy transfer processes between the ambient turbulence (AT) and the amplified LFZF prior to the transition should be further inspected. For this purpose, a simple model of the power balance between small-scale AT and large-scale zonal flows [121] has been applied:

$$\frac{\partial \tilde{v}_{turb}^2}{\partial t} = \gamma_{eff}\tilde{v}_{turb}^2 - \gamma_{decor}\tilde{v}_{turb}^2 + \frac{\partial\langle\tilde{v}_r\tilde{v}_\theta\rangle}{\partial r}V_{ZF} \tag{7.13}$$

$$\frac{\partial V_{ZF}^2}{\partial t} = -\frac{\partial\langle\tilde{v}_r\tilde{v}_\theta\rangle}{\partial r}V_{ZF} - \mu_{ZF}V_{ZF}^2 \tag{7.14}$$

where $\tilde{v}_{turb}^2$ and V_{ZF}^2 represent, respectively, the turbulent and zonal flow energies, γ_{eff} and γ_{decor} are the turbulence energy input rate (driven by ∇n,∇T,...) and decorrelation rate towards small-scale AT, respectively, and μ_{ZF} is the damping rate of zonal flows. This model essentially reveals a predator-prey process for the energy transfer between the AT and the LFZF.

Figure 7.11(a) plots time traces of the poloidally $E_r \times B$ velocity ($V_{E\times B}$) and the AT energy ($\tilde{v}_{turb}^2$ computed in a frequency range of 20-200 kHz), both measured by probes at r=46.5 cm in a biasing shot with V_{bM}=150 V. The lower bound for the AT frequency range was chosen to not interfere with the frequency range of zonal flows (LFZFs and GAMs), which cover the range from 0 to 20 kHz. The upper bound was chosen to capture a sufficient amount of the AT power. Note, that it is unnecessary to expand the AT range up to the Nyquist frequency (250 kHz) because the relative contribution of very high frequency modes (in the range above 150 kHz) is negligibly small.

The oscillation in $V_{E\times B}$ signal reflects the zonal flow (V_{ZF}) oscillation at $f = 1.3\ kHz$, which is consistent with $S(f)$ shown in Figs. 7.6(r-w). The $\tilde{v}_{turb}^2$ also varies at the same frequency and correlates well with the V_{ZF} variations. The small phase delay ($\approx \pi/2$) in between corresponds to a limit cycle oscillation in the predator-prey regime, as reported in other machines [105,106]. Equation (7.13) indicates that the growth/drop of the AT energy depends on the competition between *net effective power input* $\gamma_{net} \cdot \tilde{v}_{turb}^2$ ($\gamma_{net} = \gamma_{eff} - \gamma_{decor}$) and *nonlinear power transfer* $P_{ZF} = \frac{\partial\langle\tilde{v}_r\tilde{v}_\theta\rangle}{\partial r} \cdot V_{ZF}$, namely, the *effective power transfer rate*,

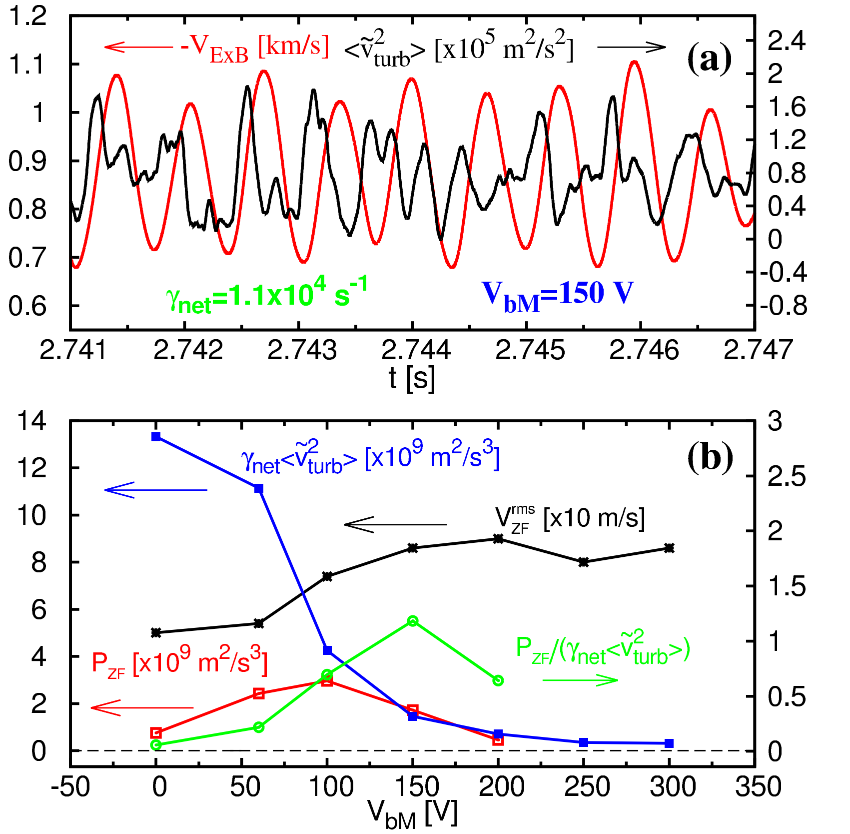

Figure 7.11: (a) Time traces of the turbulence energy and the $V_{E\times B}$ velocity measured by probes at $r = 46.5$ cm with $V_{bM} = 150$ V. (b) The energy transfer parameters in the power balance model as a function of V_{bM} voltages.

$P_{ZF}/(\gamma_{net}\langle\tilde{v}^2_{turb}\rangle)$. According to Eq. (7.13), the *net effective power input* can be deduced from the time derivative of the AT energy ($\frac{\partial \tilde{v}^2_{turb}}{\partial t}$), when $V_{ZF} = 0$. Assuming that this net power input changes little with or w/o V_{ZF} [121], we estimated from Fig. 7.11(a) an averaged value of $\gamma_{net} \cdot \tilde{v}^2_{turb} \approx 1.45 \times 10^9\ m^2/s^3$ and $\gamma_{net} = 1.1 \cdot 10^4\ s^{-1}$ from the raising phases of $\tilde{v}^2_{turb}$ signal at the time of minimal $V_{E\times B}(V_{ZF} \cong 0)$. Meanwhile we calculated $P_{ZF} = 1.72 \times 10^9\ m^2/s^3$ from the Reynolds stress gradient at $r \approx 46.5\ cm$ and the rms level of V_{ZF} signal (V^{rms}_{ZF}). Hence, we obtained the *effective power transfer rate*, $P_{ZF}/(\gamma_{net} \cdot \langle\tilde{v}^2_{turb}\rangle) \approx 1.18$ in case of $V_{bM} = 150$ V. Using a similar way we computed these relevant quantities in different biasing scenarios. The results are depicted in Fig. 7.11(b), where the V^{rms}_{ZF}, P_{ZF}, $\gamma_{net} \cdot \tilde{v}^2_{turb}$ and $P_{ZF}/(\gamma_{net} \cdot \langle\tilde{v}^2_{turb}\rangle)$ are plotted as a function of V_{bM}. With increasing V_{bM}, $\gamma_{net} \cdot \tilde{v}^2_{turb}$ decreases rapidly while V^{rms}_{ZF} gradually increases and saturates after $V_{bM} = 150$ V. Interestingly, because of maximal eddy tilting and the resultant RS gradient, the P_{ZF} shows a local maximum at $V_{bM} = 100$ V and the *effective power transfer rate* reaches to unity at $V_{bM} = 150$ V. Note that the transition to H-mode takes place at $V_{bias} = 130$ V, as illustrated in Fig. 7.3. These results clearly demonstrate the key role that energy transfer plays in triggering a transition to improved confinement.

The flow shear gives the dynamical influence on turbulence structures, which results in generation of Reynolds stress and zonal flows and eventually suppress background fluctuations via nonlinear energy transfer. The latter may therefore trigger a transition to the H-mode.

7.3 Summary

In conclusion, dedicated experiments have been conducted at TEXTOR in biasing-induced H-mode experiments to survey underlying physics across the transition to an improved confinement by using Langmuir probe and GPI diagnostics. These results present the first evidence of the eddy stretching and splitting process in a confinement device and the intimate interaction between sheared flows, eddy structures, Reynolds stress, zonal flows and ambient fluctuations during the transition to an improved confinement. The flow shear gives the dynamical influence on turbulence structures, which results in the generation of the Reynolds stress and zonal flows and eventually suppresses background fluctuations. Based on our observations, we got the entire physical picture as follows: at the initial stage, with increasing flow shear rates the eddies are gradually stretched and the Reynolds stress magnitude increases as well due to the symmetry breaking mechanism. At the same time, the zonal flows are excited by enhanced RS and concomitantly extract energy from ambient turbulence through the nonlinear energy transfer. As the power transfer rate approaches unity, the plasma confinement is improved and transits into the H-mode phase. When the flow shear rate further increases during the H-mode, the eddies split into small pieces in symmetric shape and hence the RS gradually diminishes. However, the zonal flows remain robust and background fluctuation amplitudes are largely suppressed.

8

Experimental studies of GAM zonal flows at the TEXTOR tokamak

It has already been mentioned in the previous chapter that the radial gradient of the Reynolds stress could drive not only mean "zero-frequency" flows but also zonal flows. In contrast to the previous chapter, where we discussed the low-frequency zonal flow branch, this chapter is dedicated to GAM zonal flows, the origin of which was already discussed in detail in section 1.1.1. It was also mentioned that GAM zonal flows play an important role in the regulation of turbulence and turbulent transport. Some experimental results on this issue can be found in Ref. 27,122.

The GAM zonal flows (as well as low frequency zonal flows) are the reasons for the oscillatory L-H transition phase (so called dithering or I-phase), observed, for instance, on ASDEX Upgrade [24], EAST [34] and W7-AS [35] machines. The theory in Ref. 25 states that these flows substantially lower the L-H transition power threshold, as compared to the situation when zonal flows are absent. For these reasons, in the past fifteen years, these flows have been the subject of intensive studies on many machines around the globe [26–31].

At TEXTOR, GAM zonal flows have been initially identified by correlation reflectometry [41] as density fluctuations at the top of the vacuum vessel. Further characterisation of GAM zonal flows at TEXTOR and their radial propagation has been reported in Refs. 42,43. This chapter provides a comprehensive experimental analysis of GAM zonal flows and the role they play in the turbulent transport.

In section 8.1, the manifestation of GAM zonal flows in the frequency spectrum of fluctuations is discussed. Section 8.2 presents GAM zonal flows as poloidally and toroidally uniform structures. The characterisation of the role of GAM zonal flows in turbulent transport is addressed in section 8.3. The modulation of ambient turbulence by GAM zonal flows and their subsequent nonlinear interaction are discussed in sections 8.4 and 8.5, respectively. Finally, the main experimental results are summarised in section 8.6.

8.1 Spectral analysis

The first step in characterizing GAM zonal flows is to demonstrate their existence in the frequency spectrum of fluctuations. Such results are presented in Fig. 8.1. The frequency spectra of a floating potential $\tilde{\phi}_{fl}$ and ion saturation current $\tilde{I}_{sat}$ are shown for comparison. Each spectrum is averaged over 60 samples to reduce an uncertainty of the results. Each sample covers a time window of 1.6 ms (frequency resolution is 0.62 kHz). Prior to the FFT transformation, the subtraction of the mean value from each data sample and multiplication by a Henning window function had been carried out. Measurements have been made at the location of $\approx$ 2 cm inside the last closed flux surface (LCFS). Two types of fluctuations could be identified in the auto-power spectra of $\tilde{\phi}_{fl}$ fluctuations (black line). The significant peak around 8 kHz (indicated by the grey colour area) is associated with the GAM zonal flow fluctuations. Another peak, though much weaker, in the frequency range of 20-80 kHz (also indicated by the grey colour area) is associated with the quasi-coherent (QC) mode.

The nature of QC fluctuations in the edge of TEXTOR have never been studied systematically. However, many experimental results from different machines show that these QC fluctuations have drift-wave-like properties, i.e., in-phase density and potential fluctuations (see for instance Ref. [123] where the QC mode in Alcator C-Mod is unambiguously identified as a drift wave).

It is noticeable from Fig. 8.1 that GAM fluctuations are apparent ~~only~~ in the power spectrum of the floating potential, whereas the spectral peak of GAMs in the frequency spectrum of $\tilde{I}_{sat}$ is ambiguous. This result is not surprising taking into account the following theoretical relation [27]:

$$\tilde{n}_e(f_{GAM}) \propto sin(\theta)\tilde{\phi}_p(f_{GAM}), \tag{8.1}$$

where $\tilde{\phi}_p(f_{GAM})$ is the fluctuations of plasma potential associated with GAM zonal flows. This relation implies that fluctuations of electron density driven by GAMs, as measured in the equatorial plane of the torus ($\theta \approx 0$), are negligibly small. In other words, optimal positions for measuring the GAM density fluctuations are either at the top or at the bottom of the vacuum vessel ($\theta \pm 90^o$). As an aside it should be mentioned that QC fluctuations are observed also in the spectrum of $\tilde{I}_{sat}$. This is because drift waves have both density and potential components following the Boltzmann relation.

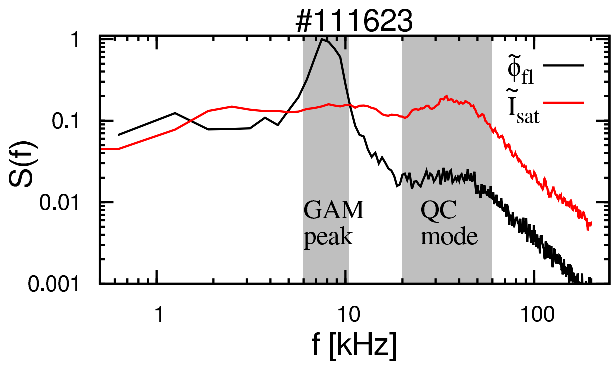

Figure 8.1: The power spectrum of floating potential fluctuations. The grey colour area at the frequency of 8 kHz indicates the power localisation of GAMs zonal flow oscillations. Another grey colour area in the frequency range of 20-80 kHz is associated with the QC mode.

In the next step, it would be interesting to compare the experimentally measured frequency of GAM with the theoretically predicted value. The theoretical prediction of the GAM frequency [33, 39, 124] is the following:

$$f_{GAM} = \sqrt{2} \cdot C_s / 2\pi R, \tag{8.2}$$

where $C_s = \sqrt{(T_e + \gamma_i \cdot T_i)/M_i}$ is the ion sound speed, R is the major radius, γ_i is the ion adiabatic index and T_i is the ion temperature. It is assumed for simplicity that $\gamma_i \cdot T_i \approx T_e$. The experimental value of the GAM frequency $f_{GAM}^{exp} \approx 7\ kHz$ in Fig. 8.1 is approximately consistent with the theoretical predictions of Eq. (8.2), i.e., $f_{GAM}^{theory} \approx 7\ kHz$ for edge $T_e = 30\ eV$ in deuterium plasmas.

At TEXTOR, in different shots with different plasma conditions, the peak frequency of GAM zonal flow fluctuations varies within the range of 5-12 kHz. Therefore, it would be interesting to make a more systematic comparison of theoretical and experimental GAM frequencies. This type of study has been undertaken where we compared the frequency of the GAM peak in the power spectrum of $\tilde{\phi}_{fl}$ with theoretical predictions of Eq. (8.2). The comparison has been done for different ohmic shots with different edge electron temperatures. The electron temperature was measured by a triple probe. Results are presented in Fig. 8.2. It is visible that theoretical and experimental estimates agree reasonably well. This ~~relative~~ consistency provides some evidence that model projections on the GAM frequency are relatively reliable and of practical importance.

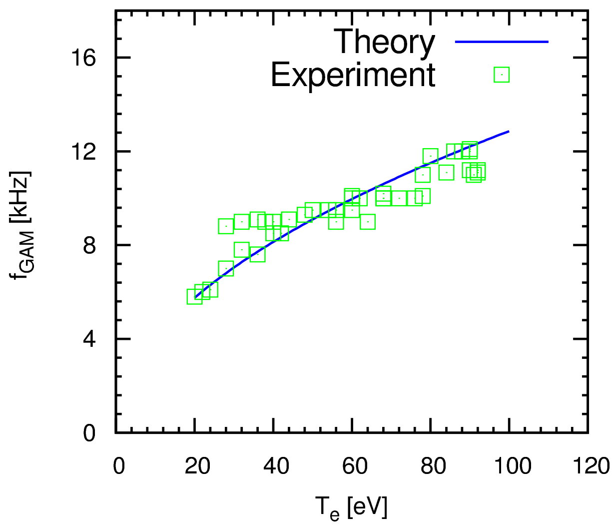

Figure 8.2: Comparison of the GAM frequency with the theoretical dispersion relation.

8.2 The spatial structure of GAM

It has been mentioned in section 1.1.1 that zonal flows are poloidally and toroidally symmetric $E_r \times B$ structures. Therefore, the important step in identifying certain fluctuations as zonal flows is to identify the symmetric spatial structure of these fluctuations, i.e., to confirm their toroidal and poloidal symmetry. This requires measurements of a long-distance correlation, i.e., the results where the correlation length of fluctuations is much longer than the typical turbulence correlation length (1-2 cm). ~~To investigate the toroidal and poloidal structure of the GAM zonal flows, we have measured the long-distance toroidal ($\approx$ 7 m) and poloidal ($\approx$ 1.2 cm) cross-correlation.~~ The cross-correlation between two signals is defined as follows:

$$C_{xy}(\tau) = \frac{\langle [x(t+\tau) - \bar{x}][y(t) - \bar{y}] \rangle}{\sqrt{\langle [x(t) - \bar{x}]^2 \rangle \, \langle [y(t) - \bar{y}]^2 \rangle}}, \tag{8.3}$$

where τ is the time lag. To investigate the toroidal and poloidal structure of the GAM zonal flows, the cross-correlation has been calculated between two time series of $\tilde{\phi}_{fl}$ or $\tilde{I}_{sat}$ signals, separated either toroidally (distance $\approx$ 7 m) or poloidally (distance $\approx$ 1.2 cm). The results are presented in Fig. 8.3. Figure 8.3(a) and (b) show nearly zero time delay and high value (≈ 0.6) of cross-correlation between two toroidally (a) and poloidally (b) separated $\tilde{\phi}_{fl}$ signals. In addition, the periodicity of functions C_{xy} in Fig. 8.3 corresponds to the GAM frequency of $\approx 10\ kHz$. These two points clearly indicate that GAM oscillations in $\tilde{\phi}_{fl}$ fluctuations are homogeneous in both toroidal and poloidal directions and hence support the idea that the GAM flow is toroidally and poloidally uniform ($m = n = 0$).

Similar study of a long-distance toroidal correlation, as applied to I_{sat} fluctuations measured in the equatorial plane, showed nearly no correlations, as seen in Fig. 8.3(c). However, this result is not unexpected because there is no GAM in the frequency spectrum of $\tilde{I}_{sat}$, as seen in Fig. 8.1(red line).

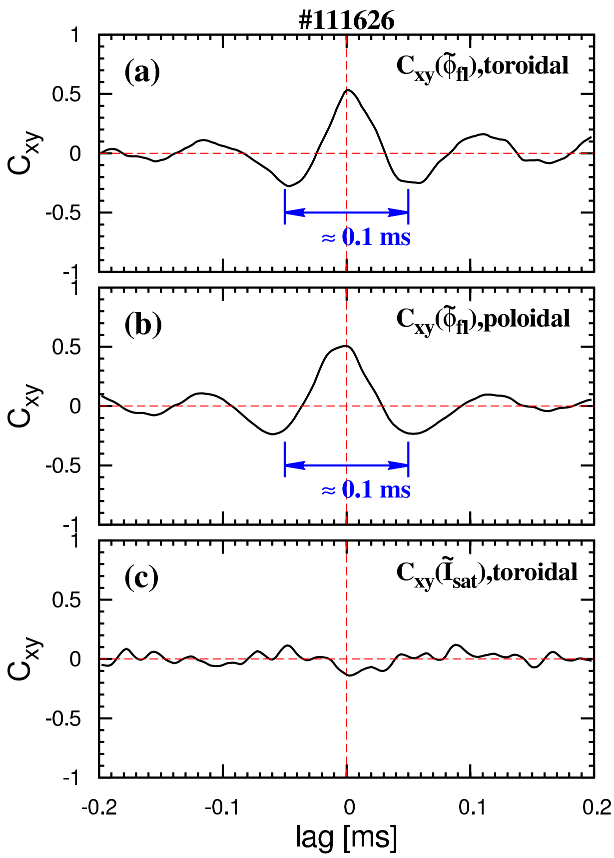

Figure 8.3: (a):The long distance toroidal correlation of two floating potential signals, measured at the same radial location by two toroidally separated (with the distance of $\approx$ 7 m) Langmuir probe pins. (b): The poloidal correlation of two floating potential signals, measured between two Langmuir probe pins, separated with poloidal distance $\approx$ 1.2 cm. (c): The long-distance toroidal correlation of two $\tilde{I}_{sat}$ signals, similar to the one performed for $\tilde{\phi}_{fl}$ signals in Fig.(a).

8.3 The characterisation of the role of GAM zonal flow in turbulent transport

One of the beneficial features of GAM zonal flows is that this mode does not contribute to the turbulent particle transport. This section provides detailed experimental insight into this issue.

The equation for the frequency resolved turbulent particle transport is the following [1, 125, 126]:

$$\Gamma(f) = \sqrt{S_{\tilde{\phi}_p}(f) S_{\tilde{n}}(f)} \left|\gamma_{n\phi_p}(f)\right| k_\theta(f) sin(\alpha_{n\phi_p}(f)), \tag{8.4}$$

where $S_{\tilde{\phi}_p}$ and $S_{\tilde{n}}$ are the power spectrum of plasma potential and density fluctuations, $k_\theta(f)$ is the wavenumber frequency spectrum, $\left|\gamma_{n\phi_p}(f)\right|$ is the coherency function between the density and potential fluctuations and $\alpha_{n\phi_p}(f)$ is the phase shift between $\tilde{n}$ and $\tilde{\phi}_p$. On the way to estimate $\Gamma(f)$ one needs to look at different ingredients of this equation. The power spectrum $S_{\tilde{\phi}_p}$ for the shot #111626 is shown in Fig. 8.4(a). Looking at this spectrum one may expect that GAM zonal flows contribute substantially to the transport.

Now, let's look at the wavenumber-frequency spectrum $k_\theta(f)$ of fluctuations. This $k_\theta(f)$ spectrum may be approximated using the local conditional wavenumber-frequency spectrum $S(k_\theta, f)$ [1, 26, 127]:

$$S(k, f) = \frac{1}{M} \sum_{j=1}^{M} I(k - k^j(f))(S_1^j(f) + S_2^j(f)), \tag{8.5}$$

where

$$I(k - k^j(f)) = \begin{cases} 1 & \text{if } k - k^j(f) \leqslant \triangle k \\ 0 & \text{if } k - k^j(f) \geqslant \triangle k, \end{cases}$$

$S_1^j(f)$ and $S_2^j(f)$ are power spectra measured at two spatially separated points with the distance h from each other. Here, $k^j(f) = \theta_{1,2}^j(f)/h$ is the local wavenumber and $\theta_{1,2}^j(f)$ is the phase shift between two points for each realization j and frequency f, M is the total number of the statistical realizations, $\triangle k$ is the chosen discretisation of the k axis. Figure 8.4(b) displays such $S(k, f)$ spectrum of $\tilde{\phi}_{fl}$ fluctuations for the poloidal wavenumber k_θ. The spectrum is measured in the edge using two poloidally separated Langmuir probe pins ($h = 5.6\ mm$).

The ensemble-averaged $\bar{k}_\theta(f)$ can be obtained from $S(k, f)$ using the following relation:

$$\bar{k}(f) = \frac{\sum_k k \cdot S(k, f)}{S_1^j(f) + S_2^j(f)}, \tag{8.6}$$

In our analysis, the spectrum $\bar{k}_\theta(f)$ is used as an approximation to $k_\theta(f)$, which we need to evaluate $\Gamma(f)$. Figure 8.4(c) shows $\bar{k}_\theta(f)$ spectrum corresponding to

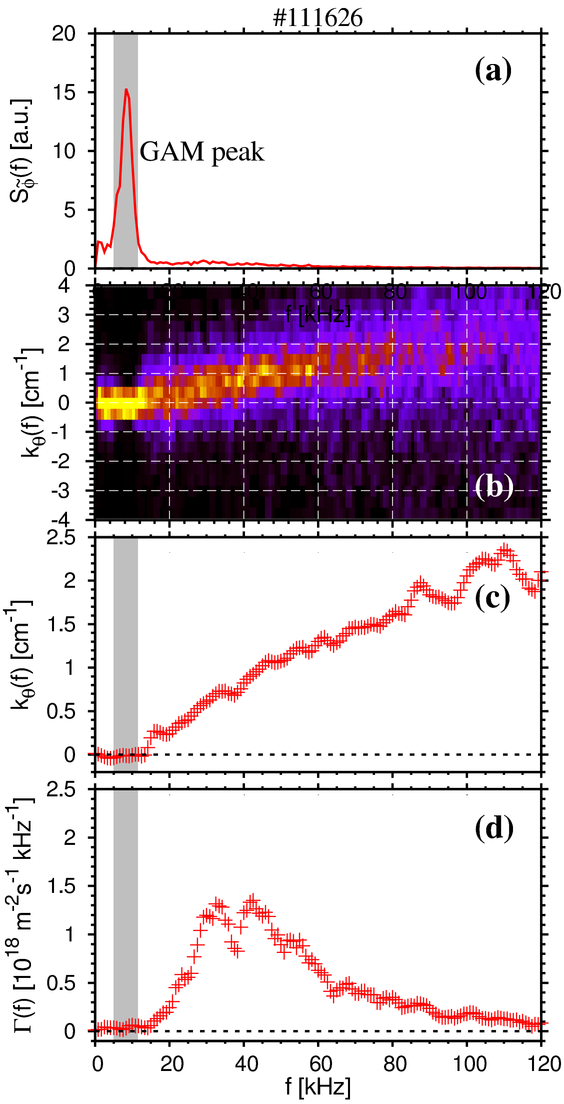

Figure 8.4: (a):The power spectrum of floating potential fluctuations shows the power localisation of GAM in the frequency range of 5-11.5 kHz (indicated by the grey colour bar). (b):The conditional wavenumber-frequency spectrum $S(k, f)$ of floating potential fluctuations. (c): The ensemble-averaged dispersion relation of the poloidal wavenumber $k_\theta(f)$. (d): The frequency resolved turbulent particle transport does not show any contribution in the frequency range of GAM zonal flows.

$S(k_\theta, f)$ in Fig. 8.4(b). This spectrum shows very low poloidal wavenumber in the frequency range of GAM. This is the consequence of a poloidal homogeneity (m=0) of GAM fluctuations, which implies $k_\theta^{GAM} = 0$.

Figure 8.4(d) displays the frequency resolved turbulent particle transport, evaluated using Eq. (8.4). One can see that the dominant contribution to the transport is provided primarily by an ambient turbulence, which is localised in the range of 20-100 kHz. Note that there is no direct contribution of GAM zonal flows, in themselves, to the turbulent transport, even though the power of GAM in the contribution of plasma potential to the product in Eq. (8.4) is substantial. The reason for this is that the power of GAM in the spectrum of plasma potential is outweighed by low values of k_θ^{GAM}, leading to only a marginal fraction of turbulent transport in the range of GAM.

8.4 The modulation of ambient turbulence and transport by GAM

The fundamental process responsible for the growth of zonal flows is considered to be a transfer of the momentum and energy from small-scale turbulent eddies to large-scale flows via the Reynolds stress [29]. This process may also be considered as the three-wave interaction mechanism, as was discussed in Sec. 7.1. In the context of plasma turbulence, the three-wave interactions can be viewed as a parametric or modulational instability [128]. Therefore, it is useful to give some attention to the nature of the modulational instability.

A modulated ambient turbulence mode is subjected to a modulational instability only under certain circumstances. The typical example is a turbulence modes (with wave number k and amplitude E) which have the following properties:

- the dependence of frequency (or phase velocity) on the amplitude of the wave
$$\omega = \omega_0 + \alpha E, \tag{8.7}$$
where α is just a proportionality coefficient.

- the property of an anomalous group velocity dispersion
$$\alpha \frac{\partial v_g}{\partial k} < 0 \tag{8.8}$$
(v_g is the group velocity of turbulence $\partial\omega/\partial k$).

Assuming that $\alpha > 0$, Condition 8.8 means that pulses with longer wavelengths travel with higher group velocity than pulses with shorter wavelength. Such a wave (being modulated) is usually partitioned into separated packets and these packets in turn experience a self-constriction, leading to an amplification of the initial modulation.

This is explained in Fig. 8.5. Figure 8.5(a) shows a weak modulation (green dashed line) at a low frequency Ω imposed on a carrier harmonic wave (black solid line) at a frequency ω_0 . Let's assume that $\alpha > 0$. In that case, the phase velocity in points G and G' is higher than in the point B, according to Relation 8.7. As a result of this, the wavelength in the area P shrinks (wave number grows), whereas the wavelength in the area Q grows (wavenumber reduces). Consequently, provided that $\partial v_g/\partial k < 0$, the group velocity of wave packet in the area P is slightly below the level predicted by the linear theory, whereas the group velocity in the area Q is slightly above that level. This leads to the self-constriction of the wave and an amplification of the initial modulation.

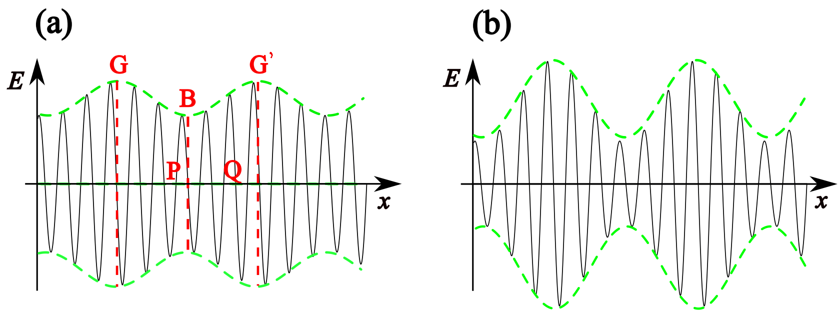

Figure 8.5: (a): The weak modulation (green dashed line) at a low frequency Ω imposed on a carrier harmonic wave (black solid line) at a frequency ω_0. (b): The initially weak modulation may evolve into a strong modulation due to self-constriction of wave packets.

Next, we will show in Fig. 8.6 that the effect of modulation can be interpreted as a result of a three-wave interaction between a strong carrier harmonic wave at a frequency ω_0, a modulating wave at a low frequency Ω and small sidebands $\omega_0 \pm \Omega$. Figures 8.6(a) and (b) show the time trace and the frequency spectrum of a carrier harmonic wave at a frequency ω_0. Figures 8.6(c) displays the carrier wave modulated at a low frequency Ω. This modulation can be equivalently represented as an appearance of sidebands at frequencies $\omega_0 \pm \Omega$, as shown in Fig. 8.6(d). A growth of the sidebands can be treated in terms of a growth of weak modulation imposed on a harmonic wave. Therefore, this is the particular case of a three-wave interaction (a waves at ω_0 and Ω create the waves at $\omega_0 + \Omega$ and $\omega_0 - \Omega$).

Alternatively, the link between amplitude modulation and a three-wave interaction becomes apparent from the mathematical representation of the amplitude modulation by the following product:

$$y(t) = sin(\omega_0 t + \varphi_c)(1 + \alpha\, cos(\Omega t + \varphi_m)), \tag{8.9}$$

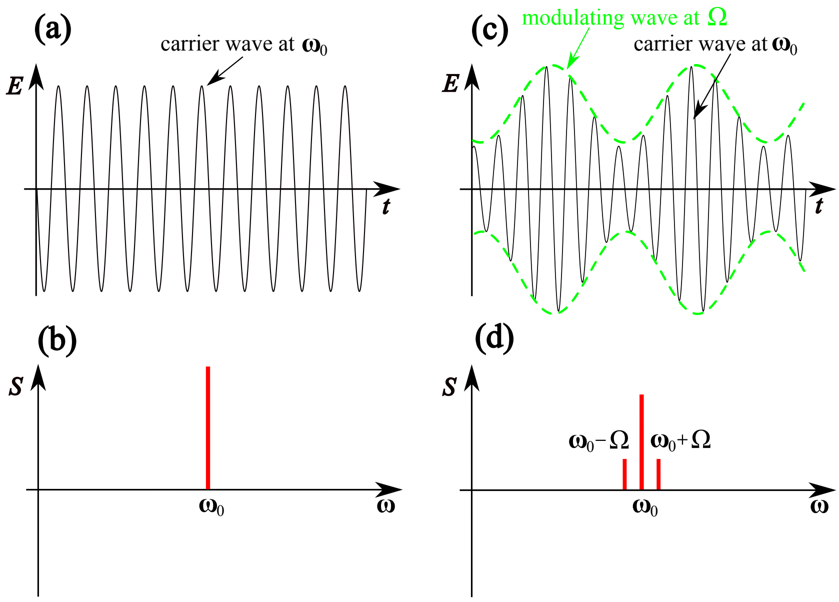

Figure 8.6: (a)-(b): The carrier harmonic wave (black solid line) at a frequency ω_0 and its monofrequency spectrum. (c)-(d): The carrier wave modulated at a low frequency Ω can be equivalently represented as an appearance of sidebands at frequencies $\omega_0 \pm \Omega$.

where φ_c and φ_m represent the initial phases of the carrier and modulating waves, respectively, and α represents the modulation depth. Using trigonometric identities, $y(t)$ can be expressed in the form

$$y(t) = sin(\omega_0 t+\varphi_c)+\frac{\alpha}{2}(sin((\omega_0+\Omega)t+(\varphi_c+\varphi_m))+sin((\omega_0-\Omega)t+(\varphi_c-\varphi_m))). \tag{8.10}$$

It is visible that the signal $y(t)$ has three components: a carrier wave and two sidebands, whose frequencies are slightly above and below ω_0.

Concerning the turbulence in toroidal magnetized plasmas, this process is usually considered as a modulation of ambient turbulence by zonal flows. Many experimental results have been reported regarding to such a modulation [27, 122, 129]. These measurements have been done in HL-2A and JFT-2M machines.

Here, we present a similar study conducted in the TEXTOR tokamak. Our analysis in this direction has qualitative and superficial character rather than systematic study on different aspects of a modulational instability, e.g., the fulfillment of Conditions 8.7 and 8.8. This is primarily due to limited measurement capability of our diagnostics because Langmuir probe as well as GPI can not directly measure either the group velocity or nonlinear properties in equation 8.7. In our analysis we follow the approach suggested in earlier works in Refs. 27, 122, 129, although we undestand that this approach is by far not complete and may well be lengthened.

Figure 8.7(a) shows $\tilde{\phi}_{fl}$ fluctuations bandpass filtered in the frequency range of 7-11 kHz, which includes more than 90% of the GAM power. Figure 8.7(b) presents high frequency ambient fluctuations in the range 50-120 kHz. The blue solid line indicates the envelope of ambient fluctuations extracted using the Hilbert transformation technique [28]. This envelope provides the measure of the power of fluctuations. It is visible that the envelope oscillates with the frequency which seems to be close to the frequency of GAM oscillations in Fig. 8.7(a). However, one has to say that this finding is not considered to be a direct evidence that GAMs modulate high frequencies. In the latter case, both oscillations (GAM and power envelope) would be synchronized (with a certain phase shift), but that is not the case. Therefore, our results provide only some hint that GAMs could modulate high frequency modes and a further study in this direction is certainly needed. Such a study is presented in the next section.

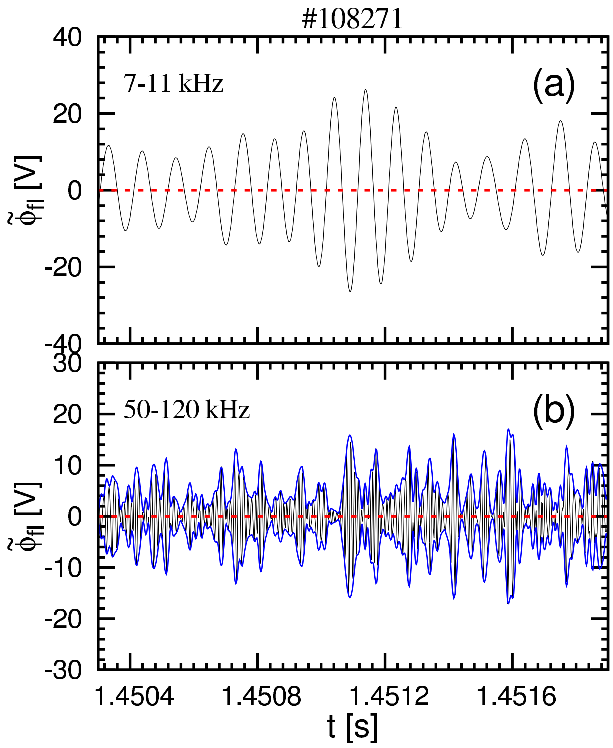

Figure 8.7: (a): Fluctuations of $\tilde{\phi}_{fl}$ bandpass filtered in the frequency range of GAM zonal flows 7-11 kHz. (b): Fluctuations of $\tilde{\phi}_{fl}$ filtered in the range of ambient turbulence 50-120 kHz.

8.5 Bispectral analysis

We have already mentioned in the previous section that GAM zonal flows are driven by small-scale turbulent fluctuations via the modulational instability which can be interpreted as a three-wave interaction process. The bispectral analysis is a signal processing technique for the experimental identification of the three-wave interaction, the measure of the phase coupling between different frequencies in the spectrum occurring as a result of the nonlinear interaction between them. Therefore, the bispectral analysis can be considered as a technique for the identification of the modulation process.

The squared bicoherence [130] of fluctuations is defined as follows

$$b^2{}_{\alpha\beta\gamma}(f_1, f_2) = \frac{\left|\frac{1}{M}\sum_{i=1}^{M}\alpha_i(f_1)\beta_i(f_2)\gamma_i^*(f_1+f_2)\right|^2}{([\frac{1}{M}\sum_{i=1}^{M}|\alpha_i(f_1)\beta_i(f_2)|^2][\frac{1}{M}\sum_{i=1}^{M}|\gamma_i(f_1+f_2)|^2])}, \quad (8.11)$$

where $\alpha(f_1)$ means the f_1 komponent of FFT spectrum for signal α, and $*$ denotes the complex conjugate. The case of $\alpha = \beta = \gamma$ pertains auto-bicoherence while the others for cross-bicoherence.

The meaning of the bicoherence is easiest to explain by the example of the auto-bicoherence of the amplitude modulation $y(t)$ presented in equation 8.9. Let's denote three equal quantities α, β and γ in equation 8.11 as Y (Fourier transform of $y(t)$):

$$b^2{}_{YYY}(f_1, f_2) = \frac{\left|\frac{1}{M}\sum_{i=1}^{M}Y_i(f_1)Y_i(f_2)Y_i^*(f_1+f_2)\right|^2}{([\frac{1}{M}\sum_{i=1}^{M}|Y_i(f_1)Y_i(f_2)|^2][\frac{1}{M}\sum_{i=1}^{M}|Y_i(f_1+f_2)|^2])} \quad (8.12)$$

The representation of the modulation by the equation 8.10 has one important property: the phases of sidebands are either sum or difference of the phases of the carrier wave and the modulating wave ($\varphi_c + \varphi_m$ or $\varphi_c - \varphi_m$). Therefore, the two quantities $Y(\omega_0)Y(\Omega)$ and $Y(\omega_0 + \Omega)$ are perfectly phase locked as well as the quantities $Y(\omega_0)Y(-\Omega)$ and $Y(\omega_0 - \Omega)$. Then if the Fourier transform is calculated several times from different parts of the time series, and we add together all of the products $Y(\omega_0)Y(\pm\Omega)Y^*(\omega_0 \pm \Omega)$, they will sum without cancelling. On the other hand, suppose that the phases of each of these frequencies ω_0, Ω, $\omega_0 + \Omega$, $\omega_0 - \Omega$ is random. Then, adding together all of the products $Y(\omega_0)Y(\pm\Omega)Y^*(\omega_0 \pm \Omega)$ will result in cancellation, and so the sum will have a small magnitude. Detecting phase coupling requires summation over a number of independent samples.

Another issue is that the product $Y(\omega_0)Y(\pm\Omega)Y^*(\omega_0 \pm \Omega)$ depends on the magnitudes of each of the frequency components. The bicoherence includes a normalization factor that removes the magnitude dependence and so the bicoherence is bounded between 0 and 1.

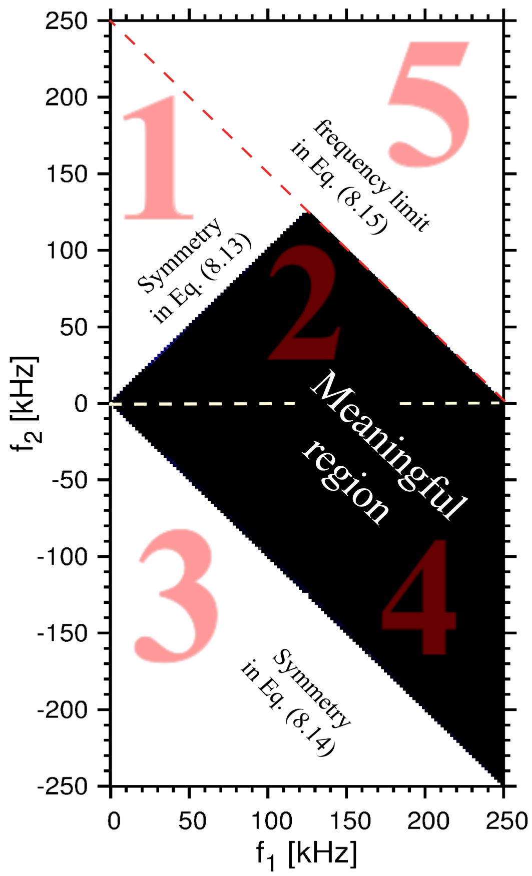

Figure 8.8: The typical representation of the auto-bicoherence. The blank (white) regions (regions 1, 3 and 5) in this figure correspond to the areas where the bicoherence is either meaningless or does not provide any new information in addition to the information in the meaningful area, that is coloured in black (regions 2 and 4).

The result of the auto-bicoherence is typically presented using a 2D contour plot, as shown schematically in Fig. 8.8. The blank (white) areas (regions 1, 3 and 5) of the frequency space $f_1 - f_2$ in this figure correspond to the regions where the bicoherence is either meaningless or does not provide any new information in addition to the information in the meaningful area, that is coloured in black (regions 2 and 4). The following properties and requirements determine such a representation of the auto-bicoherence:

1. The first property of symmetry:

$$b^2{}_{YYY}(f_1, f_2) = b^2{}_{YYY}(f_2, f_1) \tag{8.13}$$

This is apparent from the fact that both numerator and denominator of Eq. 8.12 are permutation invariants with respect to f_1 and f_2.

In particular, equation 8.13 means that the region №1 is equivalent to the region №2 and, therefore, does not provide any original information, additional to the one in the region №2. That is why the region №1 is blank.

2. The second property of symmetry:

$$b^2{}_{YYY}(f_1, -f_2) = b^2{}_{YYY}(f_2, -f_1) \tag{8.14}$$

This becomes clear from the following. In property 8.14, looking at the numerators and comparing two terms

$$Y(f_1)Y(-f_2)Y^*(f_1 - f_2)$$

and

$$Y(f_2)Y(-f_1)Y^*(f_2 - f_1),$$

we see that they are the complex conjugates of each other so that their amplitudes are equal. Therefore, after summation over a number of independent samples, the amplitudes of corresponding numerators in $b^2{}_{YYY}(f_1, -f_2)$ and $b^2{}_{YYY}(f_2, -f_1)$ are also equal. Similar considerations can also be given for denominators.

In Figure 8.8, the region №3 is blank because it is equivalent to the region №4, following property 8.14 and, therefore, does not provide any new information.

3. The frequency limit.
The Nyquist frequency $f_{Ny} = 250\,kHz$, which is the highest representable frequency, impose the following condition:

$$f_1 + f_2 \leqslant f_{Ny} \tag{8.15}$$

This requirement imposes the region №5 in Fig. 8.8 to be blank because any combination of f_1 and f_2 in this region leads to $f_1 + f_2 > f_{Ny}$, what makes meaningless the evaluation of $Y_i(f_1 + f_2)$ in equation 8.12.

Figures 8.9(a) and (b) show the contour and surface plots of the auto-bicoherence of $\langle\tilde{\phi}_{fl}\tilde{\phi}_{fl}\tilde{\phi}^*_{fl}\rangle$. All bicoherences in the following analysis are computed with a frequency resolution of 1 kHz and averaged over 1650 samples ($N_{sampl} = 1650$) to reduce the statistical noise.

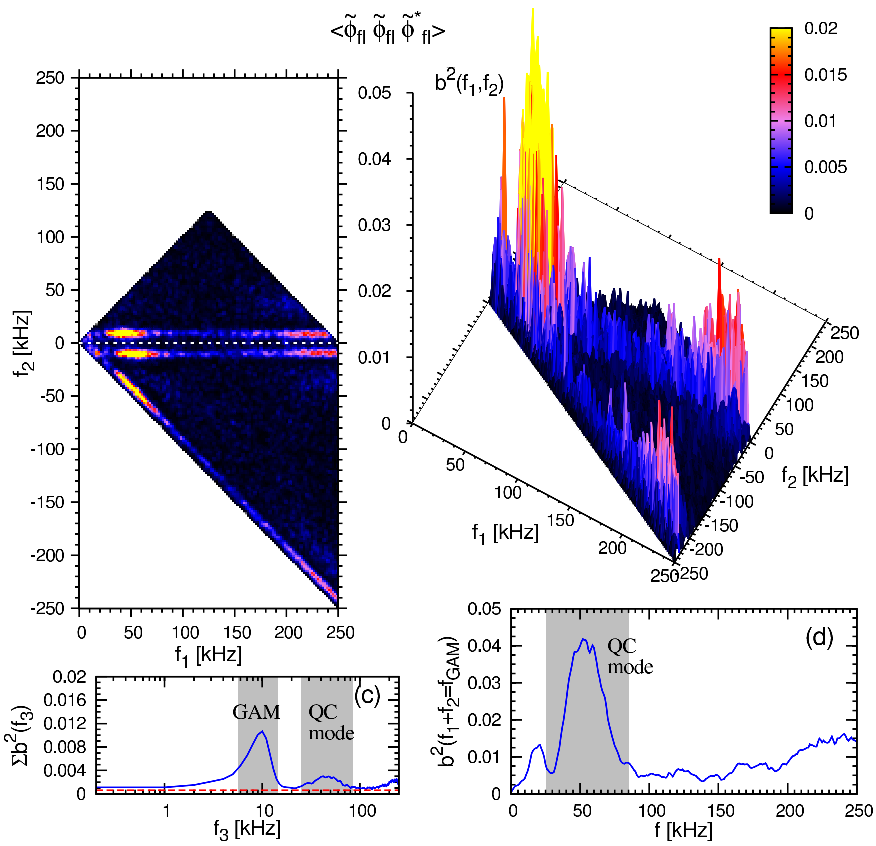

Figure 8.9: The contour (a) and surface (b) plots of the auto-bicoherence of $\langle \tilde{\phi}_{fl}\tilde{\phi}_{fl}\tilde{\phi}^*_{fl}\rangle$. (c) The corresponding total bicoherence. The dashed red line indicates the level of statistical uncertainty $1/N_{sampl} \approx 6 \times 10^{-4}$. (d) The cut of the bicoherence $b^2(f_1, f_2)$ along the line $f_1 + f_2 = f_{GAM}$ showing the strength of interaction between GAM and other frequencies in the spectrum.

It is visible that the bicoherence around the lines of $f_1 + f_2 = f_{GAM}$, $f_2 = \pm f_{GAM}$ in both plots is substantially larger than the statistical noise (the level of the statistical uncertainty is $1/N_{sampl} \approx 6 \times 10^{-4}$). This indicates a significant level of the three-wave interaction between f_{GAM} and ambient turbulence.

Figure 8.9(c) in turn shows the summed squared auto-bicoherence:

$$\Sigma b^2(f_3) = \sum_{f_3=f_1+f_2} b^2(f_1, f_2), \tag{8.16}$$

where the summation is conducted for all combinations of f_1 and f_2 that meet the condition $f_3 = f_1 + f_2$. It provides a measure of the three-wave coupling at

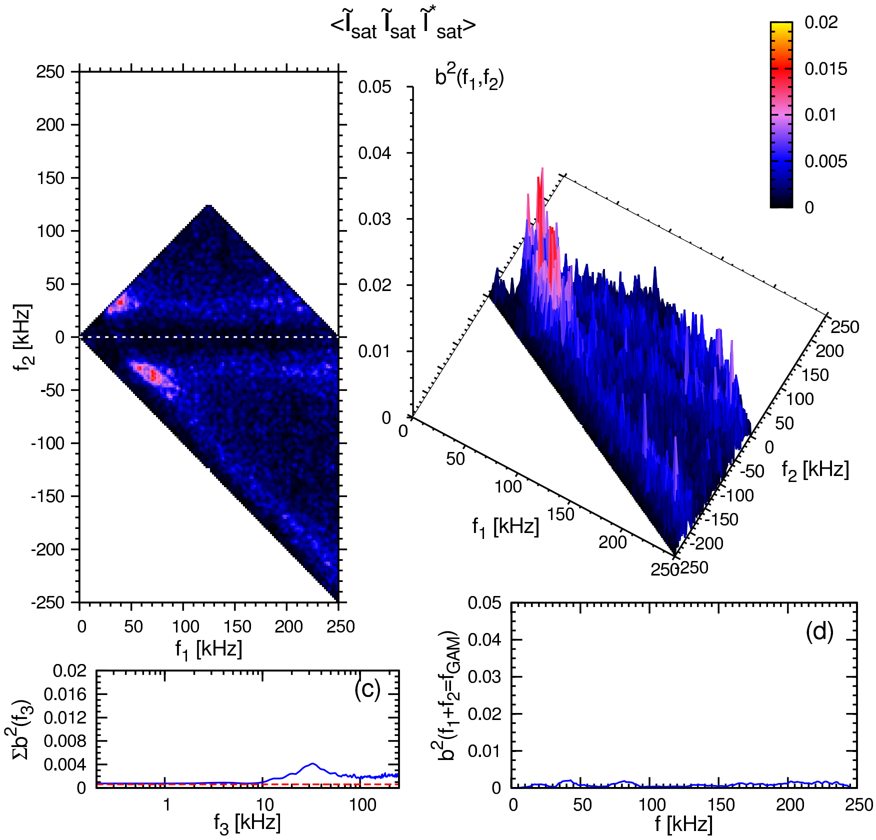

Figure 8.10: The contour (a) and surface (b) plots of the auto-bicoherence of $\langle \tilde{I}_{sat}\tilde{I}_{sat}\tilde{I}^*_{sat}\rangle$. (c) The corresponding total bicoherence. (d) The cut of the bicoherence $b^2(f_1, f_2)$ along the line $f_1 + f_2 = f_{GAM}$.

the frequency f_3. The dashed red line indicates the level of statistical uncertainty $1/N_{sampl}$. An apparent peak at the GAM frequency (indicated by the grey solid area) suggests the nonlinear interaction between GAM and ambient turbulence. The peaked value of the $\Sigma b^2(f_3)$ is $\approx 10^{-2}$.

In Figure 8.9(c), it should be noted that except of GAM peak there is another weaker peak in the range of 30-80 kHz (indicated by the grey solid area), associated with QC mode. This peak is caused by the nonlinear interaction between QC mode and ambient turbulence. This shows that nonlinear three-wave interaction is not a special feature of GAM zonal flows only but, in fact, a very general property of plasma turbulence.

In its turn, Figure 8.9(d) displays the interaction satisfying the frequency matching condition $f_1 + f_2 = f_{GAM}$ (along the diagonal line). This profile specifically shows the coupling between GAM and other frequencies in the spectrum. It is visible that the bicoherence value along this line is very inhomogeneous and varies in the range of $10^{-2} - 4 \cdot 10^{-2}$. For instance, GAM couples with QC mode (frequency range 20 - 80 kHz) several times stronger than with higher frequency components (80-250 kHz).

The results of Figure 8.9 show that the level of phase coupling, occurring as a result of a modulation by GAM, is substantially higher than the statistical uncertainty. Therefore, these results could be used as an evidence that GAMs modulate high frequencies.

Figures 8.10(a) and (b) show the contour and surface plots of the auto-bicoherence of ion saturation current $\langle \tilde{I}_{sat} \tilde{I}_{sat} \tilde{I}^*_{sat} \rangle$. These results show that no significant nonlinear interaction is visible in the density field at the GAM frequency. This is also apparent from the summed auto-bicoherence in Fig. 8.10(c). This is foreseeable taking into account that there is no GAM fluctuations in the power spectrum of $\tilde{I}_{sat}$. However, the figure 8.10 shows a substantial interaction for the QC mode, similar to that in Fig. 8.9. This is understandable in the view that drift-wave driven QC mode has both plasma potential and density components.

~~The majority of bicoherence estimates presented in the literature concerning the study of an interaction between the GAM and turbulence are based on the auto-bicoherence of either $\tilde{\phi}_{fl}$ or $\tilde{I}_{sat}$ fluctuations, without involving Reynolds stress components, i.e., velocities $\tilde{v}_r$ and $\tilde{v}_\theta$. This situation has historically developed due to difficulty in direct simultaneous measurements of these quantities. However, zonal flows are driven by the Reynolds stress. Therefore, it is better to use the physically more grounded quantities, i.e., to estimate the nonlinear interaction on the base of Reynolds stress components. Some aspects on this issue have been already discussed in Ref. 112. The appropriate combination of quantities is visible by looking at the three-wave interaction term in equation (7.10), from where it is visible that the following combination $\langle \tilde{v}_r \tilde{v}_\theta \tilde{v}^*_\theta \rangle$ would be the most straightforward example.~~

~~Figure **??** shows the cross-bicoherence of $\langle \tilde{v}_r \tilde{v}_\theta \tilde{v}^*_\theta \rangle$, where Reynolds stress components are directly involved. It is visible that the nonlinear interaction is higher as compared to the auto-bicoherence of $\langle \tilde{\phi}_{fl} \tilde{\phi}_{fl} \tilde{\phi}^*_{fl} \rangle$ in Fig. 8.9. The peaked value of the $\Sigma b^2(f_3)$ at the GAM frequency in Fig. **??**(c) is $\approx 1.6 \cdot 10^{-2}$, which is 1.5 times larger than that value in Fig. 8.9(c). More details about the interaction of GAM with other frequencies are visible in Fig. **??**(d). This figure also shows a noticeable interaction with QC mode, the same as in Fig. 8.9(d). However, the coupling with higher frequencies ($f > 80\ kHz$) is substantially larger and much more homogeneous throughout frequencies as compared to results in Fig. 8.9(d). This is the direct improvement coming from the using of Reynolds stress components.~~

8.6 Summary

The study presented in this chapter contains several key outcomes.

- The apparent ≈10 kHz mode in the frequency spectrum of floating potential fluct is identified as GAM zonal flows. In particular: (a) experiments show high toroidal and poloidal homogeneity of this mode, in agreement with the theoretical model of GAMs ; (b) the systematic study shows that the experimentally measured GAM frequencies correspond to theoretical predictions of equation (8.2); (c) These 10 kHz oscillations in the frequency spectrum of ion saturation current, when measured in the equatorial plane of the torus, are ambiguous, which is also consistent with the theory of GAM.

- Our experiments show that GAM zonal flows, in themselves, do not contribute to the turbulent transport. It is visible from the frequency spectrum of turbulent transport, where no contribution at the GAM frequency is observed.

- The nonlinear coupling between broadband turbulence and GAMs has been identified using the auto-bicoherence analysis of $\tilde{\phi}_{fl}$ and $\tilde{I}_{sat}$. ~~Moreover, the cross-bicoherence analysis which directly involves Reynolds stress components of $\tilde{v}_r$ and $\tilde{v}_\theta$ shows better coupling than the traditional auto-bicoherence of $\tilde{\phi}_{fl}$.~~

9

Overall Conclusion and Future Directions

The rising energy consumption around the globe could eventually lead to an energy crisis if no alternatives to the conventional energy sources will be provided. Controlled nuclear fusion provides a promising alternative as it proposes an almost inexhaustible, relatively safe and clean energy source. To date, the most promising approach towards this goal is a magnetic confinement fusion in a so-called "tokamak". Experimental measurements of the cross-field transport in tokamaks show that the heat and particle transports are substantially larger than values predicted by neoclassical theory. There are several possible explanations that resolves the inconsistency and the most widely followed explanation is the role of the plasma turbulence.

Turbulence in the edge region of tokamaks and other magnetized plasmas has been measured for many years. The transport in the edge and the SOL depends on the level and characteristics of this turbulence and, consequently, on the edge temperature and density. The edge conditions then may affect the core confinement through their effects on edge gradients and gradient driven instabilities such as drift waves. The edge turbulence may also play a crucial role in high confinement physics (i.e., H-mode physics) where steep edge pedestals in the temperature and density form within the closed field line region nearby the separatrix.

Previous investigations show that turbulent structures seem to be highly elongated along magnetic field lines. Rapid streaming of the highly mobile electrons along magnetic field lines smoothes fluctuations along the field and thus restricts significant variations to the radial *vs* poloidal plane. Therefore, the dynamics of turbulence across magnetic field lines appear to be more informative. Consequently, characterizing and understanding the underlying physical mechanisms require essentially two-dimensional (radial *vs* poloidal) turbulence measurements.

For the purposes of this work, the GPI diagnostic, assigned to measure 2D effects of the plasma turbulence, has been developed for the TEXTOR tokamak. With this diagnostic, the two-dimensional structure and dynamics of turbulence in the edge of TEXTOR have been observed for the first time. Results are presented in chapter 3. The main technical novelty of this system is the novel design of the in-vessel GPI optical telescope system which can sustain severe thermal load and coating. The presented design, might be used as a basis for the GPI systems on next generation machines. The assessment of diagnostic issues and limitations suggests that the local gas puff with the flux $(6-8)\times10^{19}$ molec/s, typical for the GPI experiment on TEXTOR, does not influence substantially on local and global plasma performance neither on plasma turbulence properties. Meanwhile, we have shown that the equilibrium/fluctuating emission intensity is more sensitive to the equilibrium/fluctuating electron density than the equilibrium/fluctuating electron temperature, supporting the idea that the GPI is the diagnostic that measures primarily density events. The difference in the dynamics of turbulent structures in the SOL has also been identified between divertor and limiter tokamaks. The decay of structures in the SOL of limiter tokamaks is much faster due to probably shorter connection length of the magnetic field line to the toroidal (or even poloidal) limiter.

One of the most important and challenging data analysis methods relevant to the processing of GPI data is the reconstruction of the velocity vector field from the sequence of GPI frames. Having information about the time-resolved velocity vector field can disclose an interplay between vorticity and density fluctuations.

In chapter 4 we described the multiresolution algorithm, which has been used for the processing of GPI data in this work. There is a problem of local minima of the functional (4.7) caused by the fact that the turbulent structures do not simply move but also change the shape, i.e., they are simultaneously bended, stretched and flattened. The smoothing of images removes these small details, remaining only a translational motion. In the multi-resolution technique the output from the coarse image is used as an initialization at a finer scale. The full pyramid of images is used, starting with the coarsest grid. Although not perfect, this technique gives some improvements in the reconstruction of the velocity vector field as compared to the traditional Horn and Schunck approach.

The turbulence-flow interaction is an important aspect of the edge physics due to the role of $E_r \times B$ flow shear in the suppression of turbulence and reduction of radial transport. The deep understanding of the turbulence-flow interaction requires the detailed characterisation of the poloidal flows in the plasma edge. In chapter 5, the measurements of the poloidal velocity using the Langmuir probe and GPI diagnostics are compared to the edge $E_r \times B$ poloidal flow. We have shown that in the poloidal direction, the turbulent structures move downward in the SOL (along the ion diamagnetic drift direction) and upward in the plasma edge (along the electron diamagnetic drift direction), following up mainly with the $E_r \times B$ drift. Both, probe and GPI measurements give the edge turbulence phase velocities of $-(1-3)\ km/s$. The corresponding phase velocity in the SOL is $1-2\ km/s$. The magnitude of the poloidal plasma rotation in both the edge and the SOL gradually reduces with increasing line-averaged density and toroidal magnetic field. The thickness of the shear layer, where the poloidal flow sharply changes the sign, is estimated to be $5-8\ mm$.

The reduction of the turbulent transport in the presence of sheared flows is attributed to the radial decorrelation mechanisms [21] (BDT model). The systematic study of the eddy decorrelation by sheared flows observed by a two-dimensional gas-puff imaging diagnostic in the edge of the TEXTOR tokamak is presented in chapter 6. In particular, we present the direct experimental evidence of eddy breaking and tilting events observed at the edge of the TEXTOR tokamak using a 2D GPI diagnostic. Here, one has to emphasize that the breaking of eddies in fusion plasma by sheared $E_r \times B$ flow has been observed for the first time. The shearing effects on eddies depends on the coherence length of the eddy structure, namely, the poloidal and radial correlation lengths $\omega_s \propto l_{cr} l_{c\theta}^{-1}$. The magnitude of the flow shearing rate plays a key role for the eddy breaking and needs to be larger than some lower limit. In one shot, both "tilt only" and "tilt and split" events can be seen depending on poloidal and radial extensions of eddies.

Besides spontaneous flows, poloidal flows in the plasma can also be generated by externally induced electric fields. In the concept of plasma biasing, the plasma potential is locally induced by means of an graphite biasing electrode inserted into the hot plasmas. In chapter 7, biasing is applied in order to study intermediate mechanisms involved in the turbulence-flow interaction across the transition to an improved confinement. These results present the first evidence of the eddy stretching and splitting process in a confinement device and the intimate interaction between sheared flows, eddy structures, Reynolds stress, zonal flows and ambient fluctuations during the transition to an improved confinement. The flow shear gives the dynamical influence on turbulence structures, which results in the generation of the Reynolds stress and zonal flows and eventually suppresses background fluctuations due to the nonlinear energy transfer.

Except of mean $E_r \times B$ flows, the suppression of turbulence can occur by zonal flows (ZFs). This type of poloidal flows is spontaneously excited, poloidally and toroidally symmetric, long lived $E_r \times B$ structures. In contrast to the mean "zero-frequency" flows, these flows have finite, though small, oscillation frequency. In toroidal plasmas, two types of zonal flows are expected: the low-frequency ZF and the high-frequency geodesic acoustic mode (GAM). Chapter 8 provides a comprehensive experimental analysis of GAM zonal flows and the role they play in the turbulent transport. It is shown that the apparent ≈10 kHz mode in the frequency spectrum of floating potential is attributed to GAM zonal flows. These GAM oscillations in the frequency spectrum of ion saturation current, when measured in the equatorial plane of the torus, are ambiguous. The systematic study shows that the experimentally measured GAM frequencies very well correspond to the theoretical dispersion relation. In addition, experiments show high toroidal and poloidal homogeneity of this mode, in agreement with the theoretical model. Our experiments show that there is no contribution of GAM zonal flows, in themselves, to the turbulent transport. Moreover, GAMs produce substantial modulation of ambient turbulence and corresponding turbulent transport. The amplitude modulation of ambient broadband turbulence by GAM is the first step towards a nonlinear coupling between these frequencies. This nonlinear coupling has been identified using the bicoherence analysis. The auto-bicoherence for the fluctuations of $\tilde{\phi}_{fl}$ and $\tilde{I}_{sat}$ and cross-bicoherence for $\tilde{v}_r$ and $\tilde{v}_\theta$ have been calculated. This analysis shows the nonlinear interaction between GAM and ambient turbulence. ~~Moreover, the cross-bicoherence analysis which directly involves Reynolds stress components of~~ ~~$\tilde{v}_r$ and $\tilde{v}_\theta$ shows better coupling than the traditional auto-bicoherence of $\tilde{\phi}_{fl}$.~~

9.1 Future Directions

One would like to discuss about some trends in the development of this technique.

Future development of the GPI technique. A significant drawback of the GPI diagnostic is a very narrow radial localisation of the emission intensity (approximately 6-8 cm in the vicinity of LCFS). Therefore, the development of the GPI technique in the way to extend its diagnostic range would be an attractive proposition. It would be especially attractive if the radial range of the GPI system overlaps with the corresponding radial range of the BES or reflectometry systems so that one can make a direct cross-comparison between these diagnostics.

The interpretation of an emission intensity in terms of n_e and T_e is another challenging diagnostic issue which should be studied thoroughly in the context of a development of the GPI technique. Without some effort in this direction, the interpretation of measured GPI results can be done only qualitatively. One possible approach to simplify this interpretation is to use the *helium line intensity ratio technique* [66], which is a common method used to determine the electron temperature and density in the boundary region of magnetic fusion devices. This effort requires the development of an atomic physics modelling such as DEGAS 2 to accurately describe the physics processes of the helium cloud interacting with plasma. Meanwhile, it requires much more complex imaging system (optics and cameras) where the resulting image is splitted into 3 equivalent images so that one can make simultaneous observations in different spectral lines.

The inherent feature of the GPI diagnostic is that GPI observations are essentially two-dimensional. This feature is based on the assumption that turbulent structures are believed to have a parallel wavelength $k_{\|}$ much longer than the perpendicular wavelength $k_{\perp}$. However, it is not clear whether the turbulent structures are completely homogeneous along the magnetic field so that $k_{\|} = 0$ or whether some finite scales may be involved. The measurement of the tree-dimensional turbulence geometry is the another subject of the development of the GPI technique which is receiving much attention today [32, 47].

Future development of the velocity vector field reconstruction. The main assumption of the optical flow methods is that the intensity of a turbulent structure does not change as the structure is being moved along its pathline (trajectory) while following the flow. This is known as the intensity constancy assumption or optical flow constraint, which is equivalent to the requirement that the divergence of the velocity field sought is zero. However, there is no reason for this to be true in general (especially in the case of turbulent motion), and the intensity constancy assumption is badly violated in reality. Based on these considerations, an alternative brightness constraint, which would be more suitable for the physics of turbulence, has been proposed. The suggestion is to use directly the continuity equation (4.5), as a more physically-grounded constraint. The assessment of the validity of this new brightness constraint in the particular case of the GPI imaging is the subject of our future work.

Another limitation is that the local velocity vectors should lie along the local intensity gradient, which is known as an aperture problem. We have shown in section 4.6 that the 2D cross-correlation technique is an alternative approach which has an advantage over the standard optical flow technique in that it is free of this ”aperture problem” limitation. Therefore, this is considered to be the promising strategy for further improvements of our algorithm.

References

[1] Ch.P. Ritz et al. Rev. Sci. Instrum., 59:1739, 1988.

[2] M. Endler et al. Nucl. Fusion, 35:1307, 1995.

[3] T. Uckan et al. Nucl. Fusion, 35:487, 1995.

[4] D. L. Winslow et al. Rev. Sci. Instrum, 68:396, 1996.

[5] H. Thomsen et al. Phys. Plasmas, 9:1233, 2002.

[6] J. Bleuel et al. New J. Phys, 4:38, 2002.

[7] H. Thomsen et al. Plasma Phys. Control. Fusion, 47:1401, 2005.

[8] T. Carter et al. Phys. Plasmas., 16:012304, 2009.

[9] P. Manz et al. Plasma Phys. Control. Fusion, 50:035008, 2008.

[10] I. Furno et al. Phys. Plasmas., 15:055903, 2008.

[11] S. Zoletnik et al. Rev. Sci. Instrum., 76:073504, 2005.

[12] G. R. McKee et al. Phys. Plasmas., 10:1712, 2003.

[13] A. De Coninck. *Experimental study of the turbulent flow characteristics of the boundary plasma in the Stellarator TJ-II*. Master's thesis, Ghent University, Belgium, 2008.

[14] T. Munsat et al. Rev. Sci. Instrum., 77:103501, 2006.

[15] N. Fedorczak et al. Phys. Plasmas., 19:122302, 2012.

[16] S. Srinivasan and R. Chellappa. J. Opt. Soc. Am. A, 16:493, 1999.

[17] R. J. Taylor et al. Phys. Rev. Lett., 63:2365, 1989.

[18] S. Jachmich et al. Plasma Phys. Control. Fusion, 40:1105, 1998.

[19] Ch. P. Ritz et al. Nucl. Fusion, 27:1125, 1987.

[20] Ch. P. Ritz et al. Phys. Rev. Lett., 68:2543, 1990.

[21] H. Biglari, P. H. Diamond, and P. W. Terry. Phys. Fluids B, 2:1, 1990.

[22] P. H. Diamond et al. Phys. Fluids B, 3:1626, 1991.

[23] J. F. Drake et al. Phys. Fluids B, 4:488, 1992.

[24] G. Conway et al. Phys. Rev. Lett., 106:065001, 2011.

[25] E-J. Kim and P. Diamond. Phys. Plasmas., 10:1698, 2003.

[26] T. Lan et al. Plasma Phys. Control. Fusion., 58:045002, 2008.

[27] T. Ido et al. Plasma Phys. Control. Fusion, 48, 2006.

[28] Y. Nagashima et al. Plasma Phys. Control. Fusion., 49:1611–1625, 2007.

[29] A. Fujisawa et al. Nucl. Fusion., 49:013001, 2009.

[30] K. J. Zhao et al. Phys. Rev. Lett., 96:255004, 2006.

[31] A. Fujisawa et al. Plasma Phys. Control. Fusion., 49:211–217, 2007.

[32] S. Zweben et al. Phys. Plasmas, 20:072503, 2013.

[33] P. H. Diamond. Plasma Phys. Control. Fusion, 47:R35, 2005.

[34] T. Zhang et al. Physics Letters A, 377:1725, 2013.

[35] N. P. Basse et al. Plasma Phys. Control. Fusion., 45:439–453, 2003.

[36] Y. Xu et al. Plasma Phys. Control. Fusion, 47:1841, 2005.

[37] N. Mahdizadech et al. Phys. Plasmas., 2:3932, 2004.

[38] K. Hallatschek et al. *Action of magnetic islands on GAMs and zonal flows*. In 40th EPS Conference on Plasma Physics and 16th ICPP, page P2.184, Espoo, Finland, 1 5 July 2013.

[39] N. Winsor et al. Phys. Fluids, 11:2448, 1968.

[40] F. Wagner. Plasma Phys. Control. Fusion, 49:1, 2007.

[41] Krämer-Flecken A et al. Phys. Rev. Lett., 97:045006, 2006.

[42] Y. Xu et al. Plasma Phys. Control. Fusion, 53:095015, 2011.

[43] S. Zoletnik et al. Plasma Phys. Control. Fusion, 54:065007, 2012.

[44] S. J. Zweben, D. P. Stotler, et al. Phys. Plasmas, 9:1981, 2002.

[45] R. J. Maqueda, G.A.Wurden, et al. Rev. Sci. Instrum, 74:2020, 2003.

[46] G. Y. Antar et al. Phys. Plasmas., 14:022301, 2007.

[47] S. C. Liu et al. Rev. Sci. Instrum., 83:123506, 2012.

[48] S. Zweben et al. Plasma Phys. Control. Fusion, 54:025008, 2012.

[49] Min Gu. *Advanced optical imaging theory*. Springer-Verlag, Berlin,Heidelber, 2000.

[50] H.-J. Kunze. *Introduction to Plasma Spectroscopy*. Springer, Berlin, 2009.

[51] T. Fujimoto. *Plasma Spectroscopy*. Springer, Berlin, 2004.

[52] J. D. Hey et al. J. Phys. B: At. Mol. Opt. Phys., 32:3555, 1999.

[53] J. D. Hey et al. J. Phys. B: At. Mol. Opt. Phys., 37:2543, 2004.

[54] R. Janev. *Elementary processes in Hydrogen-Helium Plasmas.* Springer, Berlin, 1987.

[55] S. Brezinsek. *Study of atomic and molecular hydrogen in front of a graphite surface in a high-temperature edge plasma*. PhD thesis, Heinrich-Heine-Universität Düsseldorf, 2001.

[56] S. Brezinsek et al. Plasma Phys. Control. Fusion, 47:615, 2005.

[57] E. Hintz and B. Schweer. Plasma Phys. Control. Fusion, 37:87, 1995.

[58] Y. Xu et al. Nucl. Fusion., 47:1696, 2007.

[59] S. J. Zweben, D. P. Stotler, et al. Phys. Plasmas, 44:134, 2004.

[60] Y. Xu et al. Phys. Rev. Lett., 97:165003, 2006.

[61] Y. Xu et al. Phys. Plasmas., 16:110704, 2009.

[62] S. Chen et al. J. Appl. Phys., 36:2363, 1965.

[63] S. Lin et al. Rev. Sci. Instrum., 63:4611, 1992.

[64] O. Schmitz et al. Plasma Phys. Control. Fusion, 50:115004, 2008.

[65] H. Stoschus. *Electron Transport in the Plasma Edge with Rotating Resonant Magnetic Perturbations at the TEXTOR Tokamak*. PhD thesis, Heinrich-Heine-Universität Düsseldorf, 2011.

[66] E. A. Unterberg et al. Rev. Sci. Instrum., 83:10D722, 2012.

[67] T. Corpetti et al. EEE Trans. Pattern Anal. Mach. Intell., 24:365, 2002.

[68] T. Corpetti et al. Experiments in Fluids, 40:80, 2006.

[69] S.S. Beauchemin and J.L. Barron. ACM Computing Surveys Intelligence, 27:433, 1995.

[70] B. Horn and B. Schunck. Artificial Intelligence, 17:185, 1981.

[71] *Tikhonov regularization.* `http://en.wikipedia.org/wiki/Tikhonov_regularization`. Accessed: 30-11-2013.

[72] M.J. Black. *Robust Incremental Optical Flow*. PhD thesis, Yale University, 1992.

[73] I. Shesterikov et al. *The experimental investigation on the role of $E \times B$ flow shear in tilting and breaking of turbulent eddies*. In 39th EPS Conference on Plasma Physics and 16th ICPP, page P5.064, Stockholm, Sweden, 2 - 6 July 2012.

[74] D. J. Tritton. *Physical Fluid Dynamics*. Oxford University Press, Oxford, 1988.

[75] Ö. D. Gürcan et al. Phys. Plasmas., 14:042306, 2007.

[76] D. R. McCarthy et al. *Formation of the shear layer in toroidal edge plasma*. Phys. Fluids B, 5:1188, 1993.

[77] K. Miyamoto et al. *Direct ion orbit loss near the plasma edge of a divertor tokamak in the presence of a radial electric field*. Nucl. Fusion., 36:927, 1996.

[78] S. Krasheninnikov et al. *The influence of a radial electric field on neo-classical orbits and ion prompt losses from tokamak edge plasmas*. Phys. Plasmas., 1:1186, 1994.

[79] V. A. Rozhansky and M. Tendler. Phys. Fluids B 4, page 1877, 1992.

[80] F. L. Hinton and R. D. Hazeltine. Rev. Mod. Phys., 48:239, 1976.

[81] L.M. Kovrizhnykh. Nucl. Fusion., 24:851, 1986.

[82] S.P. Hirshman and D.J. Sigmar. Nucl. Fusion., 21:1079, 1981.

[83] M. De Bock. *Understanding and controlling plasma rotation in tokamaks*. PhD thesis, Technische Universiteit Eindhoven, 2007.

[84] J. Cornelis et al. Nucl. Fusion., 34:171, 1994.

[85] A. Dinklage et al. *Confinement, Transport and Collective Effects*. Springer-Verlag, Berlin,Heidelberg, 2005.

[86] V. A. Rozhansky. *Lecture Notes in Plasma Theory*. Lan, Saint-Petersburg, 2011.

[87] R. J. Bickerton. Nucl. Fusion., 12:609, 1972.

[88] T. H. Stix. *Decay of poloidal rotation in tokamak plasma*. Phys. Fluids, 16:1260, 1973.

[89] S. Braginskii. *Reviews of Plasma Physics vol I.* Plenum, New York, 1965.

[90] K. Miyamoto. *Plasma Physics and Controlled Nuclear Fusion*. Springer-Verlag, Berlin,Heidelber, 2005.

[91] K. Itoh and S.I. Itoh. Plasma Phys. Control. Fusion, 38, 1996.

[92] F.F. Chen. *Introduction to Plasma Physics and Controlled Fusion*. Plenum Press, New York, 1984.

[93] Ch. P. Ritz et al. *Turbulent structure in the edge plasma of TEXT tokamak*. Phys. Fluids 27(12), page 2956, 1984.

[94] K. H. Burell. Phys. Plasmas., 4:1499, 1997.

[95] P. W. Terry. Rev. Mod. Phys., 72:109, 2000.

[96] Y. Z. Zhang and S. M. Mahajan. Phys. Fluids B, 4:1385, 1992.

[97] K. C. Shaing et al. Phys. Fluids B, 2:1492, 1990.

[98] J. Wesson. *Tokamaks*. Clarendon press, Oxford, 2004.

[99] J. A. Alonso et al. Plasma Phys. Control. Fusion, 48:B456, 2006.

[100] J. Boedo et al. Nucl. Fusion., 40:1397, 2000.

[101] R.R. Weynants et al. Nucl. Fusion., 32:837, 1992.

[102] G. Van Oost et al. Plasma Phys. Control. Fusion., 45:621–643, 2003.

[103] M. A. Pedrosa et al. Phys. Rev. Lett., 100:215003, 2008.

[104] M. Shats et al. Phys. Rev. Lett., 88:045001, 2002.

[105] T. Estrada et al. Phys. Rev. Lett., 107:245004, 2011.

[106] L. Schmitz et al. Phys. Rev. Lett., 108:155002, 2012.

[107] P.K. Kundu and I.M. Cohen. *Fluid mechanics, Fourth Edition*. Academic Press, Burlington, USA, 2007.

[108] S. B. Pope. *Turbulent Flows*. Cambridge University Press, 2000.

[109] H. Tennekes and J.L. Lumley. *A First Course in Turbulence*. The MIT Press, Cambridge, Massachusetts, 1972.

[110] A. A. Townsend. *The structure of turbulent shear flow*. Cambridge University Press, 1976.

[111] P. H. Diamond et al. Phys. Rev. Lett., 72:2565, 1994.

[112] G. Tynan et al. Phys. Plasmas., 8:2691, 2001.

[113] C. Holland et al. Phys. Rev. Lett., 96:195002, 2006.

[114] C. Hidalgo et al. Plasma Phys. Control. Fusion., 42:A153–A160, 2000.

[115] Y. H. Xu et al. Phys. Rev. Lett., 84:3867, 2000.

[116] P. H. Diamond et al. *Dynamics of Zonal Flows and Self-Regulating Drift-Wave Turbulence*. In 17th IAEA Fusion Energy Conference, pages IAEA–CN–69/TH3/1, Yokohama, Japan, 19 - 24 October 1998.

[117] I. Shesterikov, Y. Xu, et al. Nucl. Fusion., 52:042004, 2012.

[118] J. P. Antoine. CWI. Quarterly, 11:323, 1998.

[119] J. C. van den Berg, editor. *Wavelet in physics*. Cambridge University Press, Cambridge, 1999.

[120] Y. Sechrest et al. Phys. Plasmas., 18:012502, 2011.

[121] G. Tynan et al. *Power Transfer to Turbulent-driven Low-frequency Sheared $E \times B$ flows as the Trigger for the H-mode Transition*. In 24th IAEA Fusion Energy Conference, pages EX/10–3, San Diego, USA, 8-13 October 2012.

[122] T. Ido et al. Nucl. Fusion, 46:512.

[123] B. LaBombard et al. *Mirror Langmuir Probe observations of edge plasma turbulence and the Quasi-Coherent Mode in Alcator C-Mod*. In U.S. - E.U. Joint Transport Task Force Workshop, Santa Rosa, CA, U.S., 9-12 April 2013.

[124] Y. Nagashima et al. Plasma Phys. Control. Fusion, 48:S1, 2006.

[125] E.J. Powers et al. Nucl. Fusion, 14:749, 1974.

[126] A.J. Wootton et al. Phys. Fluids B 2, 12:2879, 1990.

[127] J. Beall et al. J.Appl.Phys., 53:3933, 1982.

[128] V. E. Zakharov. *Modulation instability: The beginning*. Physica D, 238:540–548, 2009.

[129] A.D. Liu et al. Phys. Rev. Lett., 103:095002, 2009.

[130] Y.C. Kim and E.J.Powers. IEEE Trans. Plasma Sci., 120:PS–7, 1979.

A
Certificate

KYUSHU UNIVERSITY

Itoh Project Prize in
Plasma Turbulence 2012

Winner

This award is made to

Ilya Shesterikov

Ecole Royale Militaire, Belgium

The award is presented for the outstanding presentation of work presented at the 39th European Physical Society Conference on Plasma Physics 2 – 6 July 2012, Stockholm, Sweden.

In the opinion of the judges the recipient showed great enthusiasm and knowledge of his subject area and presented a well based and clear presentation of his work to the judges.

Professor R O Dendy, Editor-in-Chief

17th September 2012

Date

Professor S-I Itoh

3rd. Nov. 2012

Date

Supported by IOP Publishing,
Plasma Physics and Controlled Fusion